Three-Dimensional Circulation Dynamics of Along-Channel Flow in Stratified Estuaries

by

Jeffery Daniel Musiak

A dissertation submitted in partial fulfillment of
the requirements for the degree of

Doctor of Philosophy

University of Washington

1998

Approved by David A. Jay
(Chairperson of Supervisory Committee)

Program Authorized
to Offer Degree Geophysics Program

Date 14 October 1998

In presenting this dissertation in partial fulfillment of the requirements for the Doctorial degree at the University of Washington, I agree that the Library shall make its copies freely available for inspection. I further agree that extensive copying of this thesis is allowable only for scholary purposes, consistant with "fair use" as prescribed in the U.S. Copyright Law. Requests for copying or reproduction of this dissertation may be referred to University Microfilms, 1490 Eisenhower Place, P.O. Box 975, Ann Arbor, MI 48106, to whom the author has granted "the right to reproduce and sell (a) copies of the manuscript in microform and/or (b) printed copies of the manuscript made from microform."

Signature Jeffery D Musick

Date 13 Oct 98

University of Washington

Abstract

Three-Dimensional Circulation Dynamics of Along-Channel Flow in Stratified Estuaries

by Jeffery Daniel Musiak

Chairperson of Supervisory Committee
Affiliate Associate Professor David A. Jay
Graduate Program in Geophysics

Estuaries are vital because they are the major interface between humans and the oceans and provide valuable habitat for a wide range of organisms. Therefore it is important to model estuarine circulation to gain a better comprehension of the mechanics involved and how people effect estuaries. To this end, this dissertation combines analysis of data collected in the Columbia River estuary (CRE) with novel data processing and modeling techniques to further the understanding of estuaries that are strongly forced by riverflow and tides. The primary hypothesis tested in this work is that the three-dimensional (3-D) variability in along-channel currents in a strongly forced estuary can be largely accounted for by including the lateral variations in density and bathymetry but neglecting the secondary, or lateral, flow. Of course, the forcing must also include riverflow and oceanic tides. Incorporating this simplification and the modeling ideas put forth by others with new modeling techniques and new ideas on estuarine circulation will allow me to create a semi-analytical quasi 3-D profile model. This approach was chosen because it is of intermediate com-

plexity to purely analytical models, that, if tractable, are too simple to be useful, and 3-D numerical models which can have excellent resolution but require large amounts of time, computer memory and computing power. Validation of the model will be accomplished using velocity and density data collected in the Columbia River Estuary and by comparison to analytical solutions. Components of the modeling developed here include: 1) development of a 1-D barotropic model for tidal wave propagation in frictionally dominated systems with strong topography. This model can have multiple tidal constituents and multiply connected channels. 2) Development and verification of a new quasi 3-D semi-analytical velocity profile model applicable to estuarine systems which are strongly forced by both oceanic tides and riverflow. This model includes diurnal and semi-diurnal tidal and non-linearly generated overtide circulation and residual circulation driven by riverflow, baroclinic forcing, surface wind stress and non-linear tidal forcing. 3) Demonstration that much of the lateral variation in along-channel currents is caused by variations in along-channel density forcing and bathymetry.

TABLE OF CONTENTS

List of Figures iii

List of Tables vii

Glossary viii

Chapter 1: Introduction 1

1.1 Scope of Thesis 4

1.2 Previous modeling studies 6

1.3 Field Setting 8

1.4 Dissertation Structure 10

Chapter 2: Data Collection and Processing 12

2.1 Data 12

2.2 Data Collection 13

2.3 Data Processing 16

2.4 Data Analysis 18

Chapter 3: One-Dimensional, Barotropic Modeling 28

3.1 One-Dimensional Barotropic Theory 29

3.2 One-Dimensional Barotropic Modeling Approach 33

Chapter 4: Profile Modeling: Development and Verification 37

4.1 Current Modeling Effort 39

4.2 Definition of Flow Modes 40
4.3 Relationship to Previous Studies 43
4.4 Profile Model Formulation 46
4.5 Results 75
4.6 Summary 81

Chapter 5: Lateral Topographic Effects on Along-Channel Flow **84**
5.1 Simulation Matrix 84
5.2 Rectangular Cross-Section 85
5.3 V-Shaped Channel Cross-Section 97
5.4 Irregularly Shaped Channel Cross-Section 100

Chapter 6: Summary **106**

Bibliography **111**

Appendix A: Cruise Information **117**

Appendix B: Density and Velocity Data from South Channel **118**
B.1 Time series 118
B.2 Harmonic data 133

Appendix C: 1-D Barotropic Model **141**

LIST OF FIGURES

1.1 Conceptual block digram of forcing. 5
1.2 Setting map of Columbia River Estuary. 9
1.3 Setting map of Columbia River watershed. 10

2.1 South channel ship track. 14
2.2 Density data time series for station G35b. 15
2.3 Along-channel velocity data for station G35b. 16
2.4 Echo sounder record showing advancing salt wedge. 17
2.5 Comparison of data and harmonic reconstruction. 19
2.6 Time series grayscale figure of harmonically reconstructed velocity. . . 20
2.7 Grayscale image of harmonically reconstructed density time-series. . . 20
2.8 Time series of gradient Richardson number calculated from data at south channel station G35b 21
2.9 Harmonically Analyzed along-channel velocity, Z_0 22
2.10 Harmonically Analyzed density, Z_0 23
2.11 Harmonically Analyzed along-channel velocity, K_1 24
2.12 Harmonically Analyzed density, K_1 24
2.13 Harmonically Analyzed along-channel velocity, M_2 25
2.14 Harmonically Analyzed density, M_2 25
2.15 Harmonically Analyzed along-channel velocity, M_4 26
2.16 Harmonically Analyzed density, M_4 27

3.1 3-D sketch of south channel reach. 29

3.2 Schematic of channel bifurcation. 34
3.3 Channel topography used in 1-D model. 35
3.4 Comparison of data and and 1-D model for D_1 and D_2 height amplitude and phase. 36

4.1 Neutral eddy diffusivity 59
4.2 Stratification correction to the neutral eddy diffusivity 60
4.3 Eddy diffusivity 60
4.4 Sample density forcing function. 69
4.5 South channel section bathymetry. 76
4.6 Model, riverflow circulation. 77
4.7 Model, Gravitational circulation. 78
4.8 Model, non-linear residual circulation. 78
4.9 Model, combined residual circulation. 79
4.10 Total residual flow difference plot. 80
4.11 Model, K_1 band circulation. 81
4.12 Model, M_2 band circulation. 82
4.13 Analytic solution for gravitational circulation. 82
4.14 Profile model solution for gravitational circulation. 83

5.1 1 River flow, rectangular channel, no tidal flats. 86
5.2 1 Gravitational flow, rectangular channel, no tidal flats. 87
5.3 1 Non-linear residual flow, rectangular channel, no tidal flats. 87
5.4 1 Combined residual, rectangular channel, no tidal flats. 88
5.5 1 Diurnal, rectangular channel, no tidal flats. 88
5.6 1 Semidiurnal, rectangular channel, no tidal flats. 89
5.7 2 Gravitational flow, rectangular channel with tidal flats. 90

5.8 2 Non-linear residual, rectangular channel with tidal flats. 91
5.9 2 Combined residual, rectangular channel with tidal flats. 92
5.10 2 Semidiurnal, rectangular channel with tidal flats. 92
5.11 3 River flow, rectangular channel with curvature, no tidal flats. 93
5.12 3 Semidiurnal flow, rectangular channel with curvature, no tidal flats. 94
5.13 3 Non-linear residual, rectangular channel with curvature, no tidal flats. 95
5.14 3 Gravitational, rectangular channel with curvature, no tidal flats. . . 95
5.15 3 Combined residual, rectangular channel with curvature, no tidal flats. 96
5.16 4 River flow, "V", straight, no tidal flats. 97
5.17 4 Gravitationally driven flow, "V", straight, no tidal flats. 98
5.18 4 Combined residual flow, "V", straight, no tidal flats. 98
5.19 4 Semidiurnal, "V", straight, no tidal flats. 99
5.20 4 River flow, irregular, curved to right, no tidal flats. 100
5.21 5 Gravitationally driven flow, irregular, curved to right, no tidal flats. 101
5.22 5 Combined residual flow, irregular, curved to right, no tidal flats. . . 102
5.23 5 Semidiurnal, irregular, curved to right, no tidal flats. 102
5.24 5 Combined residual flow, irregular, curved to left, no tidal flats. . . . 103
5.25 7 Baroclinic, weak density forcing, irregular, straight, wind. 104
5.26 7 Wind driven, weak density forcing, irregular, straight, wind. 105
5.27 7 Combined residual, weak density forcing, irregular, straight, wind. . 105

B.1 Time series of density for Port of Astoria. 119
B.2 Time series of along-channel velocity for Port of Astoria. 120
B.3 Time series of total gradient Richardson number for Port of Astoria. . 120
B.4 Time series of density for G35a. 121
B.5 Time series of along-channel velocity for G35a. 122
B.6 Time series of gradient Richardson number velocity for G35a. 122

B.7 Time series of density for G35b. 123
B.8 Time series of along-channel velocity for G35b. 124
B.9 Time series of gradient Richardson numbers for G35b. 124
B.10 Time series of density for G37. 125
B.11 Time series of along-channel velocity for G37. 126
B.12 Time series of gradient Richardson number for G37. 126
B.13 Time series of density for Pier 11 127
B.14 Time series of along-channel velocity for Pier 11 128
B.15 Time series of gradient Richardson numbers for Pier 11. 128
B.16 Time series of density for G39. 129
B.17 Time series of along-channel velocity for G39. 130
B.18 Time series of gradient Richardson number for G39. 130
B.19 Time series of density for East End. 131
B.20 Time series of along-channel velocity for East End. 132
B.21 Time series of gradient Richardson number for East End. 132
B.22 Hamonically analyzed Z_0 along-channel velocity, along-channel section 133
B.23 Hamonically analyzed K_1 along-channel velocity, along-channel section 134
B.24 Hamonically analyzed M_2 along-channel velocity, along-channel section 135
B.25 Hamonically analyzed M_4 along-channel velocity, along-channel section 136
B.26 Hamonically analyzed Z_0 density, along-channel section 137
B.27 Hamonically analyzed K_1 density, along-channel section 138
B.28 Hamonically analyzed M_2 density, along-channel section 139
B.29 Hamonically analyzed M_4 density, along-channel section 140

C.1 Idealized channel topography for 1-D model. 141

LIST OF TABLES

5.1 Simulation Matrix. 85

C.1 1-D Channel Geometry. 142

GLOSSARY

ADCP: An acoustic Doppler current profiler, (ADCP) measures the velocity profile in a volume of water. It transmits an acoustic signal and then determines the Doppler shift of that signal after it has been back scattered from suspended particulate matter in the water. By gating the returning signal, a two-dimensional horizontal velocity profile is obtained as a function of distance from the profiler.

COLUMBIA RIVER ESTUARY: The portion of the Columbia River in which salt and fresh water are present at some time. Here taken from the mouth to Rkm 60.

CTD: A Conductivity - Temperature - Depth profiler is a device that when lowered in the water column records the temperature and conductivity of the water column as a function of depth.

CRETM: Columbia River estuary turbidity maxima research project.

DIURNAL: See K_1.

ESTUARY: In this paper, estuary refers to the area of where the flow is significantly effected vertical density differences or stratification. This area is important because it is the interface between the ocean and the land.

EULERIAN VELOCITY: The velocity of a flow at a particular point in space.

HARMONIC ANALYSIS: A tidal analysis method in which desired frequencies, known from astronomical principles, are specified and the amplitude and phase shift of

each constituent is determined by a least squares minimization.

INTERNAL CURRENT: A current mode in which the sectionally integrated along-channel transport vanishes. This implies a reversal of direction in a steady current or a 180° phase change in the vertical for a tidal species; such currents have little or no surface expression.

INTERNAL TIDAL ASYMMETRY: Is manifest in the difference, or asymmetry, between the velocity profile of a hypothetical perfectly reversing tide and the actual velocity profile. It arises, for example, when the velocity profile of the ebb is linearly sheared with a surface maximum while there is a subsurface maximum on flood.

K_1: Luni-solar diurnal constituent. Its nominal frequency is 0.0417807462 $\frac{cycle}{hr}$ which corresponds to a period of 23.93 $\frac{hr}{cycle}$.

LMER: Land Margin Ecosystem Research project.

LAGRANGIAN VELOCITY: The velocity of a parcel of fluid as it moves in a flow.

M_2: Principal lunar semidiurnal constituent. Its nominal frequency is 0.0805114007 $\frac{cycle}{hr}$ which corresponds to a period of 12.42 $\frac{hr}{cycle}$.

M_4: Overtide of principal lunar constituent. Its nominal frequency is 0.1610228013 $\frac{cycle}{hr}$ which corresponds to a period of 6.21 $\frac{hr}{cycle}$.

MLLW: Mean Lower Low Water is the average value of the daily lower low waters over a long period of time.

MODE SPLITTING: Separating barotropic and internal calculations.

N (BRUNT-VÄISÄLÄ FREQUENCY): $\sqrt{\frac{-g}{\rho_o}\frac{\partial \rho}{\partial z}}$, is the highest frequency at which internal waves exist in a stratified fluid. It is a measure of the strength of stratification.

NSF: National Science Foundation.

NOS: National Ocean Service.

OBS: An Optical Back Scatter suspended sediment sensor is a device that measures the intensity of its infrared signal back scattered from SPM.

ONR: Office of Naval Research.

PYCNOCLINE: area of the water column where the vertical density gradient or stratification is high.

PSU: Practical Salinity Units

RI_G: Gradient Richardson Number $\frac{N^2}{(\frac{\partial u}{\partial z})^2+(\frac{\partial v}{\partial z})^2}$ is the ratio of density stratification to shear. The domain of Ri is $0 \leq Ri_g \leq \infty$.

RI_{GT}: Total Gradient Richardson Number includes internal wave shear, $\frac{N^2}{N^2+(\frac{\partial u}{\partial z}+\frac{\partial v}{\partial z})^2}$. If there is assumed to be an equipartition of potential and kinetic energy in the internal wave field, then N^2 is an estimate of the (unmeasured) internal wave shear. The domain of Ri_{gT} is $0 \leq Ri_{gT} \leq 1$.

ROSSBY RADIUS OF DEFORMATION: $\frac{NH}{2\Omega}$ where H is the horizontal length scale and Ω is the angular velocity. If the characteristic width of the system is less than the Rossby radius of deformation, then the effect of the Coriolis acceleration on the flow is negligible.

RKM- RIVER KILOMETER: kilometers upriver from the mouth.

SECONDARY CIRCULATION: The lateral circulation caused by channel curvature and other topographic effects.

SEMIDIURNAL: See M_2.

σ COORDINATES: A coordinate system where the local bottom depth is used to scale the position in the water column. $\sigma = 0$ is the bed and $\sigma = 1$ is the surface.

$\sigma_\mathbf{T}$: An expression for density; $\sigma_t = (\rho - 1) \times 1000$, for example, at 0 C, 30 PSU ≈ 1.030 kg m^{-3} $\approx \sigma_t = 30$.

SALINITY: Amount of salt in water expressed in Practical Salinity Units, PSU.

SPM: Suspended Particulate Matter is any thing that is suspended in the water, inorganic or organic, living or not.

USGS: United States Geologic Survey.

Z_0: Mean flow constituent.

ACKNOWLEDGMENTS

This work was supported by several different grants. The data collection, processing and analysis were accomplished as part of the Columbia River Estuarine Turbidity Maximum (CRETM) research project funded by National Science Foundation's Land-Margin Ecosystem Research (LMER) program OCE-94-12028AM02. Model development and validation were funded by the Office of Naval Research (ONR) grant numbers N00014-94-1-0009, *Circulation in Stratified Tidal Channels and Straits,* and N00014-97-1-0625, *AASERT – Internal Circulation in Tidal Channels and Straits: a Comparison of Observed and Numerical Turbulence Estimates.* I would like to thank my advisor, David A. Jay and the members of my reading and supervisory committees: Drs. Marcia Baker, John Booker, Thomas Sanford and H. Paul Johnson.

I would especially like to thank my wife Wendy for her support, encouragement and understanding. She made this accomplishment possible.

Chapter 1

INTRODUCTION

Estuaries provide vital habitat for a wide range of organisms and are the main interface between humans and the oceans. The most common definition of an estuary is "... a semi-enclosed coastal body of water which has a free connexion with the open sea and within which sea water is measurably diluted with fresh water derived from land drainage", Cameron and Pritchard [1]. More broadly, an estuary is a tidally influenced basin, strait or channel in which fresh water and salt water mix, perhaps including a tidal fresh water portion. Along-channel circulation in an estuary has a profound, if not controlling, influence on the organisms, particles and even the bathymetry in the estuary. The systems of particular interest here are those with a well-defined axis of tidal propagation and fresh water discharge; "narrow" will be formally defined below.

There are several ideas about estuaries that are used in this work:

- The first step in understanding the overall three-dimensional (3-D) circulation in estuaries is to understand the along-channel momentum balance, as it dictates the structure of the along-channel flow field which in turn controls transport phenomena in the estuaries of interest here. Determining the longitudinal momentum balance is an intriguing problem because it is complex and has far reaching effects.

- Some of the most interesting areas in estuaries are those where, by flow or

topography, particulate matter is concentrated, these areas are called estuarine turbidity maxima (ETM). The particulate matter, organic and inorganic, in an ETM is resuspended and advected when velocities are high enough and settles out when it is not.

- As a starting point, the circulation in an estuary can be thought of as follows: Sea water flows upstream under the fresh water to the stagnation point where this up-stream flow is balanced by the down-stream riverflow. The fresh water, which is flowing seaward, entrains sea water into the fresh/salt water interfacial layer and transports the salt back to the ocean. This outflow, being less dense than the sea water, spreads out on the surface of the ocean to create a river plume.

- In the absence of tides and wind, an estuary would reach this steady state involving two circulation modes: river outflow and gravitational, or baroclinic, circulation. Once ocean tidal forcing is included the situation becomes more complex, and several new internal circulation processes, or modes, appear.

- Two of these new modes include contributions to the mean flow: 1) a Stokes drift compensation flow and 2) internal tidal asymmetry (ITA). There is also a contribution to the over-tide mode from ITA. The Stokes drift is caused by tidal correlations of velocity and channel area. That is, at tidal frequencies, more water is moved up-river during the flood than is moved down-river during the ebb. The Stokes drift compensation flow is simply this water moving back down-river. Two aspects of the mechanism responsible for ITA are: "1) differential tidal advection of a strong horizontal density gradient causes tidal variations in stratification and thus vertical turbulent mass and momentum exchange. And, 2) baroclinic and barotropic forcing of the same sense on flood but contrary on ebb", Jay and Musiak [29]. Which act together through vertical momentum

exchange to manifest themselves as internal residual and overtide flows. On flood, the currents act on the density field to make the isopycnals more vertical and horizontally compress them, increasing the bedstress. During ebb, the stratification is increased causing the flow to be highly sheared near the surface, decreasing the bedstress. This causes the resulting Eulerian currents to not exactly reverse at each depth, thus generating the internal flows. These currents are internal in that they do not have a surface expression and, the overtide flow, since it may not produce any net transport, must exhibit a 180° vertical phase reversal.

The importance of estuarine circulation is clearly demonstrated by some of the results from the Columbia River Estuary Turbidity Maxima (CRETM) research program, which is funded by the National Science Foundation (NSF) as part of its Land Margin Ecosystem Research (LMER) project; LMER was developed to investigate scientific and societal aspects of coastal environments. The main goal of CRETM is to "understand how circulation phenomena in the estuary, called estuarine turbidity maxima (ETM), trap particles and promote biogeochemical, microbial and ecological processes that sustain a dominate pathway in the estuary's food web." Some of the interesting results from the CRETM program [50] include: 1) identifying a new mode of estuarine circulation which plays an major role in ETM formation, Jay and Musiak [29]; 2) determining the role of particle-attached microbes in the ETM food chain Crump et. al. [2]; 3) demonstrating the variability in particle processing on tidal daily and tidal monthly time scales; and, 4) describing how different species of copepods use estuarine circulation to survive, Morgan et. al. [37]. These examples demonstrate that understanding the 3-D structure of the flow field of an estuary is necessary to understanding of the chemical and food web processes and that take place in an estuary.

Thus, it is important to have a well-founded understanding of the flow dynamics

of estuaries, laying the groundwork for comprehending the movement of sediment and other particulate matter in estuaries and the life-cycles of the organisms that make their homes here. To that end, this work introduces a new class of 3-D model for calculating the along-channel circulation of estuaries which are strongly forced by both riverflow and oceanic tides. The primary hypotheses of this work are that 1) most of the lateral variability of the along-channel circulation in an estuary is caused by lateral variations in depth and consequently in vertical mixing. And, 2) along-channel scaler transport can largely be understood without quantifying the complexities of lateral circulation.

This chapter explains the goals of and motivation behind this work and describes how these goals were met. A brief introduction to the study area as well as an outline of the rest of the thesis is also included here.

1.1 Scope of Thesis

The primary hypotheses put forward in this work is that most of the lateral variability of the along-channel estuarine circulation in a straight channel is caused by lateral variations in depth directly or indirectly effecting the flow. In a curved channel, the curvature must be accounted for just as in a fluvial flow. To test this hypothesis the longitudinal momentum balance in the Columbia River estuary (CRE) is calculated and analyzed taking into account riverflow, oceanic tidal forcing, density forcing, topography, bathymetry, channel curvature and non-linear flow effects. To accomplish this, a new class of 3-D estuarine model is introduced. This new diagnostic modeling scheme incorporates several different flow processes: barotropic tides in a channel of variable width and depth, baroclinic circulation and, profile models of tidal flow, residual flow and non-linearly driven residual and overtide flow.

The model is validated using velocity and density measurements from the Columbia River and estuary and comparisons to analytical results. The circulation in the CRE,

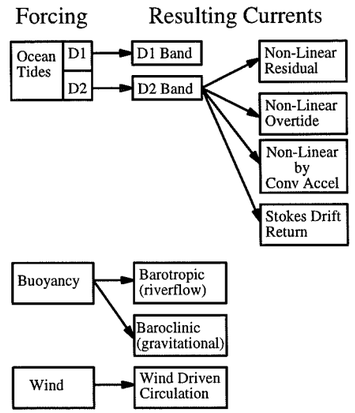


Figure 1.1: Block digram showing some of the forcing and resulting flow modes possible in an estuary.

which is typical of strongly forced estuaries, is complex; it is 3-D, time dependent, stratified and yet partially turbulent. The system is further complicated by multiple channels of variable width and depth with tidal flats that are not always wetted. An ideal tactic to use to investigate this type of system would be to analyze a reach where the channel was straight, narrow, of constant rectangular cross section. The effects of channel curvature, Coriolis acceleration, branching channels, tide flats, variations in channel width and bottom topography could then be neglected, allowing time-dependent stratified flow to be studied in the absence of topographic complications. Data interpretation and modeling would be straight forward. After this simple system was understood, increasingly more complicated sections would be modeled. Unfortunately, such an ideal section of the estuary does not exist. There are several reaches in which some or most of the complications can be initially ignored. Beginning with these sections, data interpretation and modeling took place iteratively. By using data and models together in this manner, a more complete description of an estuary is obtained than only using one or the other. This approach is used because

without verification models are of limited utility and without determining the physics of a system through modeling, data are solely descriptive.

The data used to verify this model are from the CRE; nevertheless, the models herein developed should be applicable to many other estuaries that are at least moderately forced by riverflow and tides. This new class of model is necessary to gain a conceptual understanding of strongly forced estuaries by calculating the different flow modes separately, the flow physics important in different areas of actual flow systems can then be determined. This model will also help to distinguish lateral variability in the along-channel flow generated by lateral variations in depth from the effects of lateral flow.

1.2 Previous modeling studies

Estuarine circulation is a complex problem, accordingly most previous modeling efforts have focused on a single facet of estuarine circulation, or neglected part of the system to make the problem tractable. The principal theory of time-averaged estuarine circulation was established by Hansen and Rattray [16]. They calculated circulation profiles for two estuarine regimes in a narrow channel of constant rectangular cross-section, using a steady longitudinal momentum balance between a horizontal pressure gradient and shear-stress. The two areas are: 1) The central regime, where the vertical density stratification and the horizontal density gradient are almost independent of position; and, 2) the inner regime, where the vertical density stratification is proportional to the sectional averaged salinity. The models are formulated using the assumption that the tidal currents are the primary cause of vertical mixing and transport salt landward (as express through a horizontal eddy diffusivity) but do not influence the flow in any other way. It is also assumed that river discharge, wind stress and density driven circulation are all important, but linearly independent factors creating residual circulation and thus in determining the salinity distribution

in an estuary. These studies also emphasize the coupling between the density and velocity fields of an estuary.

The next major step in estuarine circulation modeling was taken by Ianniello [19] & [20]. He first derived 2-D analytic solutions, as a function of depth and longitudinal distance, for the Eulerian and Lagrangian residual currents induced in narrow tidal channels of constant breadth, depth and rectangular cross-section by the non-linear interaction of first order tides. Perturbation analyses valid for weakly non-linear systems, $\varepsilon = \eta_0 h_0^{-1} \ll 1$, ($\varepsilon$ is the small-amplitude wave non-linearity number), where η_0 is the tidal wave amplitude and h_0 is the channel depth, were used so that the tidal and residual circulation could be partially de-coupled. By retaining the full depth dependence of the tidal driving terms he showed that previous analyses of the problem, based on boundary layer approximations, were not valid for realistic channel depths and eddy viscosity profiles. Ianniello also presented another major step in estuarine modeling — inclusion of non-linear production of steady second order residual currents by the first order tidal flow in a 2-D model. The momentum balance used is the time rate of change of momentum, vertical and longitudinal convective accelerations, horizontal pressure gradient and shear-stress.

Ianniello [20] further derived analytic solutions of "longitudinal and across-channel Eulerian and Lagrangian residual currents induced in narrow tidal channels of variable width, breadth and depth, of rectangular cross-section, by the non-linear interaction of first order tides." Again, these solutions are valid as long as the system is weakly non-linear, $g\eta_0\omega^{-2}\Delta x^{-2} \ll 1$ and as long as the breadth variations are sufficiently gradual that $fb_0\omega^{-1}\Delta x^{-1} \ll 1$, where the variables are: η_0 tidal amplitude; ω tidal frequency; Δx is the length scale over which the breadth changes; f is the Coriolis parameter; b_0 is the channel width and g is the acceleration due to gravity. As expected the results show significant differences in the residual circulation patterns between channels of varying cross-section and those of constant breadth and depth, illustrating the importance of using realistic bathymetry.

The importance of the lateral variability of along-channel residual circulation in determining the density field in estuaries has been shown by Pritchard [44] & [46], Hansen and Rattray [16], Wong [54] and others. Hansen and Rattray [16] and Officer [41] presented the analytic model for the gravitational circulation mode: the tidally averaged horizontal pressure gradient balanced by the the vertical shear stress. Where previous studies solved this model for a rectangular channel, Wong [54] re-solved the problem for a more realistic V-shaped channel, showing upstream flow in the deepest part of the channel while downstream flow of fresher water persists at the edges of the channel.

These previous modeling efforts demonstrate the usefulness and applicability of analytic models to estuarine systems. Another important aspect of these analytic models is that their scaling gives insight into what the dominant physical processes are. The ability of 3-D numeric models to more accurately portray actual estuarine topography is enticing, but the inherent loss of some physical insight may not be an acceptable trade off in all cases. There is clearly an opening for a model that can incorporate more realistic channel geometries than possible in purely analytical models while not shrouding the physical processes. It is the purpose of this dissertation to present a model of this type.

1.3 Field Setting

As previously stated, an estuary is the volume where fresh water and salt water mix. Here, a large number of species spend some or all of their life. The liefcycle of such organisms as well as much of the transport of nutrients, chemical, detritual and sediment load en-route from the river to the ocean are effected, if not controlled, by estuarine currents. The sediment, when deposited or eroded, influences the flow field which in turn effects the topography of the estuary.

The CRE, Figure (1.2), is the portion of the Columbia River from the mouth to

approximately Rkm 60, the point of maximum observed salinity intrusion. The

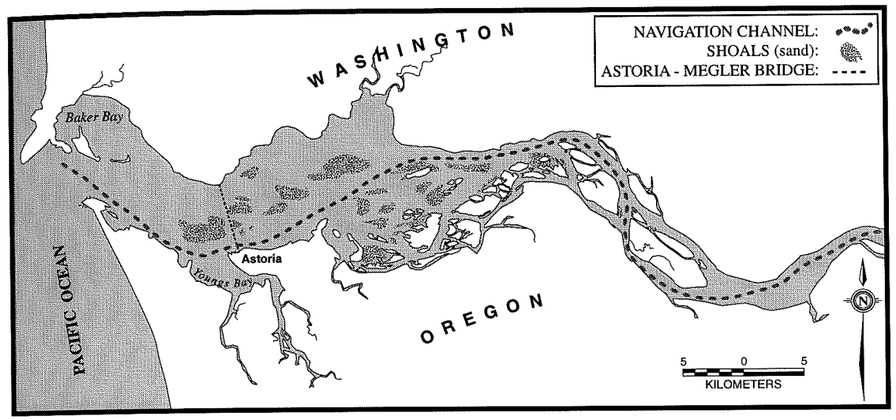


Figure 1.2: Setting map showing the Columbia River estuary. The navigation channel is shown as a dotted line, land is white and mud flats are dark gray.

Columbia River, Figure (1.3), is the the second largest river in the contiguous United States with nearly 1,200 km of its 1,936 km length within the U.S. Starting at Columbia Lake, B.C. at 809 m above sea level, the bed of the Columbia River falls to 18 m below sea level downstream of Bonneville Dam. It's drainage area is 671,000 km^2, over 7 states: Idaho, Montana, Nevada, Oregon, Utah, Washington and Nevada, and 2 Canadian Provinces: British Columbia and Alberta. Before the construction of over 100 dams on the Columbia River, average riverflow is estimated to have been 1,980 m^3s^{-1} from September through March and 18,690 m^3s^{-1} from May through July, with a daily minimum of 1,000 m^3s^{-1} and a maximum of 34,000 m^3s^{-1}, Neal [38]. The present riverflow has an average of 6,500 m^3s^{-1} with minimum and maximum flows being 2,500 and 25,000 m^3s^{-1}, Jay [23]. The tides in the estuary are mixed with a maximum range of approximately 4.0 m. The semidiurnal tidal height has a typical amplitude of 1.0 m while the diurnal amplitude is 0.4 m. The river is split into two main channels from Rkm 10 through 40 by extensive tide flats. The

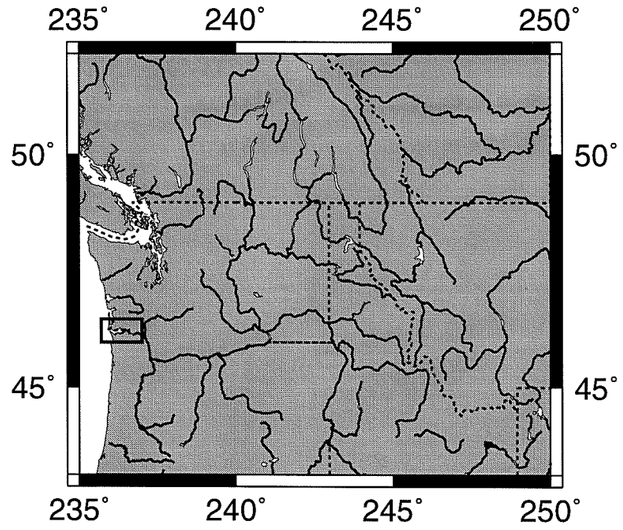


Figure 1.3: Setting map showing the drainage system of the Columbia River. The Columbia River Estuary is highlighted with a box. The borders of the states and provinces are shown as dotted lines.

southern channel has been designated as the main navigation channel and is dredged to a depth of 13.7 m. There are also several large embayments in the river.

The CRE was chosen as a research site because it is part of a dynamically interesting system that has numerous, often conflicting, uses e.g.: commercial fishing, navigation, power generation and irrigation.

1.4 Dissertation Structure

The layout of the this dissertation is as follows: Chapter 1 presents an introduction to estuarine circulation modeling along with the main hypotheses put forward in this work and the basic field setting. Chapter 2 presents the data used in this study detailing how it was collected, analyzed and presented. Chapter 3 describes the theory,

implementation and validation of a 1-D barotropic tidal model used to determine the progression of tidal waves in the estuary. Chapter 4 describes the theory and development of the 3-D Profile model which calculates profiles of along-channel velocity in an estuary. This chapter also presents comparisons of model results to velocity data and analytical calculations. Chapter 5 discusses the effects that channel depth, shape, curvature, surface wind stress, stratification and the presents of tidal flats have on the the different flow modes through simulations. And, finally, Chapter 6 presents what has been learned from work and some possibilities of the future direction. The appendices include information on the cruises, velocity, density and Richardson number data along with the harmonically analyzed velocity and density data.

Chapter 2

DATA COLLECTION AND PROCESSING

This chapter describes the data that are used in this project. Some data are from outside sources, but most are from acoustic Doppler current profiler (ADCP), conductivity-temperature-depth profiler (CTD) and echo sounder surveys compiled as part of the CRETM project in 1990 through 1992. The following sections describe what and how data is collected, processed, modeled and analyzed.

2.1 Data

The primary measurements necessary for completing this project are: along-channel velocity (u), across-channel velocity (v), density (ρ), channel depth (h), channel width (b), tidal height (ζ) and river transport ($Q_{river} = h\,b\,u_{river}$). These data were collected as follows: A vessel mounted ADCP was used to measure the along- and across-channel velocities while a CTD measured temperature and salinity from this, density profiles were obtained. A 200 kHz acoustic echo sounder was used to record bathymetry and a qualitative view of stratified flow dynamics. Tidal height (ζ) for cruise periods was predicted for the Tongue Point station, from data collected in the estuary in 1980-81 and 1991 (CREST) [23], these predictions were spot checked against National Ocean Service (NOS) predictions each year. River transport (Q_{river}) was obtained in two different ways: a) Until 1991, runoff at Bonneville and the flow of the Willimatte were obtained from the U.S. Geologic Survey (USGS) and an empirical relation [23] determined the river transport at the mouth. And b) after 1991 the USGS measured the river transport was measured at Rkm 85 with an acoustic

travel time gauge. Bathymetry was obtained from direct measurement with a 200 kHz acoustic echo sounder and from hydrographic surveys performed by the U.S. Army Corps of Engineers (COE) and NOS.

2.2 Data Collection

Three cruises were conducted in the CRE, (see Appendix A): 1) fall 1990, which had a river runoff of $\sim 3,800\ m^3 s^{-1}$, 2) summer 1991, with a runoff of $\sim 6,900\ m^3 s^{-1}$ and 3) spring 1992, at $\sim 6,600\ m^3 s^{-1}$. These cruises were planned to sample the different runoff conditions at different times of the year but all fall in the low to moderate flow range. On each of these cruises, the data collection scheme was as follows. Interesting areas of the estuary were chosen based on physical, biological or chemical criteria. A data collection pattern for that area was selected based on topography, vessel logistics and oceanographic characteristics. ADCP data were continuously collected while transiting a pattern consisting of 4 to 6 CTD stations. The station pattern was chosen to sample along- or cross-channel variations or both. At each CTD station the vessel held position and the CTD was used to sample the temperature and conductivity field. The ship track used for data collection, with CTD stations marked, is shown in Figure (2.1) for the south channel section. The entire circuit was completed at least once an hour for at least 30 hours. Sampling each station at least once an hour enables the resolution of frequencies, by the Nyquist criteria, up to the M_8 band (eighth diurnal), period 3.1 hours, to be resolved. And, by continuing sampling for 30 hours encompassed an entire tidal day, $2 \times Period_{M_2} = 24.8$ hours.

The area discussed in this work is the south channel section which is is characterized by a single channel that is 0.8 to 1.5 km wide from shore to the 3 m contour of the shoals. This channel consists of two relatively straight sections with a 6 km radius bend at Rkm 34. This section is interesting because an ETM associated with the upstream limits of salinity intrusion is here and because of the topography; There

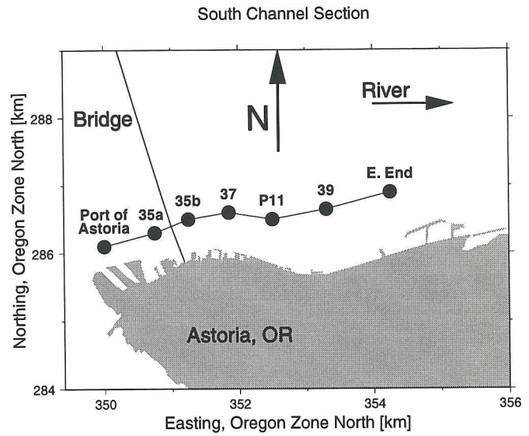


Figure 2.1: South channel ship track (line) and CTD stations (circles). The station names are shown above each station.

is a hole downstream of a topographic high. For this 4.8 km long section, there are 7 CTD stations, each with a corresponding ADCP station. Time series of the density (ρ), expressed as sigma-t ($\sigma_T = 1000 \times (\rho - 1)$), and along-channel velocity are plotted for each station in Appendix B. Time series plots of density and along-channel velocity for station 35b are shown in Figures (2.2) and (2.3). Figure (2.2) shows multiple time series of density with depths corrected to Mean Lower Low Water (MLLW). The slightly irregular bottom results from steep bed topography and imperfect vessel positioning. The denser salt water can be seen as it is advected in near the bottom and subsequently fills the water column and eroding from the surface on ebb. A diurnal tidal height inequality can be is observed where successive high and low tides are not of the same amplitude. This this is most evident in that the salt is washed out to varying degrees on different ebbs and is only washed out completely on one of the seven ebbs shown. In addition to these 7 CTD stations, a further 19 ADCP stations (26 total) were interspersed between the CTD stations. The velocity stations were 185 m long and 200 m wide. Velocity data collected anywhere in a

box was treated as though it was collected at the center point of the box. Greater resolution in the ADCP data is possible because the ADCP samples constantly as the boat moves through the water whereas the CTD must be physically lowered through the water to collect data.

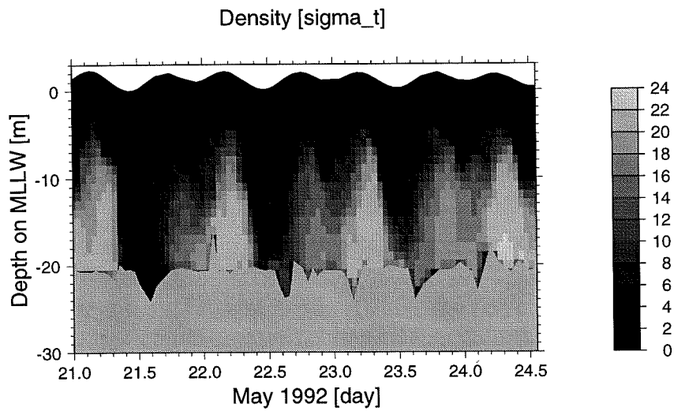


Figure 2.2: Time series of density data, in σ_T units, for south channel station 35b. On flood, the denser salt water moves up-stream near the bottom. As the flood progresses, the landward flowing sea water occupies more of the water column. On ebb, the saltwater is eroded from the top down. On the smaller ebb tides the saltwater is not completely washed out past this station.

Echo sounder records provide a valuable quantitative view of the density field, mixing processes and advance and retreat of the salt water. As an example, Figure (2.4), shows a salt wedge advancing to the left. Time series from anchor stations as well as along-channel transects showed these phenomena clearly. The salt wedge can be seen thickening just before it flows down slope, thinning as it does, and then thickening at its head. The phenomenon of the salt wedge thickening as it goes over a topographic high is very significant and will be discussed later.

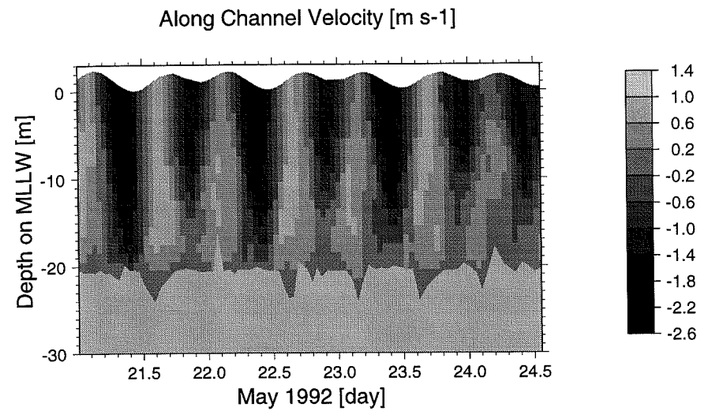


Figure 2.3: Time series of along-channel velocity data in $m\ sec^{-1}$ for south channel station 35b. On flood, the up-stream flow starts first near the bottom and moves higher in the water column later in flood. On ebb the down-stream flow starts at the surface and moves lower in the water column during ebb. down.

2.3 Data Processing

Most of the data processing which is presented here is novel. Geyer and Signell [11] used a similar method to examine the tidal flow around a headland. Their method was to divide the ship tracks into 200 m bins and then vertically average each bin so there was only one time series per box; they did not collect CTD data because stratification was negligible in their system. Geyer [10] investigated the 3-D structure of tidal flow around a headland and presented instantaneous snapshots of velocity but didn't generate time series in depth. My typical ADCP and CTD data processing scheme is to Segregate, Correct to datum, Rotate to coordinate system, and Decompose into harmonic constituents. Each of these steps is explained in more detail: 1) Segregate: The ship track is divided into horizontal boxes approximately 100-200 m on a side and the ADCP data from each box is selected. The CTD data is segregated by station. 2) Correct to datum: All depth measurements are corrected from depth

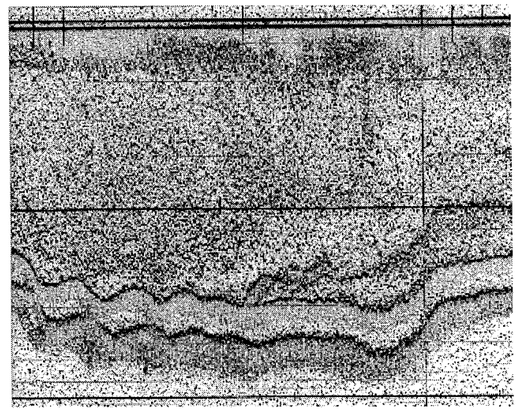


Figure 2.4: Part of an along-channel transect showing the advancing salt wedge. This data was collected on 30 May 1992 around 0400 PST in the south channel at Rkm 24, the surface is ebbing at approximately 2 ms^{-1} even thought the salt wedge is advancing along the bottom. The ocean is to the right; upriver to the left. The tick marks along the top are spaced at 1 minute intervals, the speed of the ship over ground was 5.5 ms^{-1}, or 330 m per tick. The top line is the water surface, the next line down is the transducer. The vertical scale is 30.48 m from the top straight line to the bottom straight line.

from surface to depth from MLLW. 3) Rotate: The velocity data is converted from a compass coordinate system to along- and across-channel components. 4) Decompose: The resultant time series, u, v and ρ are decomposed into amplitudes and phases for specific tidal frequencies. Harmonic analysis was used because the desired frequencies are well known allowing better frequency resolution than Fourier analysis. Harmonic analysis is also tolerant of unevenly spaced data. To show that the harmonic analysis package is able to model the data, a fit of the harmonic reconstruction to the data is shown in Figure (2.5); showing fits to the along-channel velocity for two separate time series, one dense in data and one sparse in data. Harmonic decomposition was very effective in this case despite the potential difficulties described by Jay and Flinchem [28], because the tidal signal is much stronger that in the near sub-tidal. Even so, the left hand panel in Figure (2.5) shows the tidal monthly variation in the tidal signal evolving over the time series; harmonic analysis under predicts the minimum and maximum velocities in the beginning of the series and over predicts them by the end of the series.

2.4 Data Analysis

The vessel mounted ADCP provides high quality velocity data at a rate of approximately 0.1 Hz. It allows horizontal resolution, after averaging, of $100 - 200$ m and a vertical resolution of 1 m. I use two primary formats to look at this data: time series grayscale maps and sections of harmonic constituents.

Time series grayscale maps of along-channel velocity, across-channel velocity and density show how the velocity and density fields change over a tidal day. Figure (2.6) is a grayscale map showing a time series of harmonically reconstructed along-channel velocity collected at station 35b in the south channel section, corresponding to Figure (2.3). This figure shows that the flood starts at mid-depth and moves up in the water column as it intensifies while the ebb begins at the surface and involves

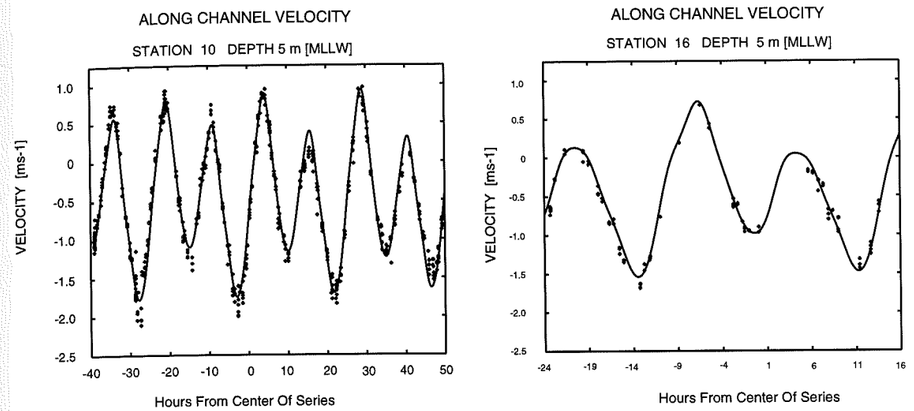


Figure 2.5: Comparison of data and harmonically reconstruction of along-channel velocity from 9 constituents: Z_0, K_1, M_2, MK_3, M_4, $2MK_5$, M_6, $3MK_7$, M_8. The plots show that time series' both A) dense, Rkm 22.8, 20-24 May, 1992, and B) sparse, Rkm 23.5, 23-24 May, 1992, in data is fit well by harmonic analysis.

successively deeper layers as the pycnocline is advected and mixed away. Figure (2.7) is the corresponding grayscale map of density, and shows the behavior of the density field over a tidal cycle, see Figure (2.2). Salt water is not always completely washed out during ebb, see Figure (2.7) day 22.9 through 23.2, 24.0 through 24.3 and day 21.8 through 22.2 where it is even more pronounced.

By combining the velocity fields and density fields, the gradient Richardson number, $Ri_g = \frac{N^2}{S^2}$, which is the ratio of the energy needed to overturn a parcel of water to the kinetic energy that is available in the flow to overturn a parcel of water. Where N^2 is the Brunt-Väisälä Frequency and $S = \sqrt{(\frac{\partial u}{\partial z})^2 + (\frac{\partial v}{\partial z})^2}$ is the vertical shear. The total kinetic energy that is available in the flow to overturn a parcel of water includes energy from internal waves and is included in the total gradient Richardson number: $Ri_{gT} = \frac{N^2}{N^2+S^2}$, after Geyer [9]. This formulation is used because ADCP's underestimate the shear by only measuring the low-frequency shear. Including N^2 in the denominator is an attempt to estimate the missed high-frequency (internal wave)

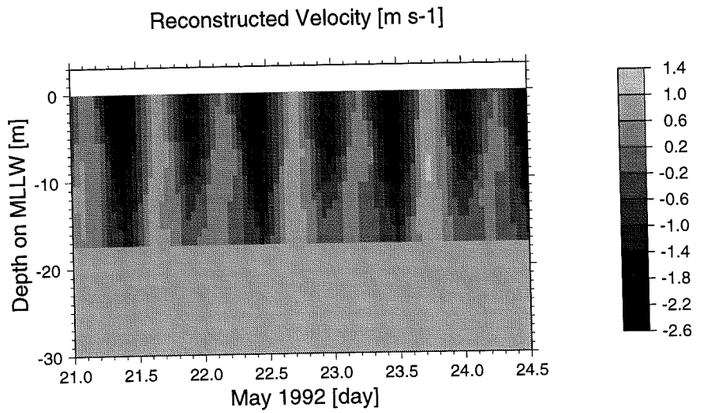


Figure 2.6: Grayscale figure showing time series of harmonically reconstructed along-channel velocity.

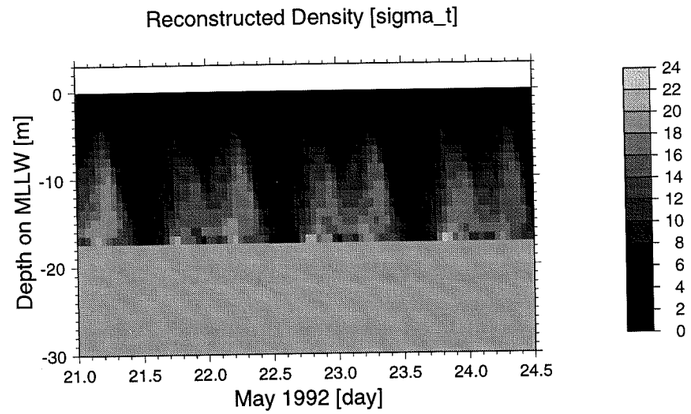


Figure 2.7: Grayscale image showing time series of harmonically reconstructed density, in σ_T units.

energy by assuming that there is an equipartition of energy in the internal wave field.

Figure (2.8) is a grayscale map of $Ri_{gT} = \frac{N^2}{N^2 S^2}$ corresponding to Figures (2.7) and (2.6). The areas where the fresh and salt water are mixing can most easily be seen from day 21.3 to 21.7 in Figure (2.8). At day 21.4, the density interface is very near the bottom in Figure (2.7) and is moving higher in the water column as the flood progresses. This is reflected in Figure (2.8) at day 20.4 as a band of critical Ri_{gT} moving up in the water column during flood until day 21.7 when the density interface starts to descend during ebb until day 22.0 when the process starts over again. As the denser sea water starts moving up stream the density stratification, N^2, increases making the interface more stable, but at the same time the vertical shear, S^2 increases. This provides the necessary energy for mixing to occur across the interface. Figure (2.8) corresponds to Figures (2.2), (2.3), (2.6) and (2.7).

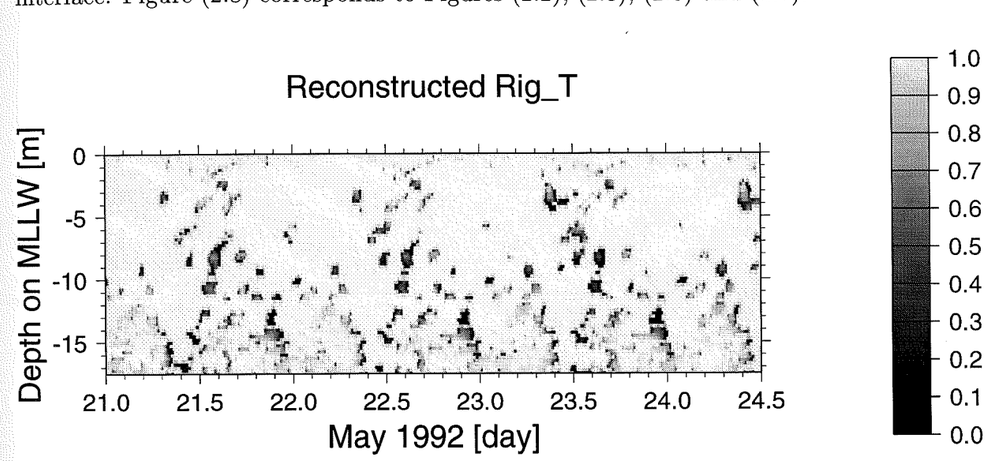


Figure 2.8: Time series of gradient Richardson number calculated from data at south channel station G35b

Another useful data presentation format is spatial sections of harmonic constituents. For these figures, a time series of ADCP or CTD data is broken into time series for each depth which are harmonically analyzed. The individual amplitudes and phases

are recombined into along- or across-channel sections and contoured. By comparing sections of density and velocity a given frequency, the interaction between these fields can be observed. Figures (2.9) and (2.10) are along-channel sections of the mean, or Z_0, amplitude of along-channel velocity $[ms^{-1}]$ and density in σ_T units. These plots are from data collected in the south channel of the CRE, Rkm 21 through Rkm 25.5 on 20-24 May, 1992 (see the ship track in Figure (2.1)). The ocean is to the left and the river to the right. Comparing Figures (2.9) and (2.10) it is clear why the 2 isolated areas of positive, upstream, near-bed flow are present at $2,100$ and $2,400\,m$. The along-channel density gradient changes sign and thickens as the salt water mass moves up river, over the hump and thins out down the back side.

2.4.1 Data Presentation

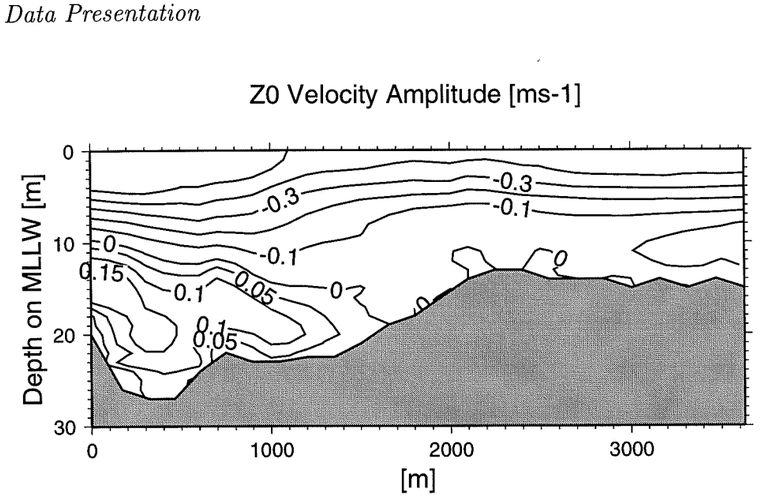


Figure 2.9: Along-channel section of the Z_0 constituent of along-channel velocity. This data was collected in the south channel from Rkm 21 through Rkm 25.5 on 20-24 May, 1992.

The amplitude of the diurnal current, Figure (2.11), shows the area of greatest amplitude in the deepest section of the channel at mid depth. The velocity amplitude

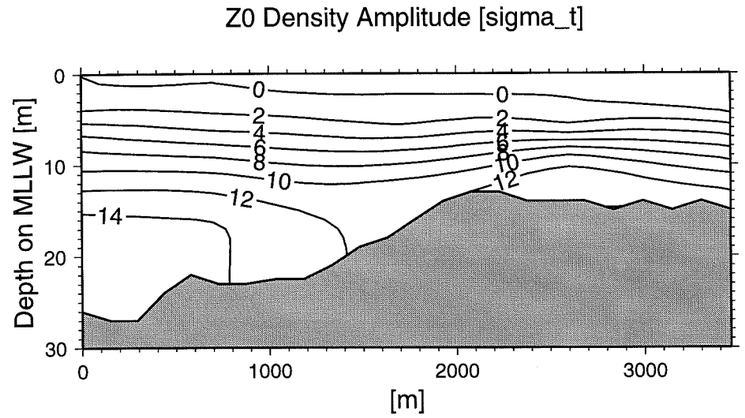


Figure 2.10: Along-channel section of the Z_0 constituent of density, in σ_T units. This data was collected in the south channel from Rkm 21 through Rkm 25.5 on 20-24 May, 1992.

also tends to decrease up-river away from the driving source at the mouth. The diurnal density field, Figure (2.12) diminishes upstream and, in fact can be seen, approaching zero at the upstream limits of salinity intrusion for this time series. The semidiurnal fields of velocity amplitude, Figure (2.13), and density, Figure (2.14), have similar characteristics to the diurnal case. The semidiurnal velocity amplitude is greater and the area of maximum extends to the surface but still decreases up river. The semidiurnal density field exhibits some interesting features. In the deepest part of the channel, a local topographic high, at 700 m into this section, produces an area of decreased density variation. This most likely occurs because the advancing salt water is blocked by the topographic feature without extensive mixing. While in the shallower section of the channel, another local topographic high, along-channel position $2,300$ m, causes a marked increase in the variation of this density field. This is caused by tidally pulsed mixing. The amplitude of the velocity at M_4, principal overtide, frequency, Figure (2.15), has a more complex pattern than the other modes.

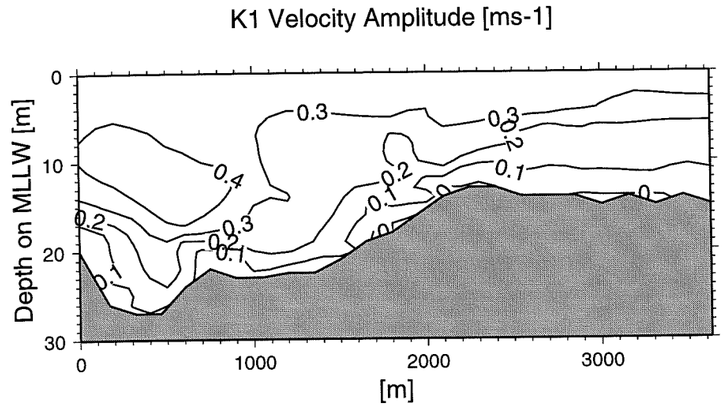


Figure 2.11: Amplitude of along-channel K_1 band velocity. This data was collected in the south channel from Rkm 21 through Rkm 25.5 on 20-24 May, 1992.

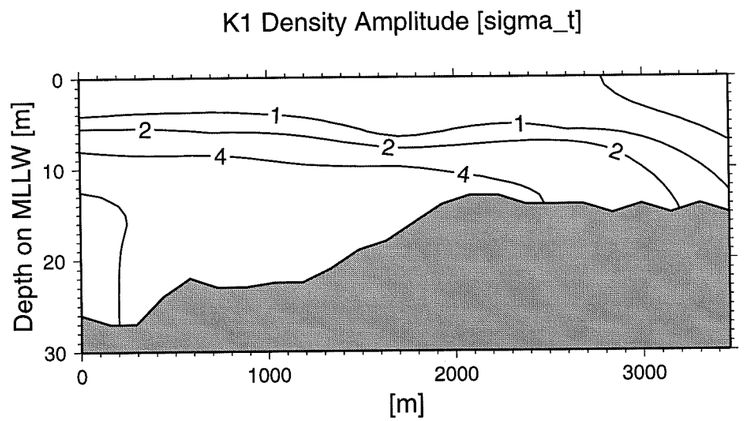


Figure 2.12: Amplitude if the K_1 band density field expressed in σ_T units. The maximum and minimum contours shown are 6 and 0 σ_T units. This data was collected in the south channel from Rkm 21 through Rkm 25.5 on 20-24 May, 1992.

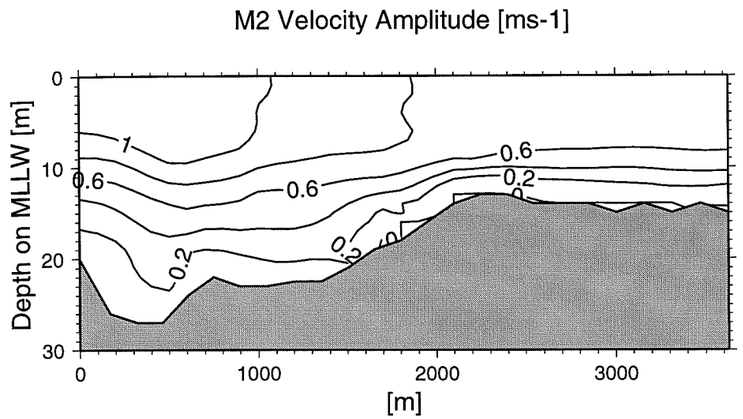


Figure 2.13: Amplitude of along-channel M_2 band velocity. This data was collected in the south channel from Rkm 21 through Rkm 25.5 on 20-24 May, 1992.

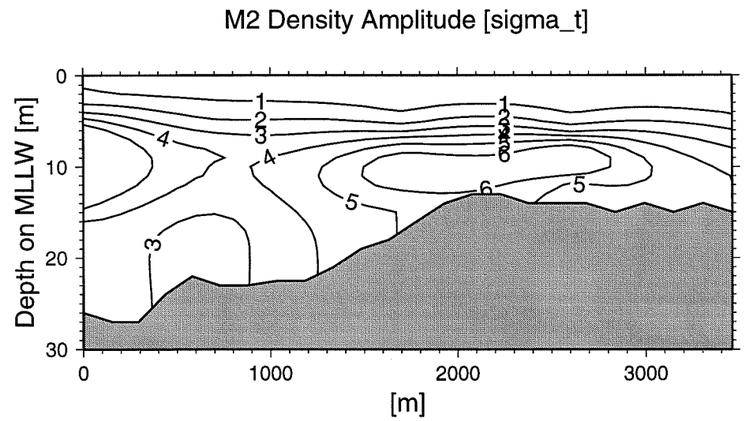


Figure 2.14: Amplitude if the M_2 band density field expressed in σ_T units. This data was collected in the south channel from Rkm 21 through Rkm 25.5 on 20-24 May, 1992.

The first thing to notice is that the maximum amplitude is slightly over 0.12 $cm\ sec^{-1}$, this is twice as large as the currents that would be driven by the M_4 tidal height forcing at the mouth, and is evidence of internal tidal asymmetry, Jay and Musiak [29]. The velocity amplitude has its maximum at mid depth along most of the channel. The M_4 density field, Figure (2.16), has its maximum slightly higher in the water column than that of the velocity. The density field also has variation maximum located over the major topographic high.

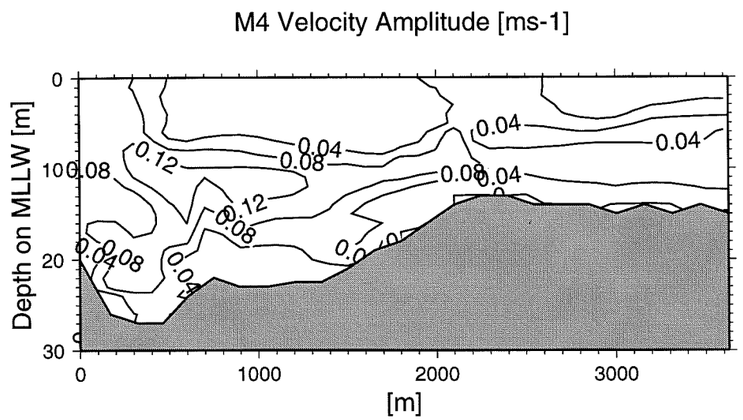


Figure 2.15: Amplitude of along-channel M_4 band velocity. This data was collected in the south channel from Rkm 21 through Rkm 25.5 on 20-24 May, 1992.

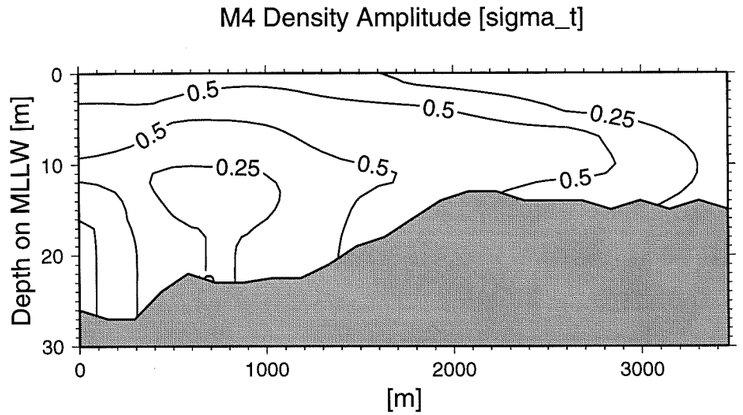


Figure 2.16: Amplitude if the M_4 band density field expressed in σ_T units. This data was collected in the south channel from Rkm 21 through Rkm 25.5 on 20-24 May, 1992.

Chapter 3

ONE-DIMENSIONAL, BAROTROPIC MODELING

The overall strategy is to use the one-dimensional (1-D) model developed in this chapter to calculate the tidal wave propagation in the estuary which in turn will be used to drive the velocity profile model developed in Chapter 4. The 1-D model is posed in terms of sections where the width, total width (including tidal flats) and depth are allowed to independently remain constant, exponentially increase or exponentially decrease with x (along-channel distance) thus allowing system topography to be realistically portrayed.

Circulation in the Columbia River and many other estuaries can be described as a frictionally dominated flow over strong topography. Modeling this type of system necessitates the accurate representation of friction, density field and bathymetry if a model is going to represent the system correctly. To accurately determine the friction factors and tidal long-wave propagation a 1-D barotropic model, following the ideas of Giese and Jay [12] and Jay [27], was used. This model was extended to include the K_1 tidal band in addition to the M_2 band with multiply connected channels. This 1-D barotropic model is used to determine the wave numbers of the K_1 and M_2 band tides along with scale velocities and friction factors for the final 150 km of the Columbia river. These values are then be used to drive 3-D profile model described in the next chapter. The model is validated using M_2 tidal height, amplitude and phase, data collected in the CRE in 1980-81 as part of the CREST [23] project.

3.1 One-Dimensional Barotropic Theory

In a 1-D estuarine model, the density, along-channel velocity and depth are cross-sectionally averaged, making them functions solely of along-channel position and time (x and t). Figure (3.1) is a 3-D sketch of the south channel reach showing the coordinate system used. X is the along-channel (stream following) axis, Y is the across-channel (perpendicular to X) axis and Z is the vertical axis. A barotropic

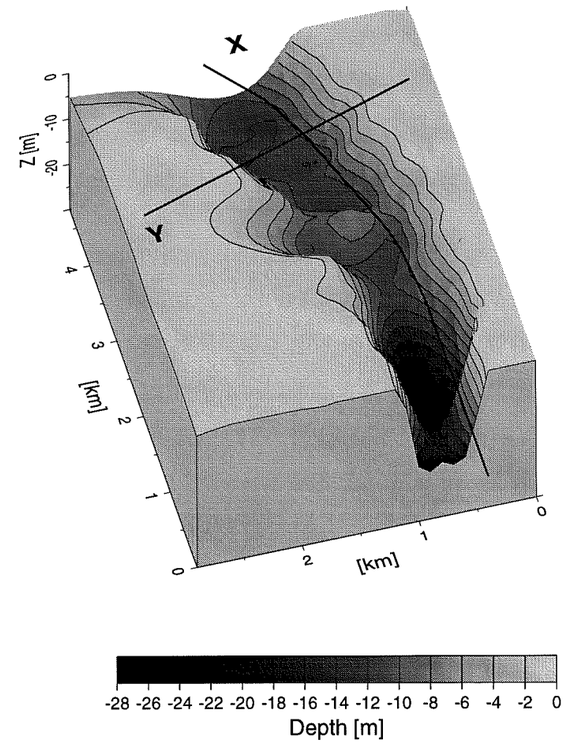


Figure 3.1: 3-D sketch showing the geometry of south channel reach. X is the along-channel, stream following, axis. Y is the across-channel axis, it is locally orthogonal to X and Z.

model is concerned solely with forcing by surface elevation differences. Although this

is a severely simplified approach to model tidal wave propagation in an estuary it can be extremely useful as long as the relevant physics is considered.

Some basic assumptions are usually made in 1-D estuarine models to simplify the calculations. The following assumptions are valid for the type of systems discussed here:

1. The estuary is narrow. The effects of the earth's rotation may be neglected, if the Rossby radius of deformation, $R_f = \frac{\sqrt{gh}}{|f|}$, is greater than the width scale of the estuary, Gill [13]. For the Columbia river, $f = 1.47 \times 10^{-4}\ sin(46°)\ sec^{-1} = 1.057 \times 10^{-4}\ sec^{-1}$, and $R_f = \frac{\sqrt{9.81 \frac{m}{sec} 10m}}{|1.057 \times 10^{-4} sec^{-1}|} = 93.7\ km$. The maximum width of the CRE is approximately 13 km, which is much smaller than $R_f = 93.7\ km$, therefore the effects of rotation can be neglected here.

2. The tidal waves are only weakly non-linear in the estuary. This assumption may be used if two conditions are met: a) The waves are of finite amplitude, $\alpha = \frac{\zeta_0}{h} << 1$. in the CRE $\zeta_0 \sim \mathcal{O}(1\text{m})$ and $h \sim \mathcal{O}(10\text{m})$, therefore $\alpha \sim \mathcal{O}(0.1) << 1$. And, b) the waves are non-dispersive, $\beta = (\frac{h}{\lambda})^2 << 1$. Where $\lambda = C_0 T = \sqrt{gh}T = \sqrt{9.81 \frac{m}{sec}\ 10m} \times 12.42hr\ \frac{3600sec}{1hr}) = 442852m$. Therefore, $\beta = (\frac{10m}{442852m})^2 = 2.26 \times 10^{-5} << 1$ and the tidal waves can be assumed to be non-dispersive in the estuary.

3. The river-flow only enters only at the upstream end of the model, or Q_{river} is independent of along-channel position.

4. The ocean is an infinite basin, the river flow does not effect the surface height of the ocean and,

5. the tides in the river are only driven by the oceanic surface height. This assumption is met for the semidiurnal tide, but there is a significant diurnal fluctuation in riverflow, and therefore elevation, at the fluvial end of the system induced

by the daily power peaking cycle at Bonneville Dam. Therefore, the 1-D model developed here is only valid in the more seaward part of the system where the influence of Bonneville Dam is minimal.

Several different approaches have been used to represent channel width and depth in 1-D barotropic modeling. For example, Prandle and Rahman [43] represent the width and depth as powers of along channel position. Being natural systems, the entire length of most estuaries can not be described in these simple terms. In another approach Jay [27] presents a method to model frictional tidal long wave propagation over strong topography using an exponential representation of the bathymetry in each of several segments. He develops two solutions to the 1-D wave equation. The first solution which he terms the "standard" solution is used where acceleration and friction are weak relative to topography or when friction and topography are weak relative to acceleration. The second solution, which he calls "critical", is used when friction is dominant over topography and acceleration. This formulation accounts for the important physics, topography, friction, river flow, tide flats and finite amplitude waves. Following Green's 1837 development, Jay distorts the along-channel metric by the wave speed such that a hypothetical inviscid tidal wave travels at the same speed regardless of its width or depth. That is the new, distorted along channel metric ($x_{distorted}$ or ,x^*) is the actual along-channel distance divided by the wave speed. Where Green used the inviscid wave speed $C_0 = \sqrt{gh}$, Jay includes the effects of tidal flats on continuity and used $C_m = \sqrt{\frac{g\,b}{h^m b_T}}$, where b_T is the total channel width, b is the momentum carrying channel width and $m = 1$ for "standard" case and $m = 2$ for "critical" convergence. Jay's approach is used in the present work.

A 1-D barotropic may be used to determine properties of tidal wave propagation in an estuary such as friction and wave number. The advantages of this approach are: computational speed, ease of implementation and direct calculation of the wave numbers and amplitudes of the incident and reflected waves, allowing interpretation

of the results. Parker [42], however, reiterates the importance of the non-linear terms in modeling flows in his review of non-linear mechanisms in tidal interactions. In the 1-D equations these terms are : 1) Non-linear continuity, $\frac{\partial \zeta u}{\partial x}$, which only affects the system at overtide frequencies and is therefore not included. 2) Inertia, $u\frac{\partial u}{\partial x}$, the most important form of this term is $u_{river}\frac{\partial u_{tidal}}{\partial x}$ which is included here, and 3) friction, $u|u|$, where x is the along-channel distance and u is the velocity and ζ is surface elevation. It is documented by several authors,e.g. Friedrichs and Aubrey [7], LeBlond [35] and Jay [27], that strongly forced estuaries are dominated by friction during most of the tidal cycle except around slack water. The quadratic friction term, $u|u|$, generates constituents that "may interfere with or alter the incoming tide", Godin and Gutierrez [14]. It is therefore important to model the friction properly to correctly model the flow. Dronkers [3] proposes a formulation of the friction term which is a third-order Chebyshchev polynomial expansion,

$$u|u| = \frac{u}{\pi}(p_1 + p_2u^2 + p_3u^3) \tag{3.1}$$

where $p_{1,2,3}$ are the Chebyshchev polynomials, this expression is more accurate, although more difficult to calculate, than Godin's: [14] formulation

$$u|u| = \frac{1}{2}(0.7u + \frac{u^3}{0.7}) \tag{3.2}$$

where u is interpreted as the sum of the mean flow and the appropriate number of tidal species. Although Dronkers' friction formulation is slightly more accurate, Godin's equation is much easier to calculate and was therefore used in this 1-D model.

To implement this model the river is divided in along-channel sections. The channel depth (h), channel width (b) and total width (b_T) (channel width plus tidal flat width) of each section is allowed to vary independently in an exponential fashion: $b = B_0e^{\alpha x_{distorted}}$, $b_T = B_{T_0}e^{\beta x_{distorted}}$ and $h = H_0e^{\gamma x_{distorted}}$. This allows the width or depth to be calculated at any point in a section. As stated earlier, tidal flats are included in this model. Their inclusion is important because they are momentum

sinks both on flood and ebb; as the water moving up-river on flood flows onto the tidal flats and comes to rest losing its momentum to bottom friction. Then, on ebb the water on the tidal flats, which has zero momentum, is re-accelerated as it enters the channel. The effects of channel curvature are not included here because they have no effect on a sectionally averaged basis.

The dimensional form of the wave equation, Jay (Equation 5) [27], is:

$$\underbrace{\frac{\partial^2 Q}{\partial x^2}}_{Pressure} - \underbrace{\frac{1}{b_T}\frac{db_T}{dx}\frac{\partial Q}{\partial x}}_{Press\,\&\,Topo} - \underbrace{\frac{3b_T - b}{g\bar{A}}U_R\frac{\partial^2 Q}{\partial x \partial t}}_{Conv\ Accel} + \underbrace{\frac{2b_T}{g\bar{A}^2}U_R\frac{d\bar{A}}{dx}\frac{\partial Q}{\partial t}}_{Conv\ Accel} - \underbrace{\frac{b_T}{g\bar{A}}\frac{\partial^2 Q}{\partial t^2}}_{Acceleration} - \underbrace{\frac{b_T}{gh}\frac{\partial T_b}{\partial t}}_{Bed\ Stress} = 0 \tag{3.3}$$

where Q is transport, x is along channel distance, b is the channel width, b_T is the total width including tidal flats, $\overline{A}$ is the channel cross-sectional area, t is time, g is the acceleration due to gravity, U_R is the river velocity, h is the channel depth and T_b is the bed stress. The boundary conditions for the system are: 1) the surface height (ζ) is specified at the mouth and 2) the transport (Q) and surface height go to zero as $x_{distorted} \to \infty$. The boundary conditions between adjacent sections in the model are as follows: The transport through upstream section boundaries is required to be identical to the transport through all connected down-stream section boundaries. Also, the surface height across section boundaries is required to be continuous: $\zeta_1|_{x_0} = \zeta_2|_{x_0} = \zeta_2|_{x_0}$ and $Q_1 = Q_2 + Q_3$, see Figure (3.2).

3.2 One-Dimensional Barotropic Modeling Approach

A bathymetric model of the Columbia River was generated extending from the mouth to approximately Rkm 150. This bathymetric model was then divided into sections, shown in Appendix C, each allowing the depth, width and total width to vary with the along-channel distance. This technique produces a more realistic bathymetric model than treating the channel as single continuous section. The primary detail

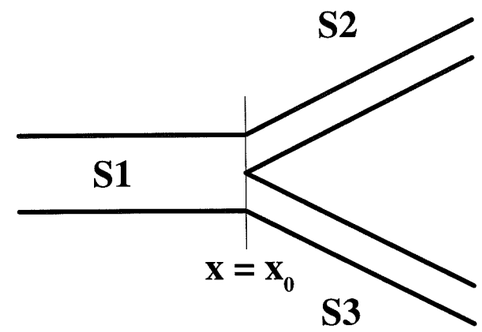


Figure 3.2: Schematic showing the bifurcation of one channel into two. The flow rate through channel S1 equals the sum of that through S2 and S3. At the juncture, $x = x_0$, the surface height are equal, $\zeta_{S1} = \zeta_{S2} = \zeta_{S3}$.

of the Columbia River topography used here was concentrated in the estuary up to Rkm 60. The more landward portion of the model is included to allow the landward decay of the tidal waves. Detailed representation of the tides here were not attempted because there is no salinity in this part of the system. The oceanic tidal forcing for the K_1 and M_2 bands was specified at the mouth, and the riverflow is specified at the upstream end of the model. It was assumed that, where the channel is divided, 30% of the river flow is in the south channel, 40% in the north channel and the remaining 30% flows between the two channels. In the first plot of Figure [3.3], the tidal flats are shown in black. These tidal flats are dry at low water and completely inundated at high water. The momentum conveying channel is shown in gray and the white polygon in the middle illustrates where the north and south channel are separated — not tidal flats. The second plot shows the corresponding laterally averaged channel depths. Where the north and south channel separate, the north channel depth is

shown as the solid line an the south channel as dashed. The output of the barotropic

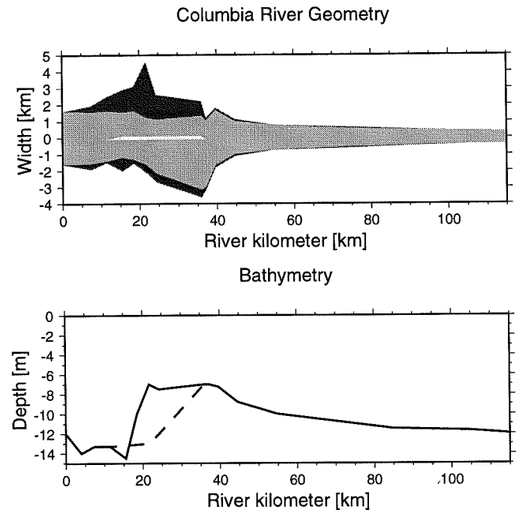
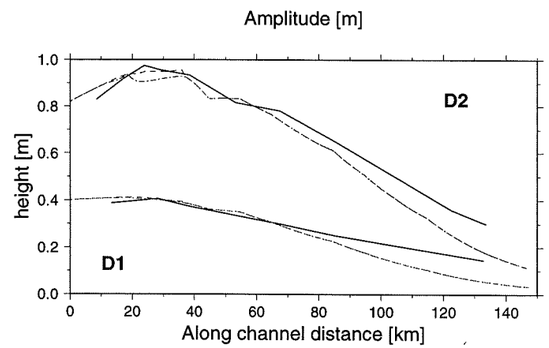


Figure 3.3: Actual widths and depths used as input to the 1-D model. The first panel shows the channel widths; the tide flats for each channel are shown in black, the channels are gray and the channel separation is shown in white. The second panel shows the north channel bathymetry as the solid line and the south channel as dashed.

was compared to the measured tidal height and phase data collected in 1980-1981. Figure (3.4) is the comparison of tidal height amplitude and phase at both the diurnal (D_1) and semidiurnal (D_2) frequencies. The solid line is the data, the dashed line is the model results for the north channel, where the data was collected and the dashed-dot line is for the south channel. The agreement is very reasonable at both frequencies for height and phase, especially in the mid estuary (Rkm 15 - 40). Above Rkm 80 the diurnal frequency data is contaminated by the daily power peaking cycle at Bonneville dam.



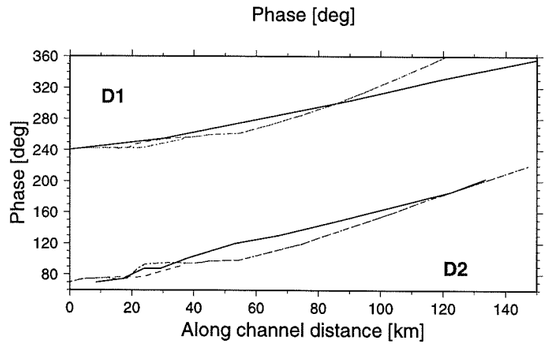


Figure 3.4: Comparison of data and model D_1 and D_2 height amplitude and phase. (-) data north channel , (–) model north channel and (-.) model south channel.

Chapter 4

PROFILE MODELING: DEVELOPMENT AND VERIFICATION

This chapter presents the theory of estuarine dynamics and then develops a new type of profile model for systems strongly forced by both oceanic tides and riverflow. This model, driven by the 1-dimensional (1-D) barotropic tidal model presented in Chapter 3, is then validated using density and velocity data collected in the Columbia River estuary (presented in Chapter 2) and by comparison to analytic solutions. To obtain a better understanding of the effects of lateral variations in depth, the presents of tidal flats, channel curvature and stratification on the different flow modes, Chapter 5 presents several simulations.

Estuarine dynamics theory discussed here includes generation of residual, tidal and overtide internal circulation, mixing mechanisms, and interactions with topography, tidal-flow, riverflow and the density field. Residual internal circulation includes responses to river discharge, winds, the density field and zero frequency and tidal non-linearities. Overtides, harmonics of basic tidal frequencies, are also generated through non-linear interactions of the basic tides.

In narrow, shallow systems vertical turbulent mixing, and thus the residual circulation, can be driven by different dominant processes. It is therefore useful to classify estuaries by the degree to which they are stratified. Several authors have put forward classification schemes for estuaries, e.g. Hansen and Rattray [17] and Jay and Smith [32] & [33]. Hansen and Rattray [17] propose the following classifications based on two parameters: highly stratified, weakly stratified and partially mixed. Jay and Smith

[32] & [33] investigate the dynamics in each of these systems. In highly stratified systems the residual circulation is primarily caused by ebb-flood asymmetry in the density interface position and thickness, while in weakly stratified systems it is finite amplitude barotropic effects and in partially mixed systems it is steady horizontal density gradient forcing and barotropic effects, Jay and Smith [32] & [33]. Many systems fall under different regimes during different times of the tidal monthly cycle or for different runoff conditions, so for a model to be useful it needs to contain the necessary physics explain all of these flow scenarios.

Several studies (Hansen and Rattray [16] and Jay and Smith [32]) acknowledge that river discharge, wind stress and density driven circulation are all important in determining the salinity distribution in an estuary — that it is important to understand the interaction between the density and total velocity field (driven by all circulation modes) of an estuary. Some previous analyses of the problem were based on boundary layer approximations but Ianniello [19] shows these analyses to be invalid for realistic channel depths and eddy viscosity magnitudes. The basis for most residual estuarine circulation modeling is Hansen and Rattray's two layer circulation model [16]. They calculated the gravitational flow in narrow estuaries of constant (rectangular) cross-section, but depth variations in the channel also effect the circulation of an estuary. Wong [54] solved the same equations as Hansen and Rattray but for a V-shaped channel and showed that upstream bottom flow occurs in the deepest part of the channel while downstream flow persists in the shallows. Ianniello's [20] results show significant differences in the residual circulation patterns between channels of constant breadth and depth and those of varying cross section. Tidal oscillations may be greatly effected by strongly convergent topography, to the point that the flow is "significantly different from classical views of tidal oscillations in rectangular, straight channels", Friedrichs and Aubrey [7]. Most estuaries can be described as short relative to the tidal wavelength with topographic features which are short relative to the length of the estuary, reiterating the necessity to include accurate topography in any model.

These studies demonstrate the necessity of considering the 3-dimensional (3-D) problem and not just in 1 or 2 dimensions. The necessity of using a 3-D model is also demonstrated by observations in the CRE. Jay [26] and Jay and Musiak [30], show that strong internal residual and overtide flows with complex spatial distributions are generated by time varying stratification. Thus, internal ebb-flood asymmetry in the vertical distribution of the horizontal tidal velocity can cause the velocity field, generated by a single surface elevation harmonic species, to have a mean flow and a complex overtide field beside the basic tidal motion.

4.1 Current Modeling Effort

To complete a comprehensive model of estuaries which are strongly forced by both tides and riverflow, I have combined the above ideas into a profile model that incorporates residual, tidal and overtide flow. Figure (1.1) in Chapter 1 is a block digram showing driving forces and resulting currents for each of the modes discussed here. A profile model calculates velocity profiles at specified points in the estuary, usually chosen to observe interesting phenomena. This approach saves time relative to a 3-D numerical models which calculate variables at more regular intervals. This final model is quasi 3-D, harmonic, semi-analytical, mode-splitting (between the 1-D barotropic and profile models), expressed in distorted $\sigma-$coordinates and treats non-linearities via a simple perturbation expansion. It includes the ability to model 3-D flow in estuaries with tidal flats and multiple channels of arbitrary, but narrow, cross-section which are forced by multiple tidal species, riverflow, wind and a 3-D density field. This scheme is used instead of a full 3-D finite difference or finite-element model because the present approach requires less computing resources, yields acceptably accurate results and provides better qualitative understanding. The profile model used here incorporates the following: 1) a stream-following coordinate system, 2) calculation of surface slope using all profiles of a cross section, 3) lateral depth dependency in

mean density forcing, 4) surface wind stress, 5) lateral and along-channel variability of stratification, 6) lateral and time variability of Ri_{gT}, 7) the ability to have multiple, intersecting channels, and 8) the ability to incorporate multiple tidal species. Model forcing and calculation procedures may be easily modified as a result of a modular programming approach.

Since the flow in many estuaries is frictionally dominated flow over strong topography it is thus necessary to accurately represent friction, depth, density field and topography if the model is going to model the system correctly. The problem is complicated because, for any system the dominate mixing process may change during the tidal month or for changing river flow. Also, the flow field of an estuary may be significantly effected by the residual and overtide flows generated by non-linear interactions. But a good model of a weakly non-linear system may be obtained by combining a 1-D barotropic model with a profile model. For systems where such an approach is appropriate, results of this scheme approach the accuracy of full 3-D finite-element models and are obtained more quickly.

4.2 Definition of Flow Modes

The quasi-linear perturbation modeling approach used here assumes that the flow in a narrow estuary may be approximated as a linear sum of several parts or modes. These individual modes can be treated separately. By this scheme, the total flow may be divided into an $\mathcal{O}(1)$ tidal component, $\mathcal{O}(\varepsilon)$ residual flows, an $\mathcal{O}(\varepsilon)$ overtide component and various $\mathcal{O}(\varepsilon^2)$ components. Separate $\mathcal{O}(1)$ tidal modes may include flow at diurnal and semidiurnal frequencies. The $\mathcal{O}(\varepsilon)$ residual flow may consist of numerous separate modes which are listed below. And, the overtide flow is driven by semidiurnal terms. The number of residual flow modes in stratified, narrow estuaries is substantial even if only two-dimensional, 2-D, forcing (in the along-channel and vertical directions) is considered. They include:

"tidal non-linear residual" driven by low-frequency correlations of $\overline{(u_1 \frac{du_1}{dx} + w_1 \frac{du_1}{dz})}$, where u is along-channel velocity, w is the vertical velocity and a subscript "1" indicates a tidal frequency variable. This name is not ideal but is commonly used as it is motivated by the fact that this mode is present even in the absence of a spatially variable density field. This mode is not considered here as it is important primarily in weakly stratified systems.

gravitational circulation forced by the mean horizontal density gradient,

internal tidal asymmetry driven by correlations of time-varying vertical mixing and vertical shear (K_1 and $\frac{du_1}{dz}$),

river outflow forced by mass entering at the upstream end,

wind driven circulation the wind blowing along the surface of the estuary generates a surface flow in the direction of the wind and a return flow develops lower in the water column, and

Stokes drift compensation flow an outward Eulerian flow that compensates for the landward Stokes drift.

These six modes belong to two broad classes — internal and discharge:

- Internal modes — characterized by having little or no surface expression and a 180° phase change in the vertical, or in other words, velocity sectionally integrates to zero. They are usually two-layered but may be multi-layered. This class includes gravitational circulation, internal tidal asymmetry, wind driven flow and the tidal non-linear residual.

- Discharge modes — have a specified non-zero integral discharge whose magnitude normally increases monotonically from the bed to the surface. This class includes riverflow and the Stokes drift compensation flow.

Stokes drift compensation flow and tidal non-linear residual modes will not be discussed here. The riverflow, wind and gravitational modes are linear in the sense that they depend on the tidal flow only to the extent that turbulence levels, and therefore K_m, are set primarily by the tidal flow and its advection of the mean density field. In contrast, tidal non-linear residual and the Stokes drift (whose roles in estuarine circulation were investigated by Ianniello [18], and internal tidal asymmetry (Jay [26]; Jay and Musiak [29]) are all forced directly by the tidal flow. There are quadratic non-linearities that also drive overtide flows. Additional modes of along- and across-channel residual flow arise when genuinely 3-D forcing is considered in the cases of channel curvature and laterally variable density forcing; these modes are not considered here.

The purposes of this section is to:

- develop a modeling formalism for systematic investigation of 3-D residual flows in channelized estuaries (with arbitrary, but slowly varying, channel cross-section) as driven by 2-D surface and internal density forcing;
- determine how the various residual flow models are distributed in a typical estuarine cross-section;
- determine how the influence of cross-section shape, stratification and variations in forcing parameters affect the modes considered; and
- understand how the different depth dependences of the various residual flow modes contributes to 3-D variability of the velocity field in a stratified estuary.

This analysis uses a frictional velocity (u_*), consistent with the tidal flow model of Chapter 3 to determine a K_m profile. The stratification correction to the K_m profile is discussed below.

4.3 Relationship to Previous Studies

Analyses of residual flow have played a prominent role in the history of estuarine physical oceanography. Interest in this topic has been spurred by the importance of residual flow in maintaining the estuarine salt balance and in scalar and pollutant transport, the complexities of the non-linearities involved, the number of distinct flow modes and the utility of estuarine residual flow processes as a means of estuarine classification. Early studies by Pritchard [45], [46] & [47] provide a background of quantitative observations and a key idea — that the along-channel density forcing is nearly spatially uniform. This spatial uniformity was used by Hansen and Rattray [16] to develop a similarity solution for the "central regime", where this uniformity of density forcing prevailed. Other solutions valid near the entrance and upstream limits of salinity intrusion were also developed. This theoretical approach treated the tides solely as a source of vertical mixing while their role in the advection of salt was only treated parametrically. Here, the tides do not directly generate residual flow. Reviews, critiques and variations of this approach include Dyer [4], Officer [41], Fischer [6], Hughes and Rattray [15], Oey [40] and Kjerfve [34].

Another line of thinking built on barotropic tidal analysis and recognized the role of tidal convective accelerations, the Stokes drift and surface elevation fluctuations in driving residual flows, Nihoul and Ronday [39] and Uncles and Jordan [53]. These and other similar analyses all employed vertically integrated equations. Ianniello [18] & [19] calculated analytically profiles of tidally driven residual flow, pointed out the importance of two-layered, tidal-residual flow and showed that scalars at different depths of the flow might have Lagrangian transports in opposite directions directions, just as with gravitational circulation. He also set up the analogous overtide problem which was not, however, susceptible to analytical solution, and analyzed the effects of multiple tidal constituents in generating fortnightly variations in residual flow. Almost all studies employed a 2-D laterally or vertically integrated approach, despite

Fischer's [5] demonstration of that landward gravitational circulation was concentrated in deeper parts of channels effectively rendering the residual flow problem 3-D. Virtually the only exception was Ianniello [20] & [21], who investigated the effects of lateral variability of channel width and depth on tidally induced residual flow in 3-D.

The isolation of these two lines of thought is striking. One ignored the presence of tides as a generator of residual flows, while the other neglected density forcing. None of the above analyses attempted to take stratification effects on vertical mixing into account despite the well-known control of boundary-layer vertical turbulent mixing by stratification. In an attempt to unify these two lines of thought, Jay and Smith [31], [32] & [33] showed how gravitational circulation, riverflow, Stokes drift compensation flow and barotropic residual could all be included in a single analytical perturbation approach. Stratification effects were accounted for by modifying a vertically uniform K_m by a stratification correction appropriate to a level 10-20% of flow depth from the bed, and by introducing a slip velocity at the bed. Jay [26] further showed that different patterns of stratification on flood and ebb (which lead to tidal correlations of tidal variations in K_m and tidal shear) should generate from the basic M_2 tide not only residual but internal overtide flows in the approximate ratios of 0.63:0.42:0.08 for the mean (Z_0, M_4 and M_8 flows, respectively.

Jay and Musiak [30] & [29] used moored current meter records, acoustic Doppler current profiler (ADCP) and conductivity-temperature-depth (CTD) data to demonstrate the existence of this "internal tidal asymmetry" and indicate its importance in suspended sediment transport. The decisive feature was anomalously large internal residuals and overtides during periods of high stratification. They were seen not only at M_4 but also, because of the prominence of the diurnal tide in the Columbia River estuary, at M_3. A preliminary, laterally averaged semi-analytical model was also provided, and a literature review was employed to argue that internal tidal asymmetry was an important feature in most if not all narrow estuaries with strong tides and riverflow, being present in at least 20 such systems.

Finally, Wong [54] provided an analytical treatment of gravitational circulation in a triangular estuarine cross-section. He pointed out the important distinction between models that conserve flow in each vertical column and those that conserve mass over an entire cross-section. His results agree with numerous observations dating back to Fischer [5] that indicate the presence of net outflow along channel margins with net inflow in mid-channel.

Residual flow and mean density parameters have also been used implicitly or explicitly in estuarine classification systems. These include methods such as Pritchard and Kent [48] that also employ geomorphic properties, and the two-parameter system of Hansen and Rattray [16] as subsequently modified or generalized by Rattray and Uncles [49] and Prandle and Rahman [43]. The essential external parameters in the classification problem for shallow channelized systems include at a minimum: riverflow (q_R) usually non-dimensionalized as a Froude number, the ratio of the fresh/salt water density difference to density ($\frac{\Delta\rho}{\rho}$) and tidal amplitude surface height (ζ), non-dimensionalized by mean depth (H) as $\varepsilon = \frac{\zeta}{H}$. Speer and Aubrey [52] have suggested a modification of the last parameter to take into account the presence of tidal flats resulting in temporal variations in width as well as depth. This suite of parameters, when combined with suitable geomorphic properties, ought to be sufficient to describe the salinity intrusion into a narrow channel, but no system advanced to date is entirely satisfactory. Additional parameters are clearly needed if fjords or broad estuaries are to be considered, and to take into account such properties as atmospheric forcing.

The separation of ideas about narrow estuaries from another line of investigation by Zimmerman [55] & [56] is somewhat more understandable. Zimmerman used a vertically integrated (VI) analysis to show that random topography on the scale of about one tidal excursion in a broad, shallow estuary could result in large and chaotic (in the formal, mathematical sense) Lagrangian particle displacements. When this type of tidal dispersion is parameterized in terms of a horizontal gradient and mean horizontal diffusivity, the resulting diffusivity is about an order of magnitude larger

than that expected for shear dispersion, as seen in river estuaries. Thus, the regime studied by Zimmerman is physically quite different from the narrow channels with tidal flats considered here.

4.4 *Profile Model Formulation*

4.4.1 Strategy

Two of the residual flow modes under consideration here, gravitational (baroclinic) circulation in the central regime and river outflow, have relatively simple along-channel structures dictated by variations in channel cross-section. The along-channel variation in the speed of the river outflow is prescribed by the channel geometry because the integral riverflow (q_R) is assumed to be constant in time and enters only at the up-stream boundary. In addition to the sensitivity to variations in cross-sectional area, the gravitational circulation case is strongly effected by the lateral and vertical variations in the assumed density field. For simplicity, the mean along-channel density gradient ($\frac{d\bar{\rho}}{dx}$) is assumed here to be linear, following the ideas of Hansen and Rattray's central regime theory. Previous attempts to calculate an along-channel surface slope ($\frac{\partial\bar{\rho}}{\partial x}$), which is responsive to a specified channel geometry, have either deviated little from linearity or not been more accurate. If a more accurate form of the mean along-channel density gradient is determined at a later date, it could be readily employed in the model presented here. Separation of the horizontal and vertical parts of the problem is maintained, but there is no need to form a sectionally integrated (SI) wave equation (as in the tidal problem), as such an equation would be degenerate for zero-frequency motion. If tidal monthly fluctuations and riverflow transients were to be considered it would be possible to form a wave equation, but still unnecessary because, at these subtidal frequencies, the acceleration term is much smaller than the pressure-gradient and bedstress terms which dominate the subtidal force balance in shallow estuaries. This can be shown by considering the scaling employed in the tidal

frequency SI wave equation, Jay [22]: In the momentum equation the bedstress term is non-dimensionalized by a ratio of bedstress to acceleration ($\frac{R}{\omega}$). For semidiurnal tides in river estuaries considered here, typically 10-20 m deep, this ratio is $\mathcal{O}(1)$. While, in the very shallow, highly non-linear regime analyzed by Friedrichs and Madsen [8] and Friedrichs and Aubrey [7], $\frac{R}{\omega} < 1$. And, for subtidal oscillations with periods of ~5-30 days, which are typical time scales for fluctuations in riverflow and gravitational forcing caused either by changes in riverflow or tidal-monthly changes in salinity intrusion length, $\frac{R}{\omega} \gg 1$.

Because a wave equation is not used for the residual flow problem, continuity (mass conservation) and along-channel momentum conservation are implemented separately; this has an important impact on solution methodology. As a group, the profile solutions for any given cross-section must meet the integral requirement set by continuity; this requirement determines a laterally uniform surface slope sufficient to satisfy the discharge requirement for that mode. A laterally non-uniform along-channel surface slope, any mode, would imply that a cross-channel slope existed as well. But, because all of the estuaries considered here are narrow with scale widths (B) typically less than 10 km and scale depths (H) of $\mathcal{O}(10\,\mathrm{m})$ the lateral long-wave adjustment time to eliminate the cross-channel slope, $\frac{B}{(gH)^{\frac{1}{2}}}$, is always less than 0.3 hr which is small relative to a tidal cycle and extremely small relative to the low-frequency motions considered here. Clearly, a laterally uniform horizontal pressure gradient is appropriate for all the residual flow modes considered, so long as the dynamic pressure resulting from these motions can be neglected; scaling will show that this is the case.

The same (x^*, y, σ, t)-coordinate system is employed here as in Jay [22]. Here, σ is simply the distorted vertical coordinate: $\sigma = \frac{z}{h}$, where z is the height off of the bed and h is the local bottom depth. In this σ-coordinate system the water surface is always $\sigma = 1$ and the bottom is at $\sigma = 0$. Use of σ-coordinates is justified by its utility in dealing with topographic variations. The along-channel coordinate (x) is distorted in such a way that a hypothetical inviscid wave travels at a constant rate

regardless of changes in channel width or depth and is given in its dimensional (1-a) and non-dimensional (1-b) forms by:

$$x = x^* \left(\frac{b_t}{gb\{h\}^n}\right)^{-\frac{1}{2}} \quad n = 1, 2 \tag{1-a}$$

$$X = X^* \left(\frac{B_t}{B\{H\}^n}\right)^{-\frac{1}{2}} \quad n = 1, 2. \tag{1-b}$$

Where: x^* is the new distorted along channel distance and { } indicates a width average, lower case variables are dimensional and the corresponding capitals are non-dimensional, b represents the momentum-conveying channel width, h the depth, $b_t = b + \Delta b$ is the mean total width (where Δb is half the high-water tidal flat width), $n = 1$ for strong or weak topographic convergence/divergence and $n = 2$ for shallow systems with very strong friction and those near "critical convergence" as described in Jay [26] and [22]. This x-distortion is not actually necessary for the present analysis but is employed for consistency, so that the results for the linear residual modes may be more readily compared to those for non-linear modes, where the distorted x^*-coordinate is essential. Derivatives in this distorted coordinate system are given by:

$$\frac{df}{dx^*} = \frac{df}{dx}\,\frac{dx}{dx^*} \tag{2}$$

for arbitrary f and where:

$$\frac{dx}{dx^*} = \left(\frac{b_T}{gbh^n}\right)^{\frac{1}{2}} + \frac{x}{2}\frac{d}{dx^*}\left(\frac{b_T}{gbh^n}\right)\left(\frac{b_T}{gbh^n}\right)^{-\frac{1}{2}} \tag{3}$$

and $n = 1, 2$ for standard and frictionally dominated solutions respectively. Derivation of solutions to the residual flow problem requires definition of bed topography. The following representation, derived from the (SI) tidal problem Jay [22], has been employed:

$$\begin{aligned} b(x^*) &= \mathbf{B}B(X^*) = \mathbf{B}e^{\alpha X^*} \\ b_t(x^*) &= \mathbf{B}_t B_t(X^*) = \mathbf{B}_t e^{\beta X^*} \\ h(x^*) &= \mathbf{H}\, f(Y)\, H(X^*) = \mathbf{H}\, f(Y)\, e^{\gamma X^*} \end{aligned} \tag{4}$$

where $\mathbf{B}$, $\mathbf{B}_t$ and $\mathbf{H}$ are scale channel-width total-width and depth, respectively and $f(Y)$ allows for variation of depth across-channel. The lateral, or y, variations within a channel section may be set as desired.

4.4.2 Mass Conservation

Conservation of mass at zero frequency is implemented through a mean, sectionally integrated continuity equation. As with the tidal-frequency version of continuity, this is quite a powerful constraint in narrow, channelized estuaries. The lowest-order dimensional version of this is, converted to the (x^*, y, σ, t)-coordinate system Ianniello [19], Jay [25]:

$$\frac{dx^*}{dx}\frac{\partial}{\partial x^*}(hb\int_{\sigma_0}^{1}\overline{u}\,d\sigma) + \frac{dx^*}{dx}\frac{\partial Q_s}{\partial x} = 0 + \mathcal{O}(\varepsilon^2). \tag{5}$$

A first approximation to the integral Stokes drift developed by Longuet-Higgins [36], $Q_S \cong bu|_{\overline{\zeta}}\overline{\zeta}$, has been employed in Equation (5). The form of this term results from: a) splitting the vertical transport integral into two parts, i) from the bed to the mean free surface, $\overline{\zeta}$, and ii) from $\overline{\zeta}$ to the instantaneous free surface, ζ ; b) approximation of the second term via a Taylor series; and c) time-averaging of the resulting equation. If there is no wind stress (and the free surface remains unstressed) then the term $\frac{d\overline{\zeta}}{dt}$ can be neglected in Equation (5) because it is $\mathcal{O}(\varepsilon^2)$, and the next non-zero term in the above Taylor series is $\mathcal{O}(\varepsilon^3)$. Continuity in the form of Equation (5) states that the mean Lagrangian flow (sum of mean Eulerian and Stokes drift terms) is conserved as the flow moves in the along-channel direction. The momentum conveying width (b) rather than the mean total width (b_t) appears in Equation (5) and throughout the analysis that follows as a consequence of the small amplitude approximation; the mean flow is conveyed, for present purposes, entirely within the momentum conveying part of a channel.

Division of Equation (5) by $\frac{dx^*}{dx}$ and a first along-channel integration from arbitrary x to ∞, which is taken to be some point landward of tidal penetration (where the

tidal flow vanishes), is used to formulate boundary conditions for the residual flow:

$$\int_{\infty}^{x} \frac{\partial}{\partial x}\overline{Q}\, dx = -(Q_S|_x - Q_S|_\infty) = -Q_S|_x \quad \text{(6-a)}$$

$$\overline{Q} = -\overline{Q}_S + Q_R. \quad \text{(6-b)}$$

This conservation law states that the along-channel Eulerian flow is the sum of a Stokes drift compensation flow and a riverflow. Because the incident landward wave is always larger and has a larger Stokes drift in the presence of friction than the reflected wave (except at a point of perfect reflection), the Stokes drift is landward. Thus, both the terms on the right, $-Q_S$ and Q_R, and their sum (the total outflow) are negative for the positive estuaries considered here. An important consequence of mass conservation is that the only estuarine circulation modes with non-zero cross-sectional integrals are those that correspond to specific terms on the right-hand side of Equation (6-b); i.e., riverflow and the Stokes drift compensation flow. For example, the riverflow ($\overline{u}_R$) must satisfy:

$$\int_{-\frac{b}{2}}^{+\frac{b}{2}} h \int_{\sigma_0}^{1} \overline{u}_R\, d\sigma\, dy = Q_R. \quad \text{(7-a)}$$

Physically, the riverflow and Stokes drift compensation flows are forced by the surface slope necessary for their discharge. In the solution procedure for these modes, the sectionally uniform surface slope is set, by a shooting method, such that the relevant discharge requirement is met. The remainder of the residual flow modes are internal and integrate to zero over the cross-section; e.g. for the gravitational circulation, $\overline{u}_G$:

$$\int_{-\frac{b}{2}}^{+\frac{b}{2}} h \int_{\sigma_0}^{1} \overline{u}_G\, d\sigma\, dy = 0 \quad \text{(7-b)}$$

and for the wind driven circulation, $\overline{u}_W$:

$$\int_{-\frac{b}{2}}^{+\frac{b}{2}} h \int_{\sigma_0}^{1} \overline{u}_W\, d\sigma\, dy = 0. \quad \text{(7-c)}$$

The internal modes are forced by specific terms in the along-channel momentum equation or from boundary conditions described in the following paragraphs. As with

the non-zero modes, the surface slope is set so that the discharge requirement is met. Note also that the riverflow and Stokes drift compensation flow modes are formally identical, except for the physical source of the flow that must be discharged. If the vertically averaged value of u, $<u>$, is used to approximate $u|_{\overline{\zeta}}$ in the definition of Q_S, then the Stokes drift compensation flow profile may be determined, just as the gravitational circulation and riverflow profiles are, without specific knowledge of the tidal velocity profile. This may be a reasonable approximation to use in weakly and partially stratified estuaries, but rarely in a highly stratified one. The more complex highly stratified case is not considered here. Calculation of the residual σ-coordinate vertical velocity $\overline{w}$ requires mass conservation at a point:

$$\frac{\partial \overline{u}}{\partial x^*}\frac{\partial x^*}{\partial x} + \frac{\partial \overline{w}}{\partial \sigma} = 0 \tag{8-a}$$

and the definition of $\overline{w}$ in terms of the Eulerian vertical velocity, $\overline{W} = \frac{\partial \zeta}{\partial t}$:

$$\overline{w} = \frac{\overline{W}}{h} - \overline{U}\frac{\sigma}{h}\frac{dh}{dx^*}\frac{dx^*}{dx}. \tag{8-b}$$

Because the mean flow is carried entirely within the momentum-conveying width (b) modification of Equations (8-a) and (8-b) to include the effects of tidal flats (as in Jay [22]) is not necessary.

4.4.3 Scaling Analysis of Along-Channel Momentum Equation

This section presents the derivation of the momentum equation used in the profile model.

Reynolds equation

The convention used here is: u is the velocity in the along-channel (x) direction, v is the velocity in the across-channel, (y) direction and w is the vertical (z) velocity. The velocity vector is thus given by:

$$\vec{u} = u\hat{i} + v\hat{j} + w\hat{k}. \tag{9}$$

Starting with continuity and Navier-Stokes equations:

$$\frac{\partial u}{\partial x} + \frac{\partial v}{\partial y} + \frac{\partial w}{\partial z} = 0 \tag{10-a}$$

$$\nabla \vec{u} = 0 \tag{10-b}$$

$$\rho\Big(\frac{\partial u}{\partial t} + u\frac{\partial u}{\partial x} + v\frac{\partial u}{\partial y} + w\frac{\partial u}{\partial z}\Big) = -\rho g - \frac{\partial P}{\partial x} + \mu\Big(\frac{\partial^2 u}{\partial x^2} + \frac{\partial^2 u}{\partial y^2} + \frac{\partial^2 u}{\partial z^2}\Big) \tag{11-a}$$

$$\rho\,\frac{D\vec{u}}{Dt} = -\rho g - \frac{\partial P}{\partial x} + \mu\nabla^2 u \tag{11-b}$$

the Boussinesq approximation is applied, $\rho = \rho_0 + \rho'$ and let $\rho = \rho_0$ except where it is multiplied by gravity. Equations (11-a) & (11-b) then become:

$$\rho_0\,\frac{D\vec{u}}{Dt} = -g\rho - \frac{\partial P}{\partial x} + \mu\nabla^2 u \tag{12-a}$$

$$\frac{D\vec{u}}{Dt} = -g\frac{\rho}{\rho_0} - \frac{1}{\rho_0}\frac{\partial P}{\partial x} + \nu\nabla^2 u \tag{12-b}$$

Where, μ is the kinematic viscosity and ν is the dynamic viscosity and $\mu = \rho\,\nu$. Now, multiply continuity (10-a) by u and add the product to the Navier-Stokes equation (11-a):

$$\frac{\partial u}{\partial t} + u\frac{\partial u}{\partial x} + u\frac{\partial u}{\partial x} + u\frac{\partial v}{\partial y} + v\frac{\partial u}{\partial y} + u\frac{\partial w}{\partial z} + w\frac{\partial u}{\partial z} = -g\,\frac{\rho}{\rho_0} - \frac{1}{\rho_0}\,\frac{\partial P}{\partial x} + \nu\nabla^2 u \tag{13-a}$$

which simplifies to:

$$\frac{\partial u}{\partial t} + \frac{\partial(u^2)}{\partial x} + \frac{\partial(uv)}{\partial y} + \frac{\partial(uw)}{\partial z} = -g\,\frac{\rho}{\rho_0} - \frac{1}{\rho_0}\,\frac{\partial P}{\partial x} + \nu\nabla^2 u. \tag{13-b}$$

Now assume that each velocity component consists of a time averaged part including tidal and lower frequencies and a varying part consisting of frequencies above the tidal frequency. The time average of the velocity is:

$$\overline{\vec{u}} = \frac{1}{T}\int_{t_0}^{t_0+T} \vec{u}\,dt \tag{14}$$

and the individual velocity components may then be written as:

$$u = \overline{u} + u' \tag{15-a}$$

$$v = \overline{v} + v' \tag{15-b}$$

$$w = \overline{w} + w'. \tag{15-c}$$

Since we are interested in terms of tidal frequency or less, when we take the time average of Equation (13-b) and the first term on the left hand side becomes:

$$\overline{\frac{\partial u}{\partial t}} = \overline{\frac{\partial}{\partial t}(\overline{u} + u')} = \overline{\frac{\partial \overline{u}}{\partial t}} + \overline{\frac{\partial u'}{\partial t}} = \frac{\partial \overline{u}}{\partial t} \tag{16-a}$$

and, the next three terms on the left hand side may be simplified as:

$$\overline{u^2} = \overline{\overline{u}^2} + 2\overline{\overline{u}u'} + \overline{u'^2} = \overline{u}^2 + \overline{u'^2} \tag{16-b}$$

$$\overline{uv} = \overline{\overline{u}\,\overline{v}} + \overline{\overline{u}v'} + \overline{u'\overline{v}} + \overline{u'v'} = \overline{u}\,\overline{v} + \overline{u'v'} \tag{16-c}$$

$$\overline{uw} = \overline{u}\,\overline{w} + \overline{u'w'}. \tag{16-d}$$

Applying relations (16-a, 16-b, 16-c & 16-d) to Equation (13-b) yields:

$$\begin{aligned} \frac{\partial \overline{u}}{\partial t} + \; & \overline{u}\frac{\partial \overline{u}}{\partial x} + \overline{u}\frac{\partial \overline{v}}{\partial y} + \overline{u}\frac{\partial \overline{w}}{\partial z} + \\ & \overline{u}\frac{\partial \overline{u}}{\partial x} + \overline{v}\frac{\partial \overline{u}}{\partial y} + \overline{w}\frac{\partial \overline{u}}{\partial z} + \\ & \frac{\partial \overline{u'u'}}{\partial x} + \frac{\partial \overline{u'v'}}{\partial y} + \frac{\partial \overline{u'w'}}{\partial z} \\ = \; & -g\,\frac{\rho}{\rho_0} - \frac{1}{\rho_0}\,\frac{\partial P}{\partial x} + \nu\nabla^2 u \end{aligned} \tag{17-a}$$

which can be expressed as:

$$\frac{\partial \overline{u}}{\partial t} + \overline{u}\nabla\cdot\overline{\vec{u}} + \overline{\vec{u}}\cdot\nabla\overline{u} + \nabla\cdot\overline{u'\vec{u}'} = -g\,\frac{\rho}{\rho_0} - \frac{1}{\rho_0}\,\frac{\partial P}{\partial x} + \nu\nabla^2 u. \tag{17-b}$$

But,

$$\overline{\nabla\cdot\vec{u}} = \frac{\partial \overline{u}}{\partial x} + \frac{\partial \overline{v}}{\partial y} + \frac{\partial \overline{w}}{\partial z} = \nabla\cdot\overline{\vec{u}} = 0 \tag{18-a}$$

by subtracting Equation (18-a) from (10-b):

$$\nabla\cdot\vec{u}' = 0. \tag{18-b}$$

The momentum equation (17-b) then simplifies to:

$$\frac{\partial \overline{u}}{\partial t} + \overline{\vec{u}}\cdot\nabla\overline{u} + \nabla\cdot\overline{u'\vec{u}'} = -g\,\frac{\rho}{\rho_0} - \frac{1}{\rho_0}\,\frac{\partial P}{\partial x} + \nu\nabla^2 u \tag{19-a}$$

or:

$$\frac{D\overline{u}}{Dt} = -g\,\frac{\rho}{\rho_0} - \frac{1}{\rho_0}\,\frac{\partial P}{\partial x} + \nu\nabla^2 u - \nabla\cdot\overline{u'\vec{u}'}. \tag{19-b}$$

Now, assuming that the flow is hydrostatic, the Navier-Stokes equation for the z-direction reduces to:

$$\frac{\partial P(x,z)}{\partial z} = -g\,\rho. \tag{20-a}$$

The aim here is to determine $\frac{\partial P(x,z)}{\partial x}$. So start by integrating with respect to z and using $P(x,\zeta)\equiv 0$:

$$\begin{aligned}\int_z^\zeta \frac{\partial P(x,z)}{\partial z}\,dz &= -g\int_z^\zeta \rho\,dz\\ P(x,z) - P(z,\zeta) &= -g\int_z^\zeta \rho\,dz\\ P(x,z) &= -g\int_z^\zeta \rho\,dz.\end{aligned} \tag{20-b}$$

Next, switch the order of integration and differentiation:

$$\frac{\partial}{\partial x}\int_z^\zeta \rho(x,z)\,dz = \int_z^\zeta \frac{\partial}{\partial x}\rho(x,z)\,dz + \rho(x,\zeta)\frac{\partial\zeta}{\partial x} + \rho(x,z)\frac{\partial z}{\partial x} \tag{20-c}$$

but, $\rho(x,\zeta) = \rho_0$ and $\frac{\partial z}{\partial x} = 0$, thus (20-b) becomes:

$$\frac{\partial P(x,z)}{\partial x} = -g\left[\int_z^\zeta \frac{\partial}{\partial x}\rho(x,z)\,dz + \rho_0\frac{\partial\zeta}{\partial x}\right]. \tag{20-d}$$

Substituting (20-d) into the momentum equation, (19-b), yields:

$$\frac{D\overline{u}}{Dt} = -g\,\frac{\rho}{\rho_0} - \frac{g}{\rho_0}\left[\int_z^\zeta \frac{\partial\rho}{\partial x}\,dz + \rho_0\frac{\partial\zeta}{\partial x}\right] + \nu\nabla^2 u - \nabla\cdot\overline{u'\vec{u}'}. \tag{21}$$

Reynolds stresses

Now determine a parameterization for the Reynolds stresses.

$$\nabla\cdot\overline{u'\vec{u}'} = \nabla\cdot\left(\overline{u'u'}\,\hat{i} + \overline{u'v'}\,\hat{j} + \overline{u'w'}\,\hat{k}\right) = \frac{\partial}{\partial x}(\overline{u'u'}) + \frac{\partial}{\partial y}(\overline{u'v'}) + \frac{\partial}{\partial z}(\overline{u'w'}) \tag{22}$$

The three Reynolds stress terms present in the x-equation are:

$$-\rho\overline{u'u'} = \rho\left(K_H\frac{\partial\overline{u}}{\partial x} + K_H\frac{\partial\overline{u}}{\partial x}\right) \tag{23-a}$$

$$-\rho\overline{u'v'} = \rho\Big(K_H\frac{\partial\overline{u}}{\partial y} + K_H\frac{\partial\overline{v}}{\partial x}\Big) \tag{23-b}$$

$$-\rho\overline{u'w'} = \rho\Big(K_V\frac{\partial\overline{u}}{\partial z} + K_H\frac{\partial\overline{w}}{\partial x}\Big) \tag{23-c}$$

We now introduce the following scaling:

$$\begin{aligned}
\hat{u} &= \mathbf{U}\,u \\
\hat{v} &= \mathbf{V}\,v \\
\hat{w} &= \mathbf{W}\,w \\
\hat{x} &= \mathbf{X}\,x \\
\hat{y} &= \mathbf{Y}\,y \\
\hat{z} &= \mathbf{Z}\,z \\
\hat{t} &= \mathbf{T}\,t \\
\hat{K}_H &= \mathbf{K_{Hm}}\,K_H \\
\hat{K}_V &= \mathbf{K_{Vm}}\,K_V \\
\hat{\rho} &= \rho_0\,\rho
\end{aligned}$$

where the various scales are given by: Along-channel tidal velocity $\mathbf{U} \cong 1\ m\,s^{-1}$, lateral velocity $\mathbf{V} \cong 0.10\ m\,s^{-1}$, vertical velocity $\mathbf{W} \cong 0.03\ m\,s^{-1}$, channel length $\mathbf{X} \cong 20,000\ m$, channel width $\mathbf{Y} \cong 1,000\ m$, channel depth $\mathbf{Z} \cong 10\ m$ and kinematic viscosity, ν is on the order of $10^{-6}\,m^2\,s^{-1}$.

The terms given in (23-a), (23-b),(23-c) may be simplified using the above scaling, (23-a) then becomes:

$$-\hat{\rho}\overline{\hat{u}'\hat{u}'} = 2\frac{\rho_0\mathbf{K_{Hm}U}}{\mathbf{X}}\,\rho\,K_H\frac{\partial u}{\partial x} \tag{24-a}$$

and, since $\frac{\mathbf{Y}}{\mathbf{X}} = \frac{100}{20{,}000} \ll 1$, (23-b) becomes:

$$\begin{aligned}
-\hat{\rho}\overline{\hat{u}'\hat{v}'} &= \frac{\rho_0\mathbf{K_{Hm}U}}{\mathbf{Y}}\,\rho\,K_H\Big(\frac{\partial u}{\partial y} + \frac{\mathbf{V}}{\mathbf{U}}\frac{\mathbf{Y}}{\mathbf{X}}\frac{\partial v}{\partial x}\Big) \\
&= \frac{\rho_0\mathbf{K_{Hm}U}}{\mathbf{Y}}\,\rho\,K_H\Big(\frac{\partial u}{\partial y}\Big).
\end{aligned} \tag{24-b}$$

If we assume that $\mathbf{K_{Hm}}$ is the same order of magnitude as $\mathbf{K_{Vm}}$ then, we can ignore $\frac{\partial w}{\partial x}$ in favor of $\frac{\partial u}{\partial z}$ since $\frac{\mathbf{K_{Hm}}}{\mathbf{K_{Vm}}}\frac{\mathbf{W}}{\mathbf{U}}\frac{\mathbf{Z}}{\mathbf{X}} = \frac{1}{40{,}000} \ll 1$, (23-c) becomes:

$$\begin{aligned} -\hat{\rho}\overline{\hat{u}'\hat{w}'} &= \frac{\rho_0 \mathbf{K_{Vm}} \mathbf{U}}{\mathbf{Z}}\,\rho\,K_V\Big(\frac{\partial u}{\partial z} + \frac{\mathbf{K_{Hm}}}{\mathbf{K_{Vm}}}\frac{\mathbf{W}}{\mathbf{U}}\frac{\mathbf{Z}}{\mathbf{X}}\frac{K_H}{K_V}\frac{\partial w}{\partial x}\Big) \\ &= \frac{\rho_0 \mathbf{K_{Vm}} \mathbf{U}}{\mathbf{Z}}\,\rho\,K_V\Big(\frac{\partial u}{\partial z}\Big). \end{aligned} \tag{24-c}$$

Substituting these into the Reynolds stress term, Equations (23-a), (23-b) and (23-c) become:

$$\frac{\partial}{\partial x}(\overline{u'u'}) \cong \frac{\partial}{\partial x}\left(2\,\hat{K}_H\frac{\partial \bar{\hat{u}}}{\partial \hat{x}}\right) = 2\,\frac{\mathbf{K_{Hm}}\,\mathbf{U}}{\mathbf{X}^2}\frac{\partial}{\partial x}\Big(K_H\frac{\partial u}{\partial x}\Big) \tag{25-a}$$

$$\frac{\partial}{\partial y}(\overline{u'v'}) \cong \frac{\partial}{\partial y}\left(\hat{K}_H\frac{\partial \bar{\hat{u}}}{\partial \hat{y}}\right) = \frac{\mathbf{K_{Hm}}\,\mathbf{U}}{\mathbf{Y}^2}\frac{\partial}{\partial y}\Big(K_H\frac{\partial u}{\partial y}\Big) \tag{25-b}$$

$$\frac{\partial}{\partial z}(\overline{u'w'}) \cong \frac{\partial}{\partial z}\left(\hat{K}_V\frac{\partial \bar{\hat{u}}}{\partial \hat{z}}\right) = \frac{\mathbf{K_{Vm}}\,\mathbf{U}}{\mathbf{Z}}\frac{\partial}{\partial z}\Big(K_V\frac{\partial u}{\partial z}\Big). \tag{25-c}$$

Now compare the relative scaling of these equations. Starting with the ratio of Equation (25-a) to (25-b):

$$\frac{\frac{\mathbf{K_{Hm}}\,\mathbf{U}}{\mathbf{X}^2}}{\frac{\mathbf{K_{Hm}}\,\mathbf{U}}{\mathbf{Y}^2}} = \frac{\mathbf{Y}^2}{\mathbf{X}^2} = \frac{1{,}000{,}000}{40{,}000{,}000} = \frac{1}{200} \ll 1 \tag{26}$$

therefore, $\frac{\partial}{\partial y}\overline{u'v'}$ may be neglected relative to $\frac{\partial}{\partial x}\overline{u'u'}$. And comparing Equation (25-a) to (25-c):

$$\frac{\frac{\mathbf{K_{Vm}}\,\mathbf{U}}{\mathbf{Z}^2}}{\frac{\mathbf{K_{Hm}}\,\mathbf{U}}{\mathbf{X}^2}} = \frac{\mathbf{X}^2}{\mathbf{Z}^2}\frac{\mathbf{K_{Vm}}}{\mathbf{K_{Hm}}}. \tag{27}$$

To determine the scaling of $\mathbf{K_{Vm}}$ and $\mathbf{K_{Hm}}$ consider a flow where the stress tensor is isotropic, the turbulent intensity is I_t, and the vertical and horizontal length scales are set by $\mathbf{Z}$ and $\mathbf{X}$ respectively. In this case:

$$\begin{aligned} \mathbf{K_{Vm}} &= I_t\,\mathbf{Z} \\ \mathbf{K_{Hm}} &= I_t\,\mathbf{X} \end{aligned} \tag{28}$$

Equation (27) then becomes:

$$\frac{\frac{\mathbf{K_{Hm}\,U}}{\mathbf{X^2}}}{\frac{\mathbf{K_{Vm}\,U}}{\mathbf{Z^2}}} = \frac{\mathbf{Z}^2}{\mathbf{X}^2}\frac{\mathbf{K_{Hm}}}{\mathbf{K_{Vm}}} = \frac{\mathbf{Z}^2}{\mathbf{X}^2}\frac{I_t\,\mathbf{X}}{I_t\,\mathbf{Z}} = \frac{\mathbf{Z}}{\mathbf{X}}. \tag{29}$$

Therefore, as long as $\mathbf{Z} \ll \mathbf{X}$, which is the case here, horizontal turbulent mixing may be neglected relative to vertical turbulent mixing. As a result of this scaling argument, the term given in (25-c) replaces the last term, $\nabla \cdot \overline{u'w'}$, in Equation (21), the dimensional for is now:

$$\frac{D\overline{u}}{Dt} = -g\,\frac{\rho}{\rho_0} - \frac{g}{\rho_0}\left[\int_z^\zeta \frac{\partial \rho}{\partial x}\,dz + \rho_0\frac{\partial \zeta}{\partial x}\right] + \nu\nabla^2 u + \frac{\partial}{\partial z}\left(K_V\,\frac{\partial \overline{u}}{\partial z}\right) \tag{30}$$

where all terms are dimensional, "^" has been dropped.

$$\begin{aligned}
&\frac{\mathbf{U}}{\mathbf{T}}\frac{\partial u}{\partial t} + \frac{\mathbf{U}^2}{\mathbf{X}}u\frac{\partial u}{\partial x} + \frac{\mathbf{U}^2}{\mathbf{Y}}v\frac{\partial u}{\partial y} + \frac{\mathbf{U}^2}{\mathbf{Z}}w\frac{\partial u}{\partial z} = \\
&-g\,\rho - \frac{g}{\rho_0}\left[\rho_0\frac{Z}{X}\int_z^\zeta \frac{\partial \rho}{\partial x}\,dz + \rho_0\frac{\zeta_0}{\mathbf{X}}\frac{\partial \zeta}{\partial x}\right] + \\
&\frac{\nu\,\mathbf{U}}{\mathbf{X^2}}\left[\frac{\partial^2 u}{\partial x^2} + \frac{\mathbf{X}^2}{\mathbf{Y}^2}\frac{\partial^2 u}{\partial y^2} + \frac{\mathbf{X}^2}{\mathbf{Z}^2}\frac{\partial^2 u}{\partial z^2}\right] + \frac{\mathbf{U\,K_{Vm}}}{\mathbf{Z}}\frac{\partial}{\partial z}\left(K_V\,\frac{\partial u}{\partial z}\right).
\end{aligned} \tag{31}$$

The kinematic viscosity term scales as:

$$\begin{aligned}
&\frac{\nu\,\mathbf{U}}{g\,\mathbf{X^2}}\left[1 + \frac{\mathbf{X}^2}{\mathbf{Y}^2} + \frac{\mathbf{X}^2}{\mathbf{Z}^2}\right] \\
\sim\ &\frac{10^{-6}\cdot 1}{10\cdot 20{,}000^2}\left[1 + \frac{20{,}000^2}{1{,}000^2} + \frac{20{,}000^2}{10^2}\right] \\
=\ &\left[4\,\times\,10^{-14} + 10^{-12} + 10^{-8}\right].
\end{aligned} \tag{32}$$

All of these terms are much less than the scale of $\frac{u}{g}\frac{\partial u}{\partial x}\ \sim\ 2\,\times\,10^{-5}$, therefore the entire kinematic viscosity term may be neglected. In addition, the small amplitude approximation is used and $\frac{\partial u}{\partial t}$ is neglected and lateral currents are not going to be considered. Then Equation (31) becomes:

$$\begin{aligned}
&\frac{\mathbf{U}^2}{\mathbf{X}}u\frac{\partial u}{\partial x} + \frac{\mathbf{U}^2}{\mathbf{Z}}w\frac{\partial u}{\partial z} = \\
&-g\,\rho - \frac{g}{\rho_0}\left[\rho_0\frac{\mathbf{Z}}{\mathbf{X}}\int_z^\zeta \frac{\partial \rho}{\partial x}\,dz + \rho_0\frac{\zeta_0}{\mathbf{X}}\frac{\partial \zeta}{\partial x}\right] + \\
&\frac{\mathbf{U\,K_{Vm}}}{\mathbf{Z}}\frac{\partial}{\partial z}\left(K_V\,\frac{\partial u}{\partial z}\right).
\end{aligned} \tag{33}$$

We then finally divide by $\frac{\mathbf{U}\mathbf{K_{Vm}}}{g\mathbf{Z}}$ to obtain the along-channel Reynolds equation:

$$\begin{aligned}\frac{\partial}{\partial z}\Big(K_V\,\frac{\partial u}{\partial z}\Big) &= \frac{\mathbf{U}}{\mathbf{K_{Vm}}}\Big(\frac{\mathbf{Z}}{\mathbf{X}}\,u\frac{\partial u}{\partial x}+w\frac{\partial u}{\partial z}\Big)+\frac{g\,\rho\,\mathbf{Z}}{\mathbf{U}\,\mathbf{K_{Vm}}}\\ &+ \frac{g\,\mathbf{Z^2}}{\mathbf{U}\,\mathbf{K_{Vm}}\mathbf{X}}\int_z^\zeta\frac{\partial\rho}{\partial x}\,dz+\frac{g\,\mathbf{Z}\,\zeta_0}{\mathbf{U}\,\mathbf{K_{Vm}}\mathbf{X}}.\end{aligned}\tag{34}$$

Curvature

Following the ideas of Smith and McLean [51] the $x-y-z$ equations can be transformed to a stream following coordinate system where x is now the along-stream coordinate, y is now locally normal to x and z is vertical. The conservation of mass equation becomes:

$$\frac{1}{1-\frac{y}{R}}\frac{\partial u}{\partial x}+\frac{\partial w}{\partial z}=0\tag{35}$$

and the momentum equation, (34), then becomes:

$$\begin{aligned}\frac{\partial}{\partial z}\Big(K_V\,\frac{\partial u}{\partial z}\Big) &= \frac{\mathbf{U}}{\mathbf{K_{Vm}}}\Big(\frac{\mathbf{Z}}{\mathbf{X}}\,u\frac{\partial u}{\partial x}\frac{1}{1-\frac{y}{R}}+w\frac{\partial u}{\partial z}\Big)+\frac{g\,\rho\,\mathbf{Z}}{\mathbf{U}\,\mathbf{K_{Vm}}}\\ &+ \frac{g\,\mathbf{Z^2}}{\mathbf{U}\,\mathbf{K_{Vm}}\mathbf{X}}\int_z^\zeta\frac{\partial\rho}{\partial x}\,dz+\frac{g\,\mathbf{Z}\,\zeta_0}{\mathbf{U}\,\mathbf{K_{Vm}}\mathbf{X}}\frac{\partial\zeta}{\partial x}\frac{1}{1-\frac{y}{R}}.\end{aligned}\tag{36}$$

Eddy Diffusivity

As demonstrated by Ianniello [19], the precise shape of the eddy diffusivity in the mid-water column and above; it is important that it increase from some small value at the bed to a maximum somewhere in the water column and then decrease to some small value at the surface. In the present model the eddy diffusivity is divided into a mean and a tidally (semidiurnal) varying part. For both parts, the eddy diffusivity is composed of a neutral eddy diffusivity function and a stratification correction. The mean case is presented below, the tidal case follows a similar development. A typical profile of the mean neutral eddy diffusivity used is shown in Figure (4.1).

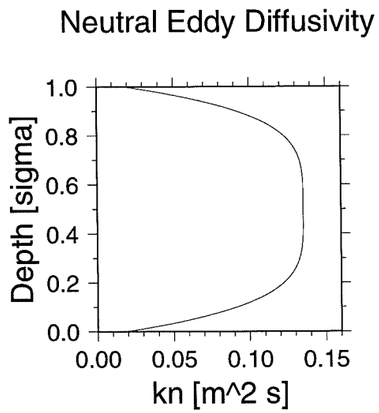


Figure 4.1: Neutral eddy diffusivity as a function of depth in σ-coordinates.

The Bloss approach for stratification correction to the neutral eddy diffusivity is used. That is the stratification correction is:

$$SR = \frac{1}{1 + g_1 \, Ri_{gT}} \tag{37}$$

where $g_1 = 3$. This function is plotted in Figure (4.2). The eddy diffusivity function used here is the product of the neutral diffusivity and the stratification correction. The composite function is shown in Figure (4.3).

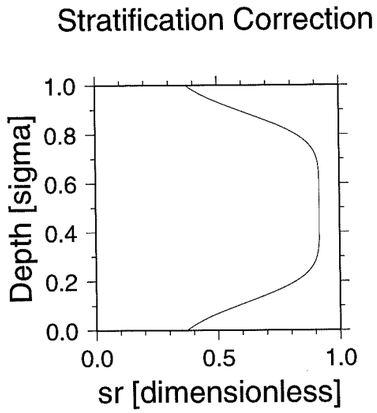


Figure 4.2: Stratification correction to the neutral eddy diffusivity as a function of depth in σ-coordinates.

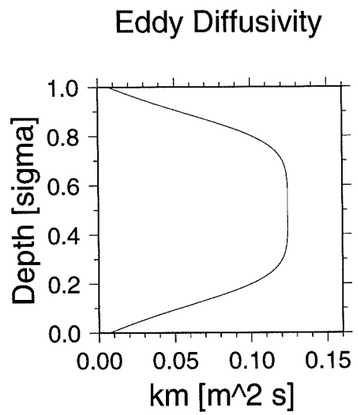


Figure 4.3: Eddy diffusivity as a function of depth in σ-coordinates.

4.4.4 *Along-Channel Momentum Equation and Separation of Modes*

The $\mathcal{O}(\varepsilon)$ mean along-channel momentum equation converted to the (x^*, y, σ, t)-coordinate system takes the form:

$$h^{-2}\frac{\partial}{\partial\sigma}(K_m\frac{\partial\overline{U}}{\partial\sigma}) - g\frac{dx^*}{dx}\frac{d\overline{\zeta}}{dx^*} = \underbrace{\overline{h^{-2}\frac{\partial}{\partial\sigma}(K_{m_1}\frac{\partial U_1}{\partial\sigma})}}_{\textit{Stress Divergence}} + \underbrace{\frac{dx^*}{dx}\overline{U_1\frac{\partial U_1}{\partial x}} + \overline{W_1\frac{\partial U_1}{\partial\sigma}}}_{\textit{Convective Accelerations}} + \underbrace{\frac{gh}{\rho_0}\frac{dx^*}{dx}[\int_\sigma^1 \frac{\partial\rho}{\partial x^*}\,d\sigma}_{\textit{Gravitational}} - \underbrace{\frac{1}{h}\frac{dh}{dx^*}\int_\sigma^1 \sigma\frac{\partial\rho}{\partial\sigma}\,d\sigma]}_{\textit{Stratification Bedslope}}. \quad (38)$$

There are three driving terms in Equation (38): the non-linear tidal convective accelerations, the non-linear stress-divergence (internal tidal asymmetry), and the two integrals associated with the non-linear gravitational circulation (in brackets). The first integral represents the effect of the mean horizontal density gradient in σ-coordinates, the second the interaction of stratification and bed slope. The convective accelerations generated by the mean flow itself are $\mathcal{O}(\varepsilon^2)$ relative to the linearly driven density $\mathcal{O}(\varepsilon)$ forcing and have therefore been neglected here. Separation of the time-average vertical eddy diffusivity K_m on the left in Equation (38) from the time varying part K_{m_1} on the right is discussed in [22]; data justifying the chosen form of K_{m_1} is discussed in Jay and Musiak [29]. Another potential forcing term is derived from the correlation of tidal fluctuations in the density field and tidal variations in surface elevation. Mathematically, it arises during time averaging of the momentum equation in the same manner as the Stokes drift in Equation (5). This term has also been neglected, because it scales as $\mathcal{O}(\varepsilon^2)$ and is thus at least one order smaller than the linear density forcing included in Equation (38). Moreover for a laterally uniform flow, the velocity associated with this flow must vanish at all depths (i.e., that this mode only slightly modifies the surface slope associated with the gravitational circulation). Removal of the requirement of lateral uniformity allows for the possibility of these non-zero flows, but this would require a laterally non-uniform along-channel pressure

gradient and will therefore be neglected for this reason.

The linear appearance of the forcing terms in (38) allows the flow associated with each of the previously defined modes (and with wind stress forcing that arises from a boundary condition) to be treated separately, and the solution procedure followed below is to treat Equations (8-b) and (38) each as the sum of five distinct equations, one for every mode. All of these modes represent phenomena that are small or $\mathcal{O}(\varepsilon)$ to the $\mathcal{O}(1)$ tidal flow, but each will have a specific value of ε associated with it as noted in Jay [22]; thus for the along-channel velocity $\overline{U}$, the vertical velocity $\overline{\omega}$ and the surface slope $\overline{S} = \frac{\partial \overline{\zeta}}{\partial x}$:

$$\begin{aligned} \varepsilon\overline{U} &= \varepsilon_G\overline{U}_G + \varepsilon_R\overline{U}_R + \varepsilon_B\overline{U}_S + \varepsilon_I\overline{U}_I + \varepsilon_B\overline{U}_B \\ \varepsilon\overline{S} &= \varepsilon_G\overline{S}_G + \varepsilon_R\overline{S}_R + \varepsilon_B\overline{S}_S + \varepsilon_I\overline{S}_I + \varepsilon_B\overline{S}_B \\ \varepsilon\overline{\omega} &= \varepsilon_G\overline{\omega}_G + \varepsilon_R\overline{\omega}_R + \varepsilon_B\overline{\omega}_S + \varepsilon_I\overline{\omega}_I + \varepsilon_B\overline{\omega}_B \end{aligned} \tag{39}$$

where the subscript "G" denotes gravitational circulation, "R" is for riverflow, "S" is Stokes drift velocity, "I" is internal asymmetry and "B" is for tidal non-linear residual flow.

4.4.5 Determination of flow Distribution

Riverflow mode

The distribution of the mean riverflow and Stokes drift compensation flow in an estuary are the simplest residual flow modes, and the riverflow solution illustrates the methods to be used, with some variations, for all the residual flow modes discussed here. The riverflow problem is therefore treated in detail, with the other modes being presented in a more summary fashion. The mass and momentum conservation equations given in dimensional form by Equations (7-a), (8-b) and (38) can be non-dimensionalized for the riverflow mode using the following scaling:

$$h = \mathbf{H}H$$

$$\begin{aligned}
\varepsilon_R\overline{\omega}_R &= \frac{\mathbf{U}}{L_T}W_R \\
\overline{\varepsilon}_R\overline{U}_R &= \varepsilon_R\mathbf{U}\overline{U}_R \\
\overline{K}_m &= \mathbf{K}\overline{K} \\
\frac{\partial\overline{\zeta}_R}{\partial x^*}\Big(\frac{1}{1-\frac{y}{\mathcal{K}}}\Big) &= \frac{\zeta_0}{L_R}S_R\Big(\frac{1}{1-\frac{y}{\mathcal{K}}}\Big) \qquad \text{(40-a)}
\end{aligned}$$

yielding one non-dimensional parameter Π_R that determines the slope amplitude relative to the depth and bedstress:

$$\Pi_R = \frac{S_R g H}{\varepsilon_R k u_* U} \qquad \text{(40-b)}$$

with: S_R = slope of river surface, $\mathbf{K} = ku_*\mathbf{H}$ and $\varepsilon_R = \frac{\mathbf{U}_R}{\mathbf{U}}$. The non-dimensional along-channel momentum equation for the riverflow is:

$$\frac{\partial}{\partial\sigma}(K_m\frac{\partial U_R}{\partial\sigma}) = gh^2\frac{d\overline{\zeta}_R}{dx^*}\frac{dx^*}{dx} = gh^{(3-\frac{n}{2})}(\frac{b_t}{b})^{\frac{1}{2}}\frac{\partial\zeta_R}{\partial x^*}\Big(\frac{1}{1-\frac{y}{\mathcal{K}}}\Big) \qquad \text{(41-a)}$$

with the condition:

$$\int_{-\frac{b}{2}}^{+\frac{b}{2}} H\int_0^{\zeta_R} U_R\,dz\,dy = +Q_R. \qquad \text{(41-b)}$$

A separation of variables is assumed of the form:

$$\begin{aligned}
\mathbf{U}_R\overline{U}_R &= \mathbf{U}_R M_R(X^*)\overline{P}_R(\sigma;X^*,Y) && \text{(42-a)}\\
\overline{\zeta}_R(X^*) &= \int_0^X M_R(X^*)\,Z_R(;X^*)\,dX^* && \text{(42-b)}\\
M_R(X^*) &= \sqrt{BB_t}\,H^{(2-\frac{n}{2})} && \text{(42-c)}
\end{aligned}$$

where the notation $f(;X^*)$ indicates a parametric dependence on X^* through B, B_t and $\{H\}$. The riverflow velocity profile is then determined from Equation (41-a):

$$M_R\frac{d}{d\sigma}\Big[K(\sigma)\frac{d\overline{P}_R}{d\sigma}\Big] = (b\,b_T)^{\frac{1}{2}}\,h^{(3-\frac{n}{2})}\,\Pi_R\,\frac{\partial\zeta_R}{\partial x^*}\Big(\frac{1}{1-\frac{y}{\mathcal{K}}}\Big). \qquad \text{(43-a)}$$

And, (41-b) becomes:

$$\int_{-\frac{B}{2}}^{+\frac{B}{2}} H\int_{\sigma_0}^1 \overline{P}_R\,d\sigma\,dy = -\frac{1}{M_R(X^*)}. \qquad \text{(43-b)}$$

The minus sign in Equation (43-b) indicates that the riverflow is always outward or negative. The boundary conditions for the riverflow problem are no-slip at the bed and an unstressed free surface, so from the separation of variables (40-a):

$$\overline{P}_R|_{\sigma_0} = 0 \tag{44-a}$$

$$\frac{\partial \overline{P}_R}{\partial \sigma}|_1 = 0. \tag{44-b}$$

The riverflow surface elevation meets the condition that the riverflow cannot effect the sea surface height:

$$\overline{\zeta}_R(x^*)|_{x^*=0} = 0 \tag{44-c}$$

a condition which has already been included in the surface-elevation definition Equation (42-b). Finally, the non-dimensional σ-coordinate vertical velocity associated with the riverflow $\overline{\omega}_R$, can be determined from integration of Equation (8-a) with respect to σ (using Equations (42-a) and (42-b)), and the boundary condition that $\overline{\omega}_R$ vanishes at the bed:

$$\overline{w}_R = -\frac{b_t}{b} h^{(2-n)} [\frac{\alpha+\beta}{2} + (2-\frac{n}{2})\gamma] \int_{\sigma_0}^{1} P_R \, d\sigma \tag{45-a}$$

$$\overline{\omega}_R|_{z_0} = 0. \tag{45-b}$$

The dimensional vertical velocity ($\overline{w}_R$) is then determined from the relationship in Equation (8-b) to the Eulerian vertical velocity:

$$\overline{W_R} = [\overline{\omega}_R + \alpha l (\frac{B}{B_t H})^{\frac{1}{2}}]. \tag{46}$$

The profile equation Equation (43-a) can be integrated twice to yield a closed-form expression for $\overline{P}_R$. Here as in the following cases, channel curvature is taken into account. The same development is used as Smith and McLean [51] and was presented in the last section. The surface slope can determined by integrating a third time and applying conservation of mass:

$$P_R = -\frac{1}{I_5(1)} \int_{\sigma_0}^{\sigma} \frac{\sigma' - 1}{K(\sigma')} \, d\sigma' \tag{47-a}$$

$$\frac{\partial \overline{\zeta_R}}{\partial x^*} = [-\Pi_R\, I_5(1)]^{-1} \qquad (47\text{-b})$$
$$I_5(\sigma) = \int_{\sigma_0}^{\sigma}\int_{\sigma_0}^{\sigma'} \frac{\sigma''-1}{K(\sigma'')}\, d\sigma''\, d\sigma'.$$

A double numerical integration involved in satisfying Equation (43-b) is, however, slow. It is numerically more efficient to integrate Equation (43-a) symbolically once employing (47-a, 47-b) and the boundary condition at the free surface Equation (44-b) to obtain a first-order differential equation:

$$\frac{\partial \overline{P}_R}{\partial \sigma} = -\frac{1}{I_5(1)}\frac{\sigma-1}{K_m}. \qquad (48)$$

The linearity of Equation (48) with respect to I_5^{-1} and the assumption of a laterally uniform surface slope allow a solution to be attained by a "shooting method", where the unknown condition that must be guessed is the value of I_5^{-1} that yields the correct integral transport (43-b) rather than a second boundary condition. The procedure employed is to guess a value of I_5^{-1}, solve Equation (48) at $\mathcal{O}(10)$ locations in the cross-section using the Mathematica function DSolve to obtain provisional solutions $\overline{P}_R$, integrate each of the $\overline{P}_R$, sum these over the section, use the discrepancy from the correct answer to Equation (43-b) to guess a new value of I_5^{-1}, and iterate to convergence. The vertical velocity terms $\overline{W}_R$ and $\overline{\omega}_R$ can then be determined by numerical integration of Equation (45-a). Note finally that the formulation employed in Equation (45-a) neglects the parametric X^*-variation of $P(\sigma; X^*, Y)$ through $S_R(X^*, Y)$ as small relative to the topographically induced variations in $M_R(X^*)$. The basic solution procedure embodied in Equations (41-a) to (48) is then employed for all the residual flow modes except for the non-linear tidal mode. The expression (48) from which the velocity profile is determined contains no non-dimensional numbers, because the magnitude of the discharge has been specified by (7-a) and incorporated into (48); there are no free parameters. The result is a velocity profile that increases in magnitude monotonically from the bed in a manner determined by the bed roughness and the eddy diffusivity profile. The sensitivity of results to the mixing parameter-

ization will be noted below. Only the magnitude of the surface slope necessary to achieve the required discharge is affected by Π_R.

Baroclinic flow mode

Scaling for the baroclinic, or gravitational, circulation problem is as follows:

$$\begin{aligned} \varepsilon_G &= (\frac{\Delta\rho_V}{\rho_0})^{\frac{1}{2}} \\ \mathbf{U}_G &= \sqrt{g\frac{\Delta\rho_V}{\rho_0}H} \\ \varepsilon_G\mathbf{U}_G &= \frac{\Delta\rho_V}{\rho_0}\sqrt{gH}. \end{aligned} \tag{49}$$

The perturbation parameter given here as ε_G is a measure of the tendency of $\mathcal{O}(1)$ tidal frequency internal wave motion, driven by a horizontal density gradient, to occur. Although there is a tidal-frequency motion driven by the time-varying density field, Jay [22], an analysis of the pertinent internal wave equation shows the the steady density forcing cannot drive such a motion, as discussed by Jay [24] and Jay and Smith [33]. Thus, the motion actually forced by steady density forcing is the gravitational circulation discussed herein. The scale velocity for this motion ($\varepsilon_G u_G$) is given in Equation (49), and the surface slope associated with the gravitational circulation is $\frac{\partial\zeta_G}{\partial x} \sim \mathcal{O}(\varepsilon_G^2\frac{\eta}{L_S})$ rather than $\mathcal{O}(\varepsilon_G\frac{\eta}{L_S})$. That is, the gravitational circulation is an internal mode, the magnitude of which is small relative to the dominant tidal circulation. Its surface slope must then be small relative to that for an $\mathcal{O}(\varepsilon)$ external mode, which would be $\mathcal{O}(\varepsilon_G\frac{\eta}{L_S})$. The surface slope for this mode must still be calculated, however, because conservation of mass is not otherwise possible.

The velocity $\overline{U}_G$ and surface slope $\frac{\partial\overline{\zeta}_G}{\partial x}$ are represented in terms of a separation of variables as:

$$\overline{U}_G = M_G(X^*)\overline{P}_G(\sigma;X^*,Y) \tag{50-a}$$

$$\overline{\zeta}_G(X^*) = \int_0^X M_G(X^*)Z_G(;X^*)dX^* \tag{50-b}$$

$$M_G(X^*) = \sqrt{\frac{B_T}{B}} H^{3-\frac{n}{2}} \tag{50-c}$$

$$\overline{W}_G(X^*) = -\frac{1}{H}\frac{\partial(\overline{U}_G H)}{\partial x^*} \tag{50-d}$$

where $\frac{\partial \overline{\zeta}_G(;x)}{\partial x}$ varies only parametrically with $B(X^*)$, $B_t(X^*)$ and $\{H(X^*, Y)\}$. The form of $M_G(X^*)$ is a consequence of the assumptions of central regime theory, specifically, because the horizontal density gradient is constant, there is no X^* variation in $\overline{U}_G$ except for that introduced by distorting X to X^*. Applying the above scaling and separation of variables Equation(50-a) to the "Gravitational" term of Equation (38), and integrating once symbolically, yields the non-dimensional profile equation for the gravitational circulation problem:

$$\frac{\partial \overline{P}_G}{\partial \sigma} = (\frac{b_T}{b})^{\frac{1}{2}} \frac{h^{2-\frac{n}{2}}}{\overline{K}_m}\Big[\Pi_1 \frac{\partial \overline{\zeta}_G}{\partial x^*} \cdot \Big(\frac{1}{1-\frac{y}{\mathcal{K}}}\Big) \cdot (\sigma - 1) + h\Pi_2^{'}\, DF\Big] \tag{51-a}$$

$$DF = \sigma - \frac{\sigma^2}{2} - \frac{1}{2} - \varepsilon_\rho \int_\sigma^1 \int_{\sigma'}^1 \frac{\partial \overline{\rho}}{\partial \sigma}\, d\sigma d\sigma^{'} + \frac{\Pi_2^{''}}{\Pi_2^{'}}\sigma \int_\sigma^1 \frac{\partial \overline{\rho}}{\partial \sigma}\, d\sigma \tag{51-b}$$

$$\Pi_1 = \frac{gH^2\eta_G}{K_0 \mathbf{U_G L_s}}$$

$$\Pi_2^{'} = -\frac{\Delta\rho}{\rho_0}\frac{gH^2}{ku_\star \mathbf{U_G L_s}}$$

$$\Pi_2^{''} = -\varepsilon_\rho \Pi_2^{'} \frac{L_s}{\lambda}\gamma l$$

and γ is the depth e-folding length as defined in (4), L_s is the salinity intrusion scale length and l is the scale length over which γ varies.

The boundary conditions for $\overline{U}_G$ are again no-slip at the bed and an unstressed free surface and therefore, $\overline{P}_G$ must satisfy:

$$\overline{P}_G|_{\sigma=0} = 0 \tag{51-c}$$

$$\frac{\partial \overline{P}_G}{\partial \sigma}|_{\sigma=1} = 0. \tag{51-d}$$

For the gravitational mode, there is no net mass transport and the conservation equation takes the form of the integral condition:

$$\int_{-\frac{b}{2}}^{\frac{b}{2}} \int_0^{\zeta_G} \overline{U}_G dz = 0. \tag{51-e}$$

Translating this to a condition on $\overline{P}_G$ by using Equation (50-c) gives:

$$\int_{-\frac{b}{2}}^{\frac{b}{2}} \int_{\sigma_0}^{1} \overline{P}_G d\sigma = 0. \tag{51-f}$$

The surface slope associated with the gravitational circulation arises from the zero-transport requirement — without this surface slope, there would be a net landward transport which is forbidden by the boundary conditions of Equations (6-a, 6-b). The boundary condition for the vertical velocity is that $\overline{w}_G$ vanishes at the bed; $\overline{w}_G$ is determined from a relationship analogous to Equation (45-a). The solution method for the gravitational circulation is analogous to that for the riverflow. This solution method generalizes on the central regime theory both with regard to realistic representation of the eddy diffusivity K_m and in that a realistic vertical profile for along-channel density forcing may be employed. An eddy diffusivity turbulence closure with a stratification correction is used herein, but other closures could be implemented. The density forcing function (DF from Equation (51-b) used here is given in Equation (51-b) and plotted in Figure (4.4); an increase with depth is typical. The function shape is a result of a stratified flow, with a constant density layer on the bottom, transitioning to a layer of lower density at the surface. The density forcing may be represented by any physically realistic function, but analytical integrability facilitates numerical computation. Using the mass conservation condition that the gravitational circulation integrate to zero, Equation (51-a) then results in a differential equation with the non-dimensional number Π_2', representing the strength of the density forcing. The gravitational circulation solution, because it contains an explicit density forcing term, is not monotonic in σ. The shape of the resulting velocity profile, in particular the strength of the landward and seaward flows are determined by Π_2', the form of the density profile ($\rho(\sigma)$) bed roughness, the eddy diffusivity K_m and the bed-slope. Even more than the river flow velocity, the sectional distribution of the gravitational circulation is influenced by the mixing parameterization employed. Only the slope necessary to achieve the specified zero discharge is influenced by Π_1',

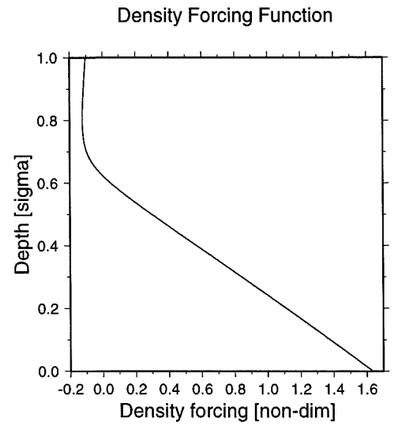


Figure 4.4: Sample density forcing (DF from Equation (51-b) showing typical increase with increasing depth. Shown as non-dimensional forcing against depth in σ-coordinates.

as is the case with all the residual flow modes.

Wind Driven Circulation

The residual circulation in an estuary can be effected by local atmospheric forcing. The basic circulation pattern for this mode is the surface moves in the direction of the wind, here assumed to be only along the channel axis, and the compensating flow in the opposite direction at depth. In this section the velocity profile equations are developed for the wind driven circulation. The basic dimensional equation is:

$$\frac{\partial}{\partial z}\left[K_m \frac{\partial U_W}{\partial z}\right] = -g \frac{\partial \zeta_W}{\partial x}\left(\frac{1}{1-\frac{y}{\mathcal{K}}}\right) \tag{52}$$

with the boundary conditions:

$$\left.\frac{\partial U_W}{\partial z}\right|_{z=\zeta_W} = -\frac{\tau_s}{\rho_0 K_m|_{z=\zeta_W}} \tag{53-a}$$

$$\left.U_W\right|_{z=0} = 0. \tag{53-b}$$

These boundary conditions relate the speed of the wind over the surface of the water to the shear stress at the surface through the relationship $\tau_s \simeq C_D\ \rho\ u_{wind}$, where $C_D = 1.1\ \times 10^{-3}$ (Gill [13]) and impose a no-slip condition at the bed. A separation of variables is then applied:

$$\mathbf{U_W}\overline{U}_W = \mathbf{U_W}\ M_W(X^*)\ \overline{P}_W(\sigma; X^*, Y) \tag{54-a}$$

$$M_W(X^*) = \sqrt{\frac{b}{b_t}}\ h^{2-\frac{n}{2}} \tag{54-b}$$

along with the non-dimensionalizations:

$$\begin{aligned} \tau_s &= \tau_{\mathbf{0}}\ \tau \\ K_m(\sigma) &= \mathbf{K_0}\ K(\sigma) \\ z &= \mathbf{H_0}\ h(X^*)\ \sigma \\ \zeta_W &= \zeta_{\mathbf{0}}\ \zeta \\ x &= X\ l_s. \end{aligned} \tag{55}$$

The differential equation, (52), then becomes:

$$\frac{\partial}{\partial\sigma}\left[K(\sigma)\ \frac{\partial\overline{P}_W}{\partial\sigma}\right] = -\Pi_W\ \frac{\partial\zeta_W}{\partial X^*}\left(\frac{1}{1-\frac{y}{\mathcal{K}}}\right) \tag{56}$$

$$\Pi_W = g\frac{\zeta_0\mathbf{H_0^2}}{\mathbf{K_0U_W}\ l_s}. \tag{57}$$

The same scaling is then applied to the boundary conditions (53-a) and (53-b), yielding:

$$\left.\frac{\partial\overline{P}_W}{\partial z}\right|_{\sigma=1} = -\Pi_1\ \frac{\tau h(X^*)}{M(X^*)K(1)} \tag{58-a}$$

$$\Pi_1 = \frac{\tau_{\mathbf{0}}\ \mathbf{H_0}}{\rho_0\mathbf{U_WK_0}}$$

$$\left.\overline{P}_W\right|_{\sigma=0} = 0. \tag{58-b}$$

The next step is to integrate (56) with respect to σ and apply the surface boundary condition (58-a) which yields the final non-dimensional differential profile equation

for the wind driven circulation:

$$\frac{\partial \overline{P}_W}{\partial \sigma} = -\Pi_W \frac{\partial \zeta}{\partial X^*} \left(\frac{1}{1-\frac{y}{K}}\right)\left(\frac{\sigma-1}{K(\sigma)}\right) - \Pi_1 \frac{\tau\, h(X^*,Y)}{M(X^*)K(1)}. \tag{59}$$

As with the previous modes, a surface slope is assumed, (59) is solved subject to the no-slip boundary condition, (58-b), for a number of profiles in a cross-channel section. These profiles are integrated in depth and width to check if mass is conserved. For this circulation mode there is no net mass transport:

$$\int_{-\frac{B}{2}}^{+\frac{B}{2}} \int_0^1 \overline{P}_W \, d\sigma \, dY \;=\; 0. \tag{60}$$

The assumed surface slope is adjusted until this condition is met.

Tidal Flow Mode

The tidal flow modes are discussed in detail in Jay [22], but an outline of the basic equations is given here. The tidal profile equation is:

$$\begin{aligned} &\frac{1}{h^2}\frac{\partial}{\partial\sigma}\Big(K_m \frac{\partial U_1}{\partial \sigma}\Big) \;-\; \Big[\frac{\partial U_1}{\partial t} + \Big(U_1 \frac{1}{1-\frac{y}{K}} \frac{\partial U_R}{\partial x}\frac{dx^*}{dx} + \overline{w}_R \frac{\partial U_1}{\partial \sigma}\Big)\frac{b_T}{b}\Big] \\ &= \frac{dx^*}{dx}\Big(g\frac{\partial \zeta}{\partial x^*}\,\frac{1}{1-\frac{y}{K}} \;+\; \frac{g\,h}{\rho_0}\int_\sigma^1 \frac{\partial \rho}{\partial x^*}\,d\sigma - \frac{1}{h}\frac{dh}{dx^*}\int_\sigma^1 \frac{\partial \rho}{\partial \sigma}\,d\sigma\Big). \end{aligned} \tag{61}$$

Which after a separation of variables and some manipulation is:

$$\begin{aligned} K\,P'' \;+\; & f_1(\sigma;x^*,y)\,P' - i\,m\,h^2 f_2(\sigma;x^*,y)\,P\,\frac{1}{1-\frac{y}{K}} \\ \cong\; & -i\,h^{2-n}\,(C^{\pm})\,m + i(\frac{b_T}{b})^{\frac{1}{2}}\,h^{3-n}\times \\ & \Big[\Omega_1(C^- + 2\frac{A}{B}\,i\,q)\int_\sigma^1 1+\varepsilon_\rho f(\sigma)\,d\sigma - \gamma l\Omega_2\int_\sigma^1 \sigma f'(\sigma)\,d\sigma\Big]. \end{aligned} \tag{62}$$

Where:

$$\begin{aligned} \Omega_1 &= (\frac{\Delta\rho}{\rho_0})(\frac{l}{L_s})^2 m e^{i\phi} \\ \Omega_2 &= \frac{L_s}{l}\varepsilon_\rho \Omega_1 \end{aligned}$$

$$
\begin{aligned}
f_1(\sigma; x^*, y) &= K'_m(\sigma; x^*, y) + \varepsilon_R m^2 h^2 \overline{w}_R \\
f_2(\sigma; x^*, y) &= 1 + i\varepsilon_R \frac{\partial x^*}{dx} \frac{\partial U_R(\sigma; x^*, y)}{\partial x^*} \\
\varepsilon_R &= \varepsilon \frac{\mathcal{U}_{\mathrm{R}}}{\mathcal{U}} \frac{l}{L_T} \frac{b_T}{b} \\
m &= \frac{\omega H^2}{K_0}.
\end{aligned} \tag{63}
$$

Additionally:

$$
\begin{aligned}
C^{\pm} &= (\frac{\Delta}{2})^2 + q_1^2 \\
\Delta &= \alpha + \beta + n\,\gamma \\
C^{-} &= \frac{\Delta}{2} \\
q_1 &= 1 - (\frac{\Delta}{2})^2 - I\frac{R}{\omega}.
\end{aligned} \tag{64}
$$

Non-Linear Residual Flow Generated by Internal Tidal Asymmetry

The distribution of non-linear residual flow which is generated by internal tidal asymmetry is one of the more complicated circulation modes found in estuaries. It is generated by the interaction of the tidal frequency current and the tidal frequency eddy viscosity, ω_1 and ω_2 in Equation (65) where $\omega_1 = \omega_2$. Non-linear interactions that yield sums and differences in frequency can be seen from the trigonometric identity:

$$
Cos(\omega_1 t) \times Cos(\omega_2 t) = \frac{1}{2} Cos([\omega_1 - \omega_2]t) + \frac{1}{2} Cos([\omega_1 + \omega_2]t). \tag{65}
$$

Terms at all frequencies interact: for example, the interaction of K_1 with M_2 generates flows at K_1 and M_3, or more properly MK_3 frequencies. Terms at these newly generated frequencies again interact producing a full spectrum of overtide flows. These successive currents are usually much too small to be of concern. The more important cases have $\omega_1 = \omega_2$ thus generate a zero-frequency, or residual, flow and a double-frequency, or overtide flow. The two cases considered in this dissertation are driven by currents and eddy viscosity both in the M_2 band. The residual flow is discussed

first. The governing equation for this mode is:

$$\frac{\partial}{\partial z}\left[K\frac{\partial \overline{U}_I}{\partial z}\right] = g\frac{\partial \overline{\zeta}}{\partial x}\frac{1}{1-\frac{y}{\kappa}} + \frac{g}{\rho_0} int_z^1 \frac{\partial \rho}{\partial z}\, dz' - \frac{\partial}{\partial z}\overline{\left[K_1\frac{\partial U_1}{\partial z}\right]} \tag{66}$$

which when scaled yields the non-dimensional, scaled equation for zero-frequency:

$$\frac{\partial}{\partial z}\left[K\frac{\partial \overline{U}_I}{\partial z}\right] = r_I\frac{\partial \zeta_I}{\partial x}\frac{1}{1-\frac{y}{\kappa}} - \frac{\mathbf{U_i}}{\mathbf{U_I}\varepsilon_1}\frac{\partial}{\partial z}\overline{\left[K_*\frac{\partial U_1}{\partial z}\right]} \tag{67}$$

where the subscript "I" indicates Internal tidal asymmetry and the subscript "1" denotes a tidal frequency variable. Then applying a separation of variables:

$$\begin{aligned}
U_I &= \mathbf{U_I}\, M'(X^*)\overline{P}_I(\sigma) \\
\zeta_I &= C_3 M(X^*) \\
\frac{\partial \zeta_I}{\partial x} &= C_3 M'(X^*) \\
r_I &= \frac{\zeta_I}{H}\frac{\sqrt{gH}}{\mathcal{U}_1}\varepsilon_1\frac{\lambda}{\mathrm{L_s}}\mathrm{m} \\
\mathbf{U_I} &= \gamma\sqrt{H\frac{g\Delta\rho_H}{\rho_0}} \\
\mathbf{U_i} &= \gamma\sqrt{H\frac{g\Delta\rho_v}{\rho_0}} \\
\varepsilon_i &= \gamma\sqrt{H\frac{g\Delta\rho_H}{\rho_v}} \\
\gamma^2 &= \frac{g\Delta\rho_{vT}}{\Delta\rho_r v0} \\
m &= \frac{\omega H^2}{2K}
\end{aligned} \tag{68}$$

where $M_I(X^*)$ has the same form as in (50-d) and C_3 is the scaling amplitude for the surface slope. Integrating Equation (67) vertically and applying the free surface boundary condition

$$\left.\frac{\partial U_I}{\partial z}\right|_{z=1} = 0 \tag{69}$$

yields the differential equation for the non-linear residual mode:

$$\frac{\partial P_I}{\partial \sigma} = \frac{r_I\, C_3}{K}(\sigma-1)\frac{1}{1-\frac{y}{\kappa}} - \frac{\mathbf{U_i}}{2\mathbf{U_I}\varepsilon_1}\frac{K_1}{K}\frac{\partial P_1}{\partial \sigma}. \tag{70}$$

Then to obtain the value of C_3, setting the associated surface slope, Equation (70) is integrated in the vertical a second time and the boundary condition at the bed is applied:

$$P_I\Big|_{\sigma=0} = 0 \tag{71}$$

and finally continuity:

$$\int_{\sigma_0}^{1} P_I \, d\sigma = 0 \tag{72}$$

is invoked through a third integration.

Non-Linear Over-Tide Flow Generated by Internal Asymmetry

The driving mechanism for this mode is the same as the last (non-linear residual) except that it is generated by the sum of the frequencies, the second term on the right hand side of Equation (65):

$$\frac{\partial}{\partial z}\left(\overline{K}_m \frac{\partial U_{I2}}{\partial z}\right) - \frac{\partial U_{I2}}{\partial t} + T_{b_{I2}} = \frac{\partial}{\partial z}\overline{\left(K_1 \frac{\partial U_1}{\partial z}\right)}. \tag{73}$$

Applying the following separation of variables:

$$\begin{aligned} U_1 &= \mathbf{U_1}\, \mathcal{R}\mathrm{e}[\mathrm{M}'(\mathrm{x})\mathrm{P}_1(\mathrm{z})\mathrm{e}^{\mathrm{it}}] \\ U_{I2} &= \mathbf{U_I}\varepsilon_\mathrm{I}\, \mathcal{R}\mathrm{e}[\mathrm{M}'(\mathrm{x})\mathrm{P}_{\mathrm{I2}}(\mathrm{z})\mathrm{e}^{2\mathrm{it}}] \\ K_1 &= K_0\, \mathcal{R}\mathrm{e}[\mathrm{K}_1\, \mathrm{e}^{\mathrm{it}}] \\ T_{b_{I2}} &= M'(x)e^{2it}\frac{u_\star^2}{H}\frac{T_b}{h} \end{aligned} \tag{74}$$

yields the differential equation to be solved (here a prime indicates a vertical derivative, $\frac{\partial}{\partial\sigma}$):

$$\overline{K}_m P''_{I2} + \overline{K}'_m P'_{I2} - 2\, i\, m\, P_{I2} + \frac{U_\star\, T_{b_{I2}}}{k\mathbf{U_I}\varepsilon_\mathrm{I}(1-\sigma_0)} = -\frac{1}{2}\frac{\mathbf{U_1}}{\varepsilon_\mathrm{I}\mathbf{U_I}}\left(K_1 P''_1 + K'_{m1} P'_1\right) \tag{75}$$

and the value of $T_{b_{I2}}$ is determined by vertically integrating and applying boundary conditions Equations (69) and (71) at the surface and the bed.

$$T_{b_{I2}} = \frac{1}{2}\frac{\mathbf{U}}{\mathbf{U_I}}(\mathrm{K}_1\mathrm{P}'_1)|_{\sigma_0} + \varepsilon_\mathrm{I}(\overline{\mathrm{K}}_\mathrm{m}\mathrm{P}'_{\mathrm{I2}})|_{\sigma_0} \tag{76}$$

The constant T_{bI2} is the sum of two terms: 1) the tidally varying eddy diffusivity times the tidal velocity shear and 2) the mean eddy diffusivity times the overtide velocity shear both evaluated at the bed. This is essentially the bedstress caused by internal tidal asymmetry.

4.5 Results

4.5.1 Comparison to data

Using the density data from the along-channel sections presented in Chapter 2, the along-channel ($\frac{\partial \rho}{\partial x}$) and vertical ($\frac{\partial \rho}{\partial z}$) gradients were determined for the residual, diurnal and semidiurnal flow modes (see Figures (2.10), (2.12) and (2.14) in Chapter 2). Salinity profile functions were also determined and Total Gradient Richardson number, $Ri_{gT} = \frac{N^2}{(\frac{\partial u}{\partial z})^2 + N^2}$, profiles were calculated using the density and velocity data. The incident and reflected tidal height amplitudes and phases for the diurnal and semidiurnal frequencies, friction factors determined from the 1-D barotropic model were also used as input for the profile model. The topography of this section of channel is shown in Figure (4.5). The model was run for 8 separate channel cross-sections in the south channel of the Columbia River estuary, representing the area of data collection discussed in Chapter 2. Tidal flats were included in the model for cross-sections where they were present in the river. Again, the tidal flats are only momentum sinks and mass storage, currents on the tidal flats are not considered. The stars, $\star$, along the bottom of the following contour plots represent where the model was run. For each channel cross-section, velocity profiles were calculated at 7 non-dimensional cross-section locations: $(-\frac{1}{2}, -\frac{1}{3}, -\frac{1}{6}, 0, +\frac{1}{6}, +\frac{1}{3}, +\frac{1}{2})$, where 0 is the center of the channel and $\pm\frac{1}{2}$ represent the channel edges. For each cross-section, the profile which best matched the depth from the velocity data was selected and the 8 profiles were plotted together to generate along channel plots. The model output for the riverflow is shown in Figure (4.6). The changes in the along-channel river flow

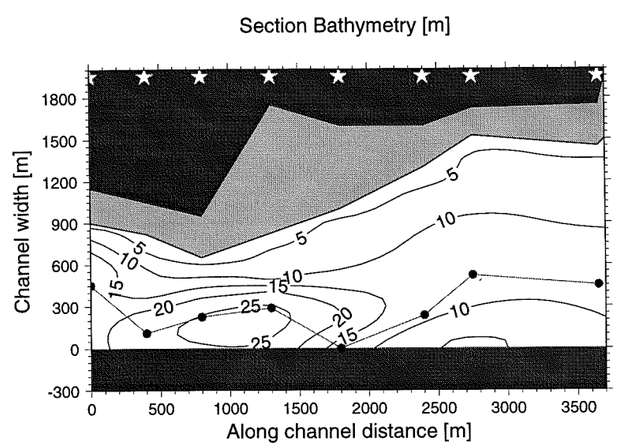


Figure 4.5: Contour plot showing channel bathymetry in meters on MLW. The x-axis is the along-channel distance for this section, y-axis is cross-channel distance from the southern shore. The width of the momentum carrying portion of the channel is shown in white and the total channel width (gray) includes tidal flats. The circles indicate the profile from each cross-section used to construct the along-channel contour plots. The stars mark the along channel positions of the cross-channel sections used. For each section, the the channel width is centered on zero.

can be attributed to 2 factors: change in channel cross-sectional area and channel curvature. A decrease in channel area increases the river currents and an increase in are results in the currents decreasing because the river transport is constant in the channel. Channel curvature has the effect of laterally displacing the fastest flow to the outside of the channel. The baroclinic circulation, Figure (4.7), is influenced by

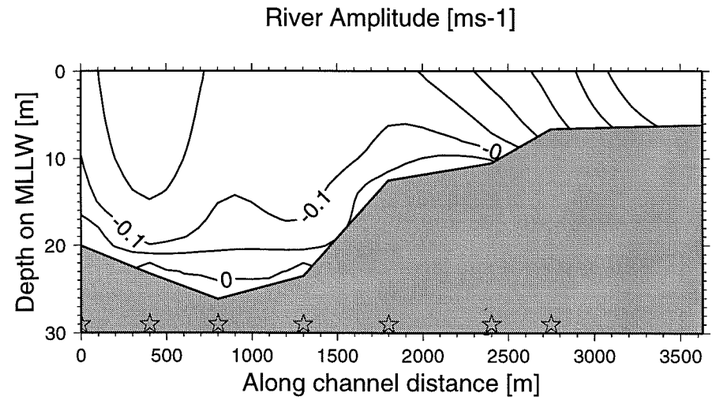


Figure 4.6: Along-channel riverflow in $[m\ s^{-1}]$.

channel depth — the inflow is strongest flowing down the bed slope to the deepest part of the channel and channel curvature — the denser bottom water flow is strongest on the outside of the channel. The currents shown in the contour plot do not integrate to zero because the plot is generated using one profile from each cross-section and the condition of mass conservation is applied to the entire cross-section and not to individual profiles. The non-linearly generated residual flow, Figure (4.8), has its origins in the semidiurnal tidal currents, Figure (4.12), and therefore also its form. The combined residual flow, Figure (4.9), is the scaled sum of the riverflow, baroclinic residual and the non-linearly generated tidal residual. It is approximately the same flow that is determined from data in Figure (2.9). It is important to note here that the observed residual flow and all of the individual calculated modes which make up

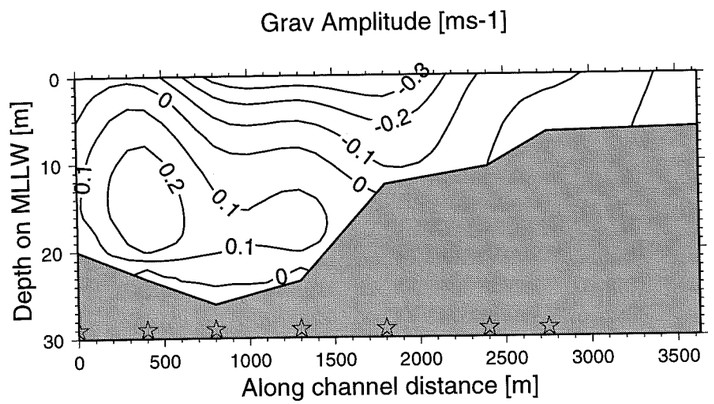


Figure 4.7: Along-channel gravitational circulation in $[m\ s^{-1}]$.

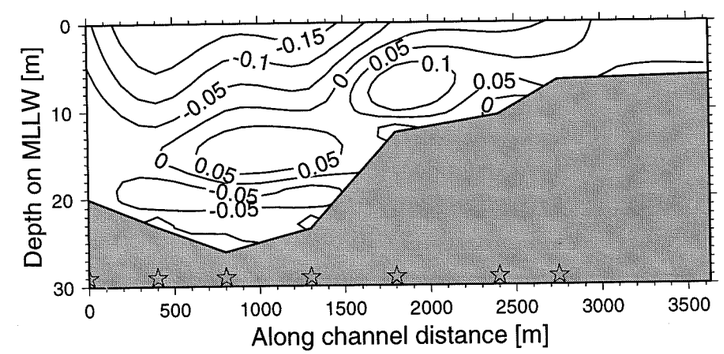


Figure 4.8: Along-channel non-linear residual circulation in $[m\ s^{-1}]$.

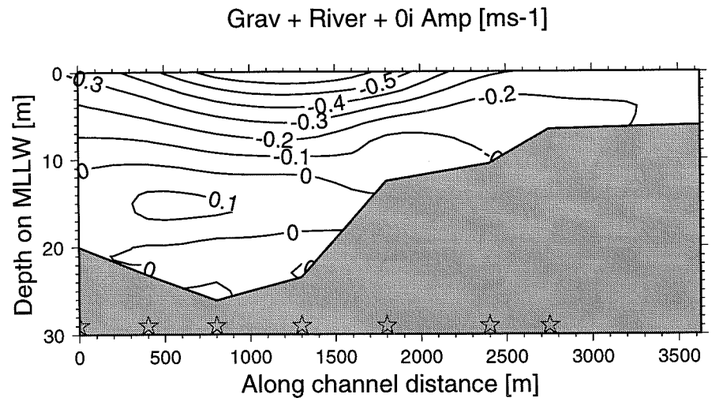


Figure 4.9: Along-channel combined residual circulation in $[m\ s^{-1}]$. Includes river-flow, gravitational and non-linearly generated residual modes.

the total residual are larger than the errors resulting from differencing the data and model results; this tends to lend credence to the results.

The difference between the data and model was calculated at each grid point, every meter in the vertical and every 100 m in the horizontal, see Figure (4.10).

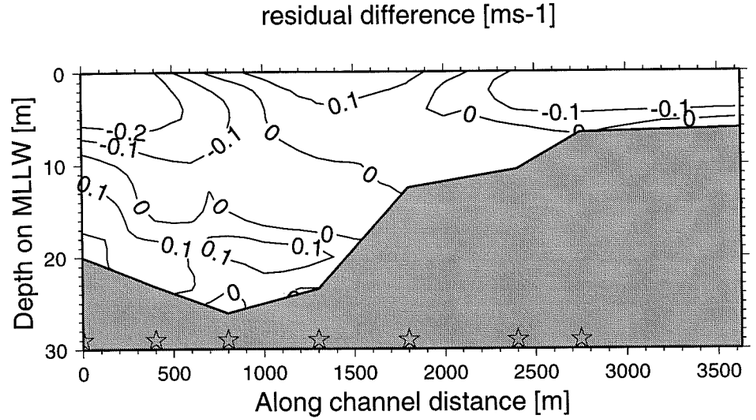


Figure 4.10: Difference of data, Z_0 and modeled, total residual along channel velocity which includes riverflow, gravitational and non-linearly generated residual flow. In $[m\,s^{-1}]$.

The diurnal, Figure (4.11), and the semidiurnal tidal currents, Figure (4.12), are shown for completeness and should be compared to Figures (2.11) and (2.13) respectively.

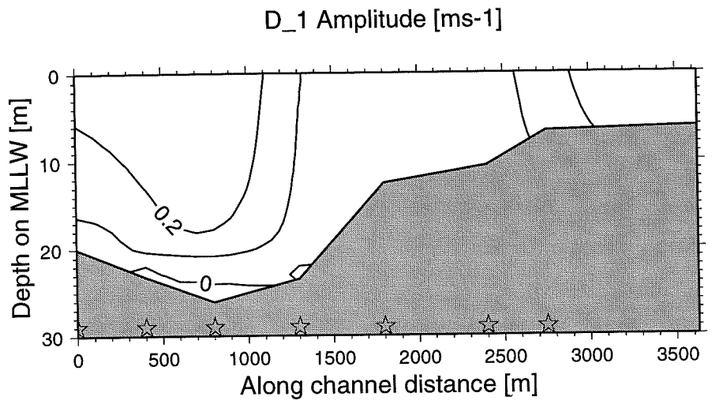


Figure 4.11: Along-channel D_1 band circulation in $[m\ s^{-1}]$.

4.5.2 Comparison to analytical solution

The gravitational circulation for a V-shaped channel calculated with the profile model, Figure (4.14), is compared to the analytic solution, Figure (4.13) from Wong [54]. The two figures are identical.

4.6 Summary

This test, along with the comparisons to data shown earlier, verify this modeling approach. Using the profile model, the solutions are analytically tractable for arbitrary channel cross-section if the eddy diffusivity is vertically constant ($K_m \neq f(z)$), and the density forcing can be integrated three times.

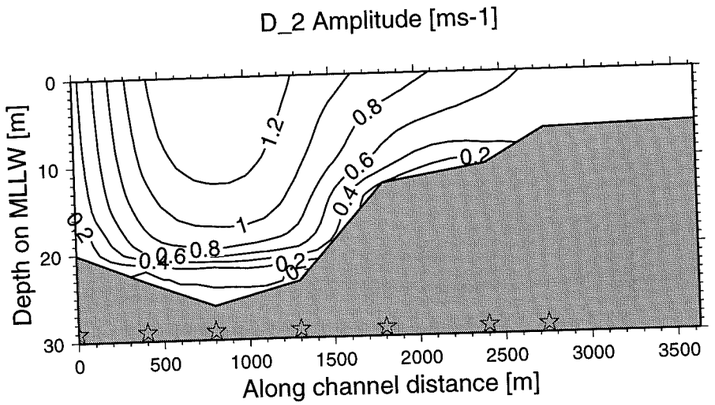


Figure 4.12: Along-channel D_2 band circulation in $[m\ s^{-1}]$.

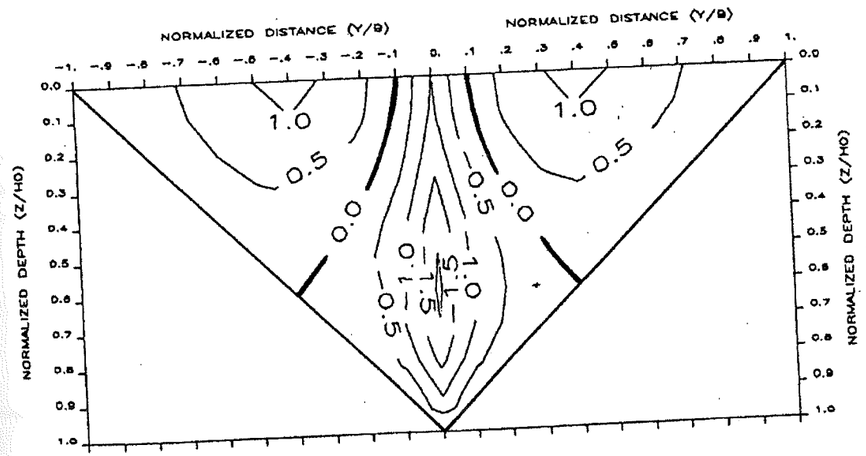


Figure 4.13: From [54] showing the normalized analytic solution for gravitational circulation in a V-shaped channel.

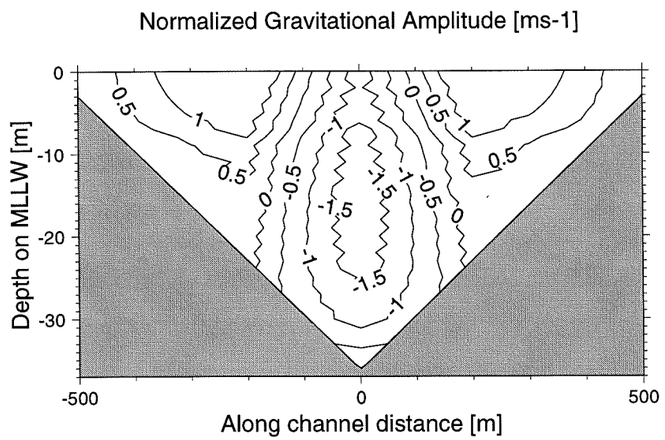


Figure 4.14: Profile model solution for gravitational circulation in a V-shaped channel for comparison to Figure (4.13).

Chapter 5

LATERAL TOPOGRAPHIC EFFECTS ON ALONG-CHANNEL FLOW

To demonstrate how the different flow modes are effected by the topography of an estuary 7 simulations were run. These simulations are intended to illustrate how the presence or absence of tidal flats, channel curvature and variations in depth effect flow in an estuary.

5.1 Simulation Matrix

Table 5.1 shows the configuration of each of the simulations. The second column indicates the shape of the lateral channel bathymetry. The next 3 columns describe the along channel radius of curvature looking up-river: straight, "+" to the left or "-" to the right with a radius of 4 km. The next 2 columns are for presence or absence of tidal flats where the tidal flat widths are expressed in terms of a percentage of the momentum carrying channel width. As an example, if the momentum carrying channel width is $1,000$ m, then the tidal flat width is 20% or 200 m yielding a mean total channel width of $1,200$ m and a high water width of $1,400$ m. The flow dynamics on the tidal flats are not modeled here, they are formulated solely as momentum sinks and mass storage. That is, as a parcel of water, which is flowing upstream on flood, enters the tidal flats as the water height increases with the tide it loses its momentum to the increased friction of the tidal flats and comes to rest. When the tide starts to ebb and the tidal flats are emptied, the parcel of water is re-accelerated as it enters the channel, gaining momentum from the main flow. The next column indicates the

strength of the stratification and the last column indicates if surface shear stress is present in the form of wind forcing.

Table 5.1: Simulation matrix showing the parameters for each run. The tidal flat width is the percentage of the momentum carrying width.

Run	Channel Shape	Radius of Curvature			Tidal Flats		Stratification	Wind
		Straight	+4 km	-4 km	0%	20%		
1	Rectangular	X			X		strong	
2		X				X	strong	
3			X		X		strong	
4	V	X			X		strong	
5	Stepped		X		X		strong	
6				X	X		strong	
7		X			X		weak	X

The simulations were run with the same basic parameters. They all have the same cross-sectional area of $19,575\ m^2$, a riverflow is $3,000\ m^3sec$, and average depths of $19.4\ m$. The channel width (momentum carrying width) is $1,000\ m$ in each case. The strong stratification cases have a mean horizontal density gradient of 13 and the weak cases 3 was used. All of the following lateral sections are looking upstream. Positive values indicate upstream flow while negative values indicate down-stream flow. When curvature is present, the radius of curvature ($\mathcal{K}$) is $4\ km$.

5.2 Rectangular Cross-Section

A rectangular channel is the most basic shape in that there are no lateral depth variations to effect the flow. Lateral variations in the along-channel flow fields will be

strength of the stratification and the last column indicates if surface shear stress is present in the form of wind forcing.

Table 5.1: Simulation matrix showing the parameters for each run. The tidal flat width is the percentage of the momentum carrying width.

Run	Channel Shape	Radius of Curvature			Tidal Flats		Stratification	Wind
		Straight	+4 km	-4 km	0%	20%		
1	Rectangular	X			X		strong	
2		X				X	strong	
3			X		X		strong	
4	V	X			X		strong	
5	Stepped		X		X		strong	
6				X	X		strong	
7		X			X		weak	X

The simulations were run with the same basic parameters. They all have the same cross-sectional area of $19,575\ m^2$, a riverflow is $3,000\ m^3 sec$, and average depths of $19.4\ m$. The channel width (momentum carrying width) is $1,000\ m$ in each case. The strong stratification cases have a mean horizontal density gradient of 13 and the weak cases 3 was used. All of the following lateral sections are looking upstream. Positive values indicate upstream flow while negative values indicate down-stream flow. When curvature is present, the radius of curvature ($\mathcal{K}$) is $4\ km$.

5.2 Rectangular Cross-Section

A rectangular channel is the most basic shape in that there are no lateral depth variations to effect the flow. Lateral variations in the along-channel flow fields will be

investigated for cases including channel curvature and tidal flats.

5.2.1 Straight without Tide Flats: Run #1

Since this is the most basic channel cross-section, subsequent cross-sectional channel geometries will be compared to this case. As expected, the riverflow is down-stream every where in the channel in Figure (5.1). The highest amplitude flow is at the top-center of the channel, farthest from channel bottom and sides. Integration of the velocity over the channel cross-section yields the specified riverflow (q_R) in $m^3 sec$.

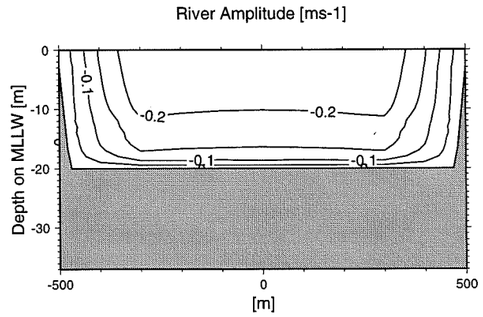


Figure 5.1: River flow [$m\ s^{-1}$] for a straight channel of rectangular cross-section without tidal flats. Looking upstream. Negative values indicate flow down-stream.

For the case of the gravitational (baroclinic) flow Figure (5.2), the denser ocean water moves landward in the bottom center of the channel. The maximum landward flow is above the bed because, friction retards the flow at the bed. The seaward compensating flow of fresh water is concentrated at the top center of the channel. Here, the integrated flow over the cross-section is zero as required by this mode. The non-linearly generated residual flow, shown in Figure (5.3), is driven by the near-bottom shear of the semidiurnal current, Figure (5.6). The compensating return flow

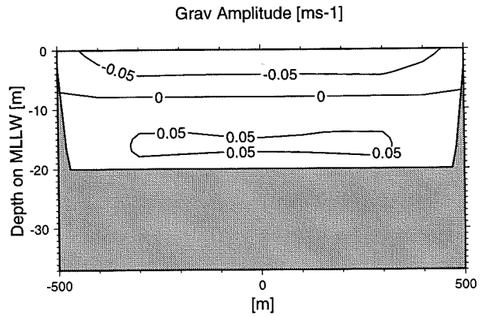


Figure 5.2: Gravitational flow $[m\ s^{-1}]$ for a straight channel of rectangular cross-section without tidal flats. Looking upstream. Negative values indicate flow down-stream, positive upstream.

near the surface is a direct result of conservation of mass. The combined residual

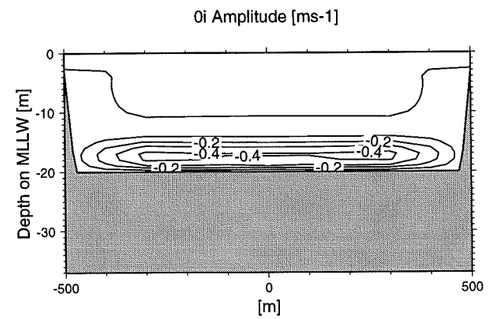


Figure 5.3: Non-linearly generated residual flow $[m\ s^{-1}]$ for a straight channel of rectangular cross-section without tidal flats. Looking upstream. Negative values indicate flow down-stream, positive upstream.

flow, which is the sum of the river, gravitational and non-linearly generated residual flows, in Figure (5.4) illustrates a very basic notion of estuarine circulation: the denser water is flowing upstream near the bottom with a maximum near the middle of this upstream flow and the outflow increases from the top of the inflow layer to the surface.

The amplitudes of the diurnal and semidiurnal band currents, Figures (5.5) and (5.6),

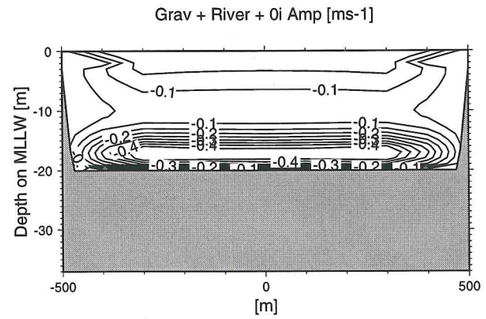


Figure 5.4: Combined residual flow $[m\ s^{-1}]$ for a straight channel of rectangular cross-section without tidal flats. Looking upstream. Negative values indicate flow down-stream, positive upstream.

show the same basic pattern as the riverflow case. This occurs because the tidal flow is quite strongly effected by friction, so the dominant force balance is between friction and surface slope.

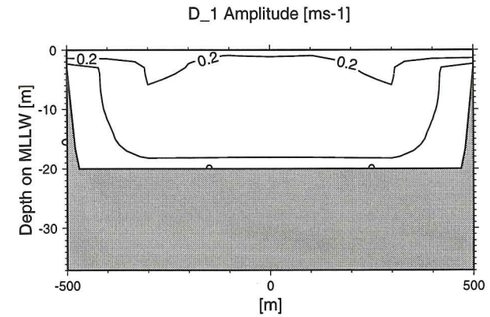


Figure 5.5: Amplitude of the diurnal band tidally driven flow $[m\ s^{-1}]$ for a straight channel of rectangular cross-section without tidal flats. Looking upstream.

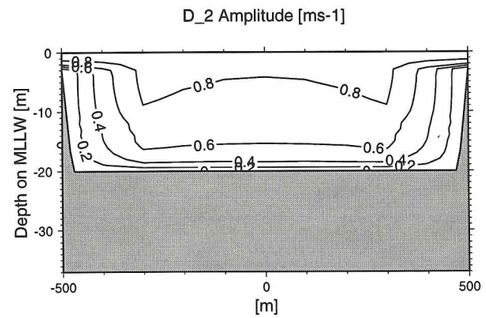


Figure 5.6: Amplitude of semidiurnal band tidally driven flow $[m\ s^{-1}]$ for a straight channel of rectangular cross-section without tidal flats. Looking upstream.

5.2.2 Straight with tidal flats: Run #2

The inclusion of tidal flats has some important consequences. In the case of riverflow (not shown), the effect is a small intensification of the flow at the surface, concentrated at the edges of the top center portion of the channel. For the case of the gravitational (baroclinic) flow, Figure (5.7), the presence of tidal flats intensifies the flow in both layers in the distorted coordinates. The outward flowing contours are slightly lower in the water column than for the case without tidal flats, Figure (5.1). The stagnation contour is in the same place and the in-flowing contours are slightly intensified to balance the increased outflow. This intensification factor comes directly from the x^*-coordinate distortion, $\sqrt{\frac{b_T}{b}} = \sqrt{1.2} = 1.095$, and is not present in the undistorted coordinates.

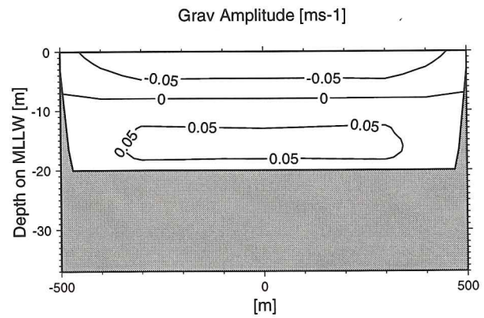


Figure 5.7: Gravitational flow $[m\ s^{-1}]$ for a straight channel of rectangular cross-section with tidal flats. Looking upstream. Negative values indicate flow downstream, positive upstream.

Non-linearly generated residual flow, Figure (5.8), varies with the square of the D_2 flow and is therefore moderated from Figure (5.3) because the semidiurnal current is also reduced by the presents of tidal flats. Combined residual flow includes river, gravitational and non-linearly generated residual flows, Figure (5.9), mainly reflects the moderation in the non-linear residual mode.

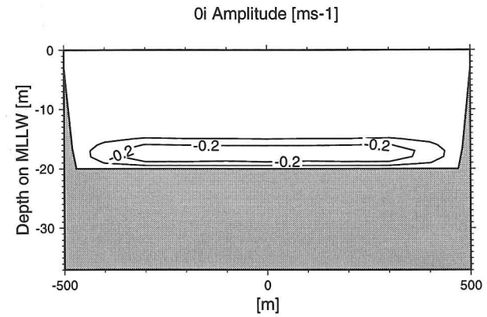


Figure 5.8: Non-linearly generated residual flow [$m\ s^{-1}$] for a straight channel of rectangular cross-section with tidal flats. Looking upstream. Negative values indicate flow down-stream, positive upstream.

The flow for the tidally driven flow in the diurnal and the semidiurnal bands both show a slight decrease in current amplitude; the semidiurnal flow is more strongly effected and is shown in Figure (5.10). The 0.6 $m\ s^{-1}$ contour is higher in the water column while the 0.4 $m\ s^{-1}$ contour doesn't move. This local decrease in shear directly influences the non-linear residual profile and is caused by the augmentation of the convective acceleration term ($U_1\ \frac{\partial U_R}{\partial x}$) by the ratio $\frac{b_T}{b}$.

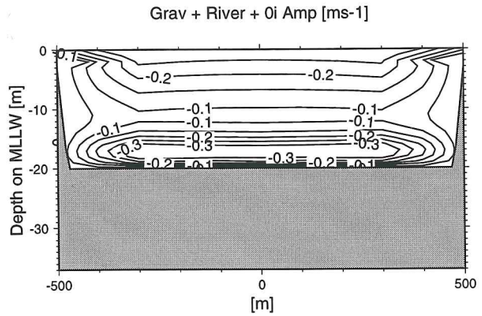


Figure 5.9: Combined residual flow $[m\ s^{-1}]$ for a straight channel of rectangular cross-section with tidal flats. Looking upstream. Negative values indicate flow downstream, positive upstream.

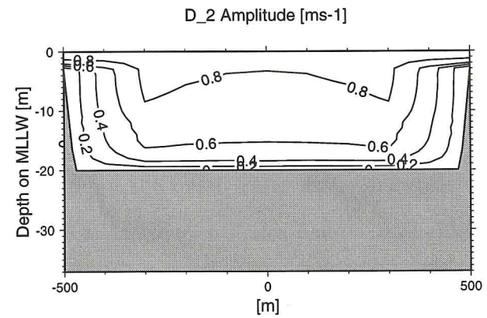


Figure 5.10: Amplitude semidiurnal band tidally driven flow $[m\ s^{-1}]$ for a straight channel of rectangular cross-section with tidal flats. Looking upstream.

8/8c/5

5.2.3 *Channel Curvature without Tide Flats: Run #3*

For the case of a rectangular channel cross-section without tidal flats but a channel curvature, $\mathcal{K} = 4$ km to the left looking upstream, River flow Figure (5.11), semidiurnal band tidally driven flow Figure (5.12) and the tidally driven diurnal band, the areas of fastest currents are moved towards the outside of the bend without modifying the intensity of the flow. Non-linerally generated residual flow Figure (5.13).

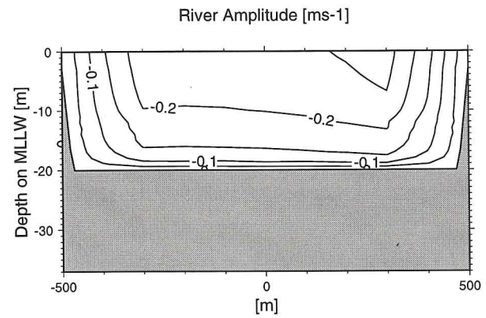


Figure 5.11: River flow $[m\ s^{-1}]$ for a channel of rectangular cross-section with $\mathcal{K} = 4$ km and without tidal flats. Looking upstream. Negative values indicate flow downstream.

Gravitationally driven flow shown in Figure (5.14) dramatically shows the effect curvature can have on the flow. The denser landward flow is significantly intensified and concentrated on the outside of the bend while the seaward flow is also slightly intensified and is concentrated at the inside if the bend. In this case the denser bottom water, which is flowing upstream, is concentrated at the outside of the bend, forcing less dense surface return flow to concentrate at the inside of the bend. The combined residual flow, Figure (5.15), shows the effect of channel curvature more in the upper layer than in the lower layer. The bottom inflow is the same basic amplitude as the straight case except that the outer lobe is slightly enlarged and the inner decreased. The maximum surface outflow, however, is slightly increased but more noteworthy is

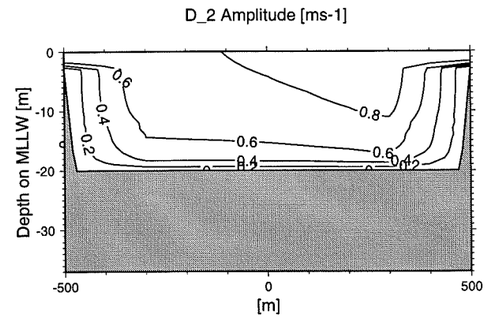


Figure 5.12: Amplitude of semidiurnal band tidally driven flow $[m\ s^{-1}]$ for a channel of rectangular cross-section with $\mathcal{K} = 4$ km and without tidal flats. Looking upstream.

that the area of most intense outflow is located at the inside of the bend.

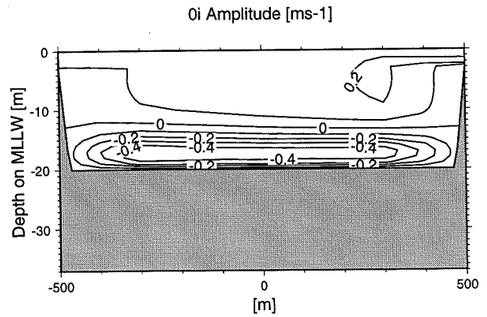


Figure 5.13: Non-linerally generated residual flow $[m\ s^{-1}]$ for a channel of rectangular cross-section with $\mathcal{K} = 4$ km and without tidal flats. Looking upstream. Negative values indicate flow down-stream, positive upstream.

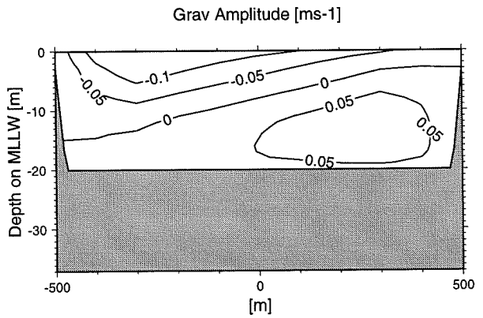


Figure 5.14: Gravitationally driven flow $[m\ s^{-1}]$ for a channel of rectangular cross-section with $\mathcal{K} = 4$ km and without tidal flats. Looking upstream. Negative values indicate flow down-stream, positive upstream.

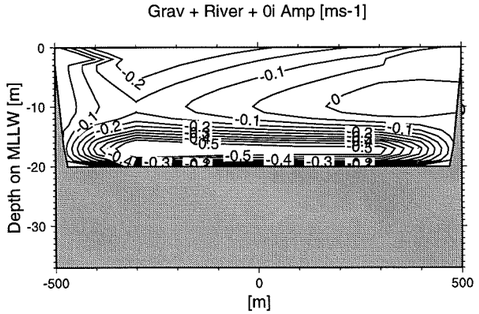


Figure 5.15: Combined residual flow $[m\ s^{-1}]$ for a channel of rectangular cross-section with $\mathcal{K} = 4$ km and without tidal flats. Looking upstream. Negative values indicate flow down-stream, positive upstream.

5.3 V-Shaped Channel Cross-Section

5.3.1 V-Shaped Straight without Tide Flats: Run #4

To demonstrate the effect that variations in bottom depth has on the different flow modes I'll now increase the topographic complexity by modeling flow in a straight "V"-shaped channel without tidal flats. As expected, the riverflow, Figure (5.16), is concentrated over the deepest part of the channel where drag is a minimum, decreasing to the sides as the channel shoals. In the gravitationally driven case, Figure (5.17),

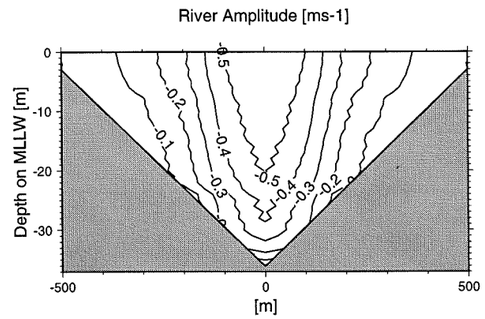


Figure 5.16: River flow $[m\ s^{-1}]$ for a straight "V"-shaped channel without tidal flats. Looking upstream. Negative values indicate flow down-stream.

the denser upstream flow is concentrated in the deepest part of the channel and the fresher return flow is forced towards the banks, but the greatest return flow is over the deepest remaining area of the channel. The flow field in this case is very similar to Wong's Figure (8b) even though he neglected the effects of a vertically variable eddy viscosity. The combined residual flow is shown in Figure (5.18) and exhibits the same characteristics as the gravitational flow case. The flow for the diurnal tidally driven case (not shown) has the same appearance as the semidiurnal tidally driven mode shown in Figure (5.19).

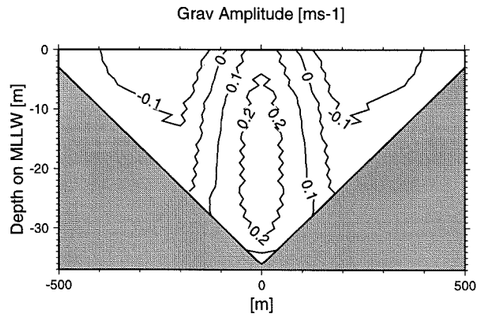


Figure 5.17: Gravitationally driven flow $[m\ s^{-1}]$ for a straight "V"-shaped channel without tidal flats. Looking upstream. Negative values indicate flow down-stream, positive upstream.

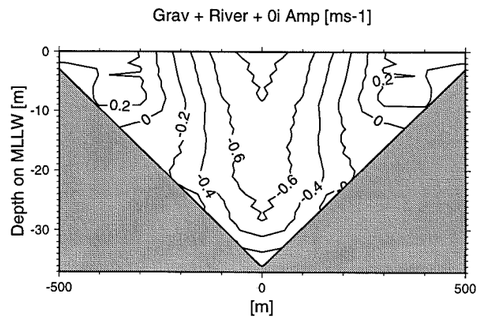


Figure 5.18: Combined residual flow $[m\ s^{-1}]$ for a straight "V"-shaped channel without tidal flats. Looking upstream. Negative values indicate flow down-stream, positive upstream.

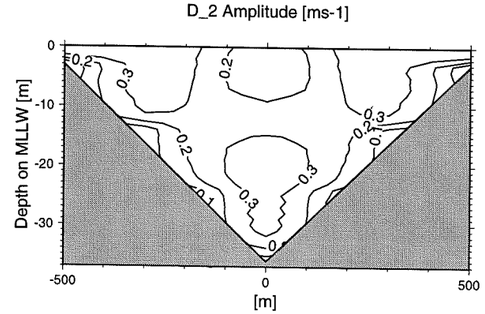


Figure 5.19: Amplitude of semidiurnal tidally driven flow $[m\ s^{-1}]$ for a straight "V"-shaped channel without tidal flats. Looking upstream.

5.4 *Irregularly Shaped Channel Cross-Section*

Turning now to a still more realistic channel configuration, the combined effects of channel curvature and variations in depth, which may interact constructively or destructively, are illustrated with an irregularly shaped channel cross-section. This configuration is similar to the dredged channels often observed in estuaries. The flow patterns of straight, although irregular, channel can be deduced from the previous examples and, therefore, will not be presented here. The two cases which will be investigated are those of the channel curving to the left and to the right.

5.4.1 Curved to Left: Run #5

In this case, the channel curves to the left with a radius of curvature of 4 km and there are no tide flats here. The riverflow, Figure (5.20), shows the area of faster outflow to be concentrated over the deeper half of the channel with a slight intensification along the outer edge of the channel (on the right side of the figure). The gravitationally

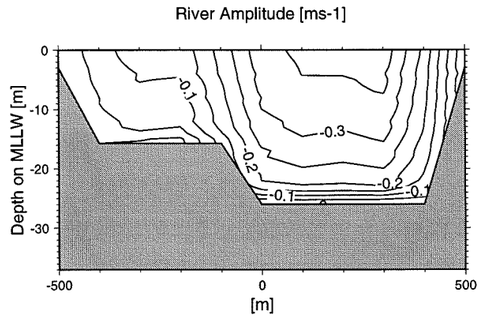


Figure 5.20: River flow $[m\ s^{-1}]$ for an irregular channel with $\mathcal{K} = 4$ km and without tidal flats. Looking upstream. Negative values indicate flow down-stream.

driven flow, Figure (5.21), exhibits some interesting behavior. The landward flow is only in the deepest half of the channel with a mid-depth velocity maximum. Here

the effects of the channel curving to the left and the deepest section of the channel being on the right act in concert to accentuate the seaward flow. The inflow extends to the surface for approximately 25% of the channel width along the outer edge. The compensating outflow is concentrated in the shallower section of the channel with a very slight displacement towards the outside of the channel.

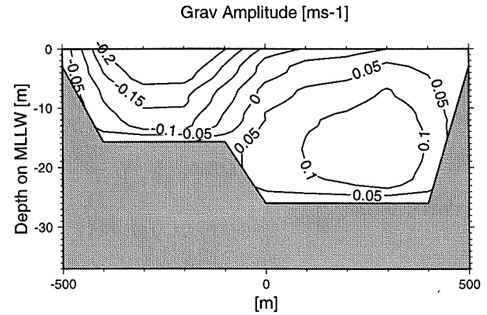


Figure 5.21: Gravitationally driven flow $[m\ s^{-1}]$ for an irregular channel with $\mathcal{K} =$ 4 km and without tidal flats. Looking upstream. Negative values indicate flow downstream, positive upstream.

The combined residual flow shown in Figure (5.22) has outflow over the entire channel being much stronger on the inside of the bend, over the shallower section of the channel, while the inflow occurs solely in the deeper side of the channel with a velocity maxima near the bottom. The semidiurnal tidally driven flow amplitude, Figure (5.23), shows a fairly uniform velocity distribution. The diurnal tidally driven flow amplitude again has the same form.

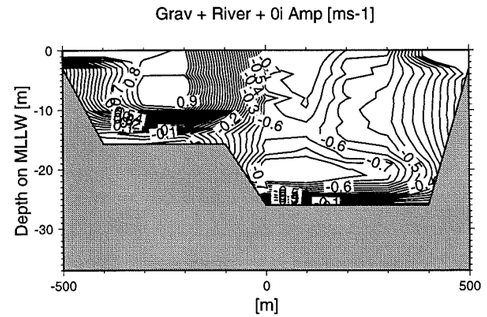


Figure 5.22: Combined residual flow $[m\ s^{-1}]$ for an irregular channel with $\mathcal{K} = 4$ km and without tidal flats. Looking upstream. Negative values indicate flow downstream, positive upstream.

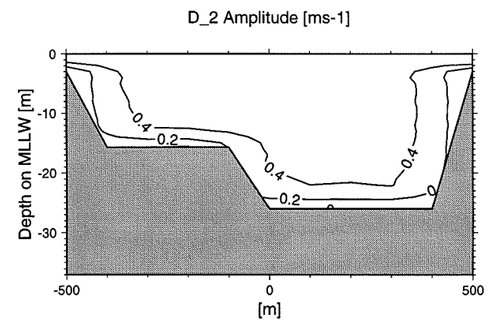


Figure 5.23: Amplitude of semidiurnal tidally driven flow $[m\ s^{-1}]$ for an irregular channel with $\mathcal{K} = 4$ km and without tidal flats. Looking upstream.

5.4.2 Curved to Right: Run #6

The case of an irregularly shaped channel which curves to the right when looking upstream behaves like the other cases with channel curvature: the flow is concentrated on the outside of the bend, the left side of the channel in this case. Only the results for the combined residual flow are shown here, as the other modes do not provide any significantly new information. The combined residual flow, Figure (5.24), shows the bottom inflow in the deepest section of the channel, but slightly intensified on the left side. This intensification is responsible for decrease in the surface velocities over the left side of the deeper channel. Combined residual flow Figure (5.24). In this case the

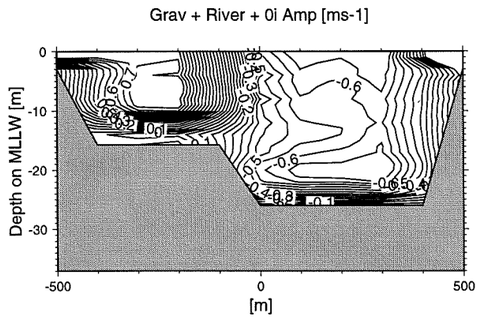


Figure 5.24: Combined residual flow $[m\ s^{-1}]$ for an irregular channel with $\mathcal{K} = -4$ km and without tidal flats. Looking upstream. Negative values indicate flow downstream, positive upstream.

channel curvature and depth variation oppose each other. The combined effect is to more evenly distribute the seaward surface across the channel and the seaward inflow across the deepest section of the channel.

5.4.3 Straight channel, weak stratification with wind

This section discusses the effects of wind driven circulation and weak stratification has on the residual circulation patterns in a irregularly shaped channel. As previously

stated, residual circulation generated by surface wind stress has the ability to influence the total residual circulation as well as the density structure of an estuary. Figure (5.25) shows the baroclinic circulation pattern for weak density forcing, approximately 25% of that in the previous cases. The circulation pattern is the same earlier cases, but the amplitude is reduced. The figure of the wind driven circulation, (5.26), shows

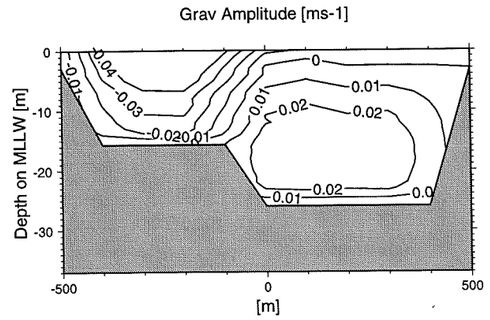


Figure 5.25: Baroclinic circulation $[m\ s^{-1}]$ for a straight irregular channel, with wind forcing, with weak density forcing and without tidal flats. Looking upstream. Negative values indicate flow down-stream, positive upstream.

the flow generated by a surface shear stress of 1.1 $N\ m^2$, up-stream (into the page).

Combined residual circulation Figure (5.27).

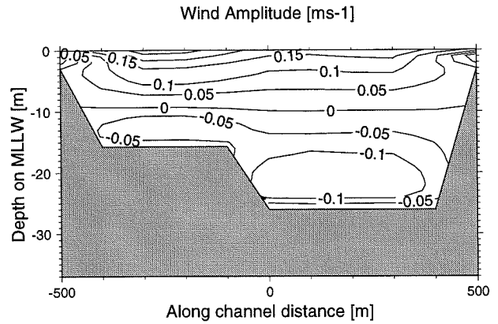


Figure 5.26: Wind driven circulation $[m\ s^{-1}]$ for a straight irregular channel, with wind forcing, with weak density forcing and without tidal flats. Looking upstream. Negative values indicate flow down-stream, positive upstream.

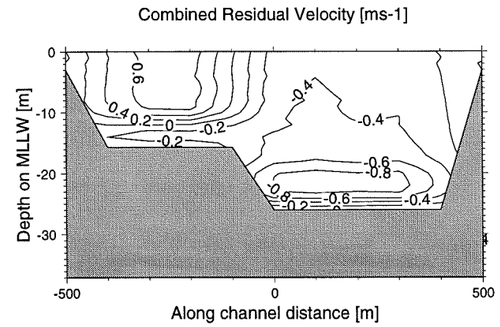


Figure 5.27: Combined residual circulation $[m\ s^{-1}]$ which includes riverflow, baroclinic flow, non-linearly generated residual and wind driven circulation. For a straight irregular channel, with wind forcing, with weak density forcing and without tidal flats. Looking upstream. Negative values indicate flow down-stream, positive upstream.

Chapter 6

SUMMARY

The objective of this dissertation is to give insight into the three-dimensional (3-D) circulation dynamics of stratified estuaries that are strongly forced by both oceanic tides and riverflow. Knowledge of the along-channel circulation dynamics in estuaries is important because it is the along-channel flow which is primarily responsible for the transport of material in an estuary. The material being transported may include: 1) deutrital matter; 2) salt; 3) man made pollutants entering the estuary from anywhere in the watershed; 4) sediment that has the ability to alter the topography of an estuary which, in turn, would alter the circulation; or, 5) micro- or macro-organisms which are important members of the estuarine food web, processing nutrients and deutrital material in the estuary and supplying food for larger members of the food web that are of interest to man. To accomplish this goal, a new class of 3-D model is presented to fill a niche between purely analytical and fully 3-D numerical models.

This new model calculates along-channel velocities for strongly forced "narrow" estuarine systems and may be described as:

1. Mode-splitting in that the 1-D barotropic tidal long-wave propagation in the estuary is calculated first and then velocity profiles are calculated for each mode separately. The profile model encompasses the major circulation processes in narrow estuaries: tidal circulation, overtide and residual flow non-linearly generated by internal tidal asymmetry, riverflow, wind driven and baroclinic circulation. The model could be extended to include Stokes drift compensation and tidal non-linear residual flows;

2. Quasi 3-D, referring to the fact that lateral forcing is not considered;

3. Using sectional geometry where within a section of the estuary the channel width, total width (including tidal flats) and depth are allowed to independently vary or remain constant, the same topography is used in the 1-D and 3-D models;

4. Harmonic because the multiple tidal species are considered independently;

5. Employing a separation of variables for the velocity as a function of along-channel distance, a function of lateral distance and depth and a function of time: $U(x, y, z, t) = \mathcal{R}e[F(x)\ G(y, z)\ e^{-2ni\omega t}]$ where $n = 0, 1, 2, ...$ for the residual flow, tidal and overtide flows.

6. Cast in σ-coordinates where the vertical coordinate is scaled by the local depth. This causes the bottom to be at $\sigma = 0$ and the surface of the water to be at $\sigma = 1$. The very different depth dependences of the various flow modes are rendered explicit by using a σ-coordinate system.

This model can also incorporate realistic channel bathymetry, use any physically realistic density forcing function, treat vertical mixing more realistically than can be done in purely analytical models, does not mask the physics involved in the flow and is less computationally intensive than fully 3-D numerical models.

The primary hypothesis of this dissertation is that most of the 3-D variability in the along-channel circulation in a strongly forced estuary can be accounted for by including the lateral variations in density and bathymetry but neglecting the effects of secondary, lateral, flow; the model results suggest that this idea is correct. This new model incorporates this simplification and the modeling ideas put forth by others with new modeling techniques and new ideas on estuarine circulation. The model allows for the presence of tidal flats as long as the estuary and its tidal flats can be considered narrow. Surface forcing (e.g. wind stress), if present, is taken to be laterally uniform,

while internal forcing is taken to be to be a function of depth. Validation of the model has been accomplished with velocity and density data collected in the Columbia River estuary (CRE) and comparison to analytical results. Analysis of flows in artificial, but typical, channels elucidate important features of estuarine residual circulation; e.g.: 1) how stratification, channel curvature and density forcing interact to determine the position of upstream bottom flow in a channel; 2) how variations in horizontal density gradient effect the flow, and 3) how tides, stratification and topography interact to create residual flow through internal tidal asymmetry.

The lateral distribution of gravitational circulation in a cross-section is strongly affected by the lateral distribution of bottom depth and the lateral and vertical distribution of along-channel density gradient; stratification at mid-depth increases the concentration of flow in mid-channel. The strength of the gravitational circulation is modulated by vertical mixing and the strength of horizontal density forcing and bed-slope. Gravitational circulation is affected in at least three respects by a landward decrease in bottom depth. First, the rise in isopycnals over a topographic high causes a local decrease and possibly reversal of the along-channel density forcing as shown in Chapter 2 Figures (2.10, 2.12, 2.14, 2.16). Secondly, the reversal of bed-slope acts directly through stratification/bed-slope interaction term, see Equation (38), that appears explicitly in the σ-coordinate representation of baroclinic forcing. Lastly, a topographic high can also cause a local increase in vertical mixing by increasing vertical shear this may also be seen in Chapter 2, Figures (2.9, 2.11, 2.13, 2.15).

The lateral distribution of river outflow as well as wind driven circulation is effected by lateral variations in depth through friction, but less strongly so than gravitational circulation. The vertical distribution of outflow is affected primarily by stratification effects on vertical mixing. The sensitivity of these and other residual flow modes to variations in the representation of vertical mixing demonstrates the need for the development of turbulence models that better represent the physics of internal mixing and interactions between turbulence, vertical shear and internal waves over topography.

Non-linearly generated residual follows the vertical shear of the semidiurnal circulation, it's primary driving force along with the tidally varying eddy diffusivity field. This mode can become significant, the residual mode rivaling the amplitudes of either the riverflow or the baroclinic circulation. In these systems, a time-varying density field leads to unsteady tidal flow, which in turn feeds back onto the density field through tidal straining.

There are several ways to improve upon and extend this work. Many improvements will be due to improved equipment. For example, new broad-band ADCP technology may be used to attain better horizontal and vertical velocity resolution. While using an ADCP with a 20° beam angle instead of 30° will allow confident measurement of velocities closer to the bed. Some improvements will come about by combining data from multiple instruments: Using multiple ship mounted ADCP's will give a more synoptic picture of estuary. Current meter moorings used in conjunction with multiple ships equipped ADCP's will improve the synopticity of measurements. Incorporating data measured very near the bed with instruments like acoustic Doppler velocimeter (ADV) data with ADCP data would also improve bed stress parameterization. Still other improvements will come about from better computer techniques: Developing a method to relate data collected at different times to be reduced to a single time base will give a synoptic picture of the estuary from non-synoptic data. Or, by using wavelet analysis instead of harmonic analysis, the non-stationary nature of the data will be correctly accounted for. The model would also benefit from verification in other systems where the dominant physical processes may be different from those in the CRE. And, of course, the lateral force balance should be included for the model to be completely proper.

This study has presented a new tool for gaining a better understanding of the physical processes occurring in strongly forced estuarine systems. With some basic knowledge of a new system (topography, density field and tidal and river forcing) valuable insight may be obtained as to the importance of the various flow modes

present and thus an understanding of the transport of material in the estuary. This work has also shown that most of the lateral variation in along-channel flow can be accounted for by including the lateral variations in density and bathymetry while simplifying the mathematics by neglecting the secondary, or lateral, flow.

BIBLIOGRAPHY

[1] W. M. Cameron and D. W. Pritchard. Estuaries. In N. M. Hill, editor, *The Sea*, pages 306–324, New York, 1963. John Wiley.

[2] B. C. Crump, J. A. Baross, and C. A. Simenstad. Dominance of particle-attached bacteria in the columbia river estuary. *Aquat. Microb. Ecol.*, 14:7–18, 1997.

[3] J. J. Dronkers. *Tidal Computations in Rivers and Coastal Waters.* North-Holland, Amsterdam, 1964. pp. 219-304.

[4] K. R. Dyer. *Estuaries: a Physical Introduction.* John Wiley, New York, 1973. 140 pp.

[5] H. B. Fischer. Mass transport mechanisms in partially stratified estuaries. *Journal of Fluid Mechanics*, 53(4):671–687, 1972.

[6] H. B. Fischer. Mixing and dispersion in estuaries. *Annual Review of Fluid Mechanics*, 8:107–133, 1976.

[7] C. T. Friedrichs and D. G. Aubrey. Tidal propagation in strongly convergent channels. *Journal of Geophysical Research*, 99(C2):3,321–3,336, Feb. 15, 1994.

[8] C. T. Friedrichs and O. S. Madsen. Nonlinear diffusion of the tidal signal in frictionally dominated embayments. *Journal of Geophysical Research*, 97(C4):5,637–5650, 1993.

[9] W. R. Geyer. *The Time dependent Dynamics of a Salt Wedge.* PhD thesis, University of Washington, 1985.

[10] W. R. Geyer. Three-dimensional tidal flow around headlands. *Journal of Geophysical Research*, 98(C1):955–966, January 15, 1993.

[11] W. R. Geyer and R. Signell. Measurements of tidal flow around a headland with a shipboard acoustic doppler current profiler. *Journal of Geophysical Research*, 99(C3):3,189–3,197, March 15, 1990.

[12] B. S. Giese and D. A. Jay. Modeling tidal energetics of the columbia river estuary. *Estuarine, Coastal and Shelf Science*, 29:549–571, 1989.

[13] A. E. Gill. *Atmosphere-Ocean Dynamics.* Academic Press, Inc., San Diego, 1982. 207 pp.

[14] G. Godin and G. Gutierrez. Non-linear effects on the tide of the bay of fundy. *Continental Shelf Research*, 29:379–402, 1986.

[15] P. Hamilton and M. Rattray Jr. *Estuarine Transport Processes*, chapter Theoretical Aspects of Estuarine Circulation, pages 37–74. University of South Carolina Press, Columbia, 1978.

[16] D. V. Hansen and M. Rattray Jr. Gravitational circulation in straits and estuaries. *Journal of Marine Research*, 23:104–122, 1965.

[17] D. V. Hansen and M. Rattray Jr. New dimensions in estuary classification. *Limnology and Oceanography*, XI(3):319–326, 1966.

[18] J. P. Ianniello. *Non-Linearly Induced Residual Currents in Tidally Dominated Estuaries.* PhD thesis, The University of Connecticut, 1977.

[19] J. P. Ianniello. Tidally induced residual currents in estuaries of constant breadth and depth. *Journal of Marine Research*, 35(4):755–786, 1977.

[20] J. P. Ianniello. Tidally induced residual currents in estuaries of variable breadth and depth. *Journal of Physical Oceanography*, 9:962–974, 1979.

[21] J. P. Ianniello. Comments on tidally induced residual currents in estuaries: Dynamics and near-bottom flow characteristics. *Journal of Physical Oceanography*, 11:126–134, 1981.

[22] D. A. Jay. Two-dimensional forcing of stratified estuarine circulation, over three-dimensional topography: I. tidal flow modes, in preparation.

[23] D. A. Jay. Circulatory processes in the columbia river estuary. Technical report, CREST/Geophysics, 1984.

[24] D. A. Jay. *Residual Circulation in Shallow Stratified Estuaries.* PhD thesis, University of Washington, 1987.

[25] D. A. Jay. Estuarine salt conservation: a lagrangian approach. *Estuarine, Coastal and Shelf Science*, 32:547–565, 1991.

[26] D. A. Jay. Internal asymmetry and anharmonicity in estuarine flows. In B. B. Parker, editor, *Progress in Tidal Hydrodynamics*, pages 521–543, New York, 1991. John Wiley.

[27] D. A. Jay. Green's law revisited: Tidal long-wave propagation in channels with strong topography. *Journal of Geophysical Research*, 96(C11):20,585–20,598, November 15, 1991.

[28] D. A. Jay and E. P. Flinchem. A comparison of methods for analysis of tidal records containing multi-scale non-tidal background energy. *Continental Shelf Science*, in press.

[29] D. A. Jay and J. D. Musiak. Internal tidal asymmetry in channel flows: Origins and consequences. In C. Pattiaratchi, editor, *Mixing Processes in Estuaries and Coastal Seas, an AGU Coastal and Estuarine Sciences Monograph*, pages 219–258, Washington, D.C., 1996. AGU.

[30] D. A. Jay and J. D. Musiak. Particle trapping in estuarine tidal flows. *Journal of Geophysical Research*, 99(C10):20,445–20,461, October 15, 1994.

[31] D. A. Jay and J. D. Smith. Circulation in and classification of shallow, stratified estuaries. In J. J. Dronkers and W. van Leussen (Eds.), editors, *Physical Processes in Estuaries*, pages 19–41, Heidlberg, 1988. Springer-Verlag.

[32] D. A. Jay and J. D. Smith. Residual circulation in shallow, stratified estuaries i: Highly stratified estuaries. *Journal of Geophysical Research*, 95:711–731, 1990.

[33] D. A. Jay and J. D. Smith. Residual circulation in shallow, stratified estuaries ii: Weakly stratified and partially mixed estuaries. *Journal of Geophysical Research*, 95:733–748, 1990.

[34] B. Kjerfve. *Hydrodynamics of Estuaries*, volume I: Estuarine Physics. CRC Press, Boca Raton, 1988.

[35] P. H. LeBlond. On tidal propagation in shallow rivers. *Journal of Geophysical Research*, 83:4717–4721, 1978.

[36] M. S. Longuet-Higgins. On the transport of mass by time-varying ocean currents. *Deep Sea Research*, 16:431–447, 1969.

[37] C. A. Morgan, J. R. Cordell, and C. A. Simenstad. Sink or swim? copepod population maintenance in the columbia river estuarine turbidity-maxima region. *Marine Biology*, 129:309–317, 1997.

[38] V. T. Neal. Physical aspects of the columbia river and its estuary. In A. T. Pruter and D. L. Avlerson, editors, *The Columbia River Estuary and Adjacent Ocean Waters: Bioenvironmental studies*, pages 19–40, Seattle, 1972. University of Washington Press.

[39] J. C. J. Nihoul and F. C. Ronday. The influence of tidal stress on the residual circulation. *Tellus*, 27:484–489, 1975.

[40] L. Y. Oey. On steady salinity distribution and circulation in partially mixed and well mixed estuaries. *J of Physical Oceanography*, 14:629–645, 1984.

[41] C. B Officer. *Physical Oceanography of Estuaries (and associated Coastal Waters)*. John Whiley, New York, 1976.

[42] B. B. Parker. The relative importance of the various nonlinear mechanisms in a wide range of tidal interactions. In B. B. Parker, editor, *Progress in Tidal Hydrodynamics*, pages 237–268, New York, 1991. John Wiley.

[43] D. Prandle and M. Rahman. Tidal response in estuaries. *Journal of Physical Oceanography*, 10:1552–1573, 1980.

[44] D. W. Pritchard. Salinity distribution and circulation in the chesapeake estuarine system. *Journal of Marine Research*, 11:106–123, 1952.

[45] D. W. Pritchard. A study of the salt balance in a coastal plain estuary. *Journal of Marine Research*, 13:133–144, 1954.

[46] D. W. Pritchard. The dynamic structure of a coastal plain estuary. *Journal of Marine Research*, 15:33–42, 1956.

[47] D. W. Pritchard. The equations of mass continuity and salt continuity in an estuary. *Journal of Marine Research*, 17:412–423, 1958.

[48] D. W. Pritchard and R. E. Kent. A method for determing mean longitudinal velocities in a coastal plain estuary. *Journal of Marine Research*, 15:81–91, 1956.

[49] M. Rattray Jr. and R. J. Uncles. On the predictability of the ^{137}cs distribution in the severn estuary. *Estuarine, Coastal and Shelf Science*, 16(5):475–487, 1983.

[50] C. A. Simenstad, D. A. Jay, J. A. Barros, L. F. Small, F. G. Prahl, D. J. Reed, L. J. Bledsoe, and A. Baptista. Lmer research in the columbia river estuary: The role of estuarine turbidity maxima (etm) processes coupling watershed, estuary and ocean. *NSF*, 1994.

[51] J. D. Smith and S. R. McLean. A model for flow in meandering streams. *Water Resources Research*, 20(9):1,301–1,315, 1984.

[52] P. E. Speer and D. G. Aubrey. A study of non-linear tidal propagation in shallow inlet/estuarine systems part ii: Theory. *Estuarine, Coastal and Shelf Science*, 21:206–240, 1984.

[53] R. J. Uncles and M. B. Jordan. Residual fluxes of water and salt at two stations in the severn estuary. *Estuarine and Coastal Marine Science*, 9:287–302, 1978.

[54] K. C. Wong. On the nature of transverse variability in a coastal plain estuary. *Journal of Geophysical Research*, 99(C7):14,209–14,222, July 15, 1994.

[55] J. T. F. Zimmerman. Mixing and flushing of tidal embayments in the western dutch wadden sea part i: Distribution of salinity and calculation of mixing time scales. *Netherlands Journal of Sea Research*, 10(2):149–191, 1976.

[56] J. T. F. Zimmerman. Dispersion by tide-induced residual current vorticies. In J. C. J. Nihoul, editor, *Hydrodynamics of Estuaries and Fjords*, pages 207–216, 1978.

Appendix A

CRUISE INFORMATION

Tells all about the cruises and the great fun we all had

- 1990

  Dates: 17 Sept - 22 October.
  Ship: R/V Snow goose
  Where: Mouth to Beaver, Rkm 0 - Rkm 85
  Runoff: 3,845 $m^3 s^{-1}$ average

- 1991

  Dates: 2 July - 2 August.
  Ship: R/V Barnes
  Where: Jetty-A to Beaver, Rkm 0 - Rkm 85
  Runoff: 6,874 $m^3 s^{-1}$ average

- 1992

  Dates: 17 May - 20 June.
  Ship: R/V Snow goose
  Where: Mouth to Dalles pool, Rkm 0-Rkm
  Runoff: 6,570 $m^3 s^{-1}$ average

Appendix B

DENSITY AND VELOCITY DATA FROM SOUTH CHANNEL

This section presents the velocity and density data collected in the south channel of the Columbia River estuary during the time period 19 - 25 May 1992.

B.1 Time series

This section presents the raw velocity and density data collected in the south channel of the Columbia River estuary during the time period 19 - 25 May 1992 plotted as time series colormaps. The surface of the water can be seen moving up and down with the tide. The bottom is shown as solid gray. The station locations are shown in Figure (2.1). For each station a time series plot of the total gradient Richardson number is also presented.

B.1.1 Port of Astoria Station

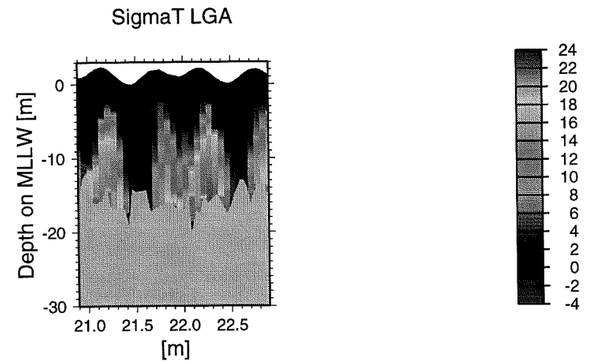


Figure B.1: Time series of density expressed as σ_T for Port of Astoria. See Figure (2.1).

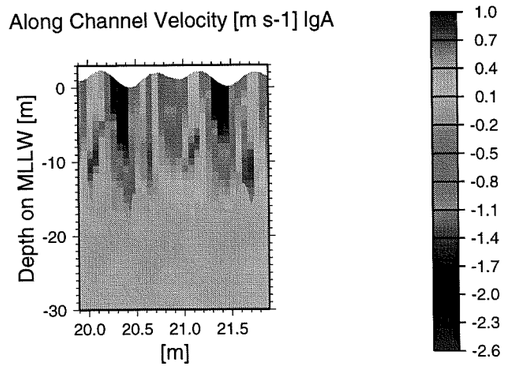


Figure B.2: Time series of along-channel velocity for Port of Astoria. See Figure (2.1).

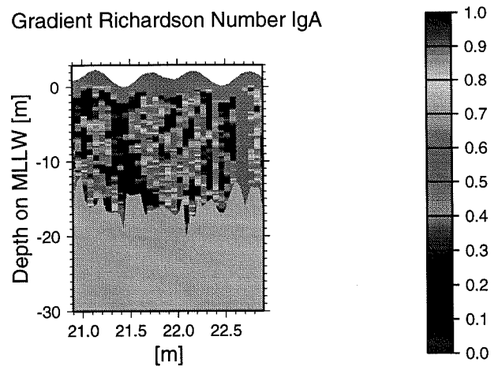


Figure B.3: Time series of gradient Richardson number for Port of Astoria. See Figure (2.1).

B.1.2 Buoy 35a station

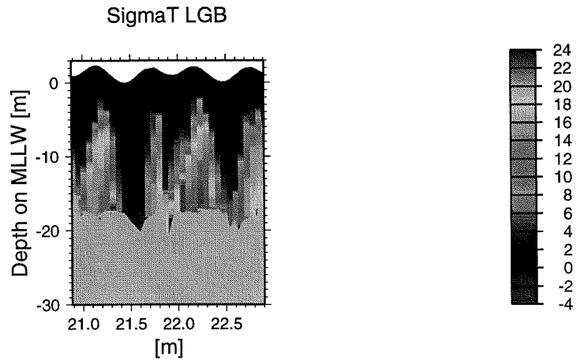


Figure B.4: Time series of density expressed as σ_T for G35a. See Figure (2.1).

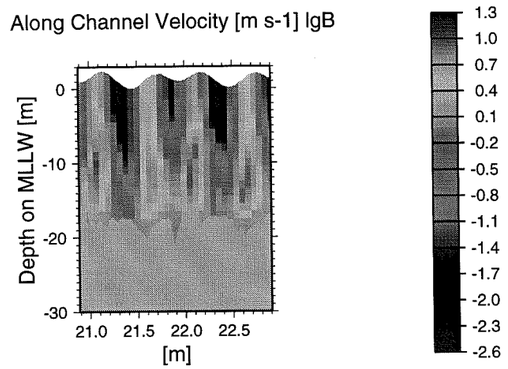


Figure B.5: Time series of along-channel velocity for G35a. See Figure (2.1).

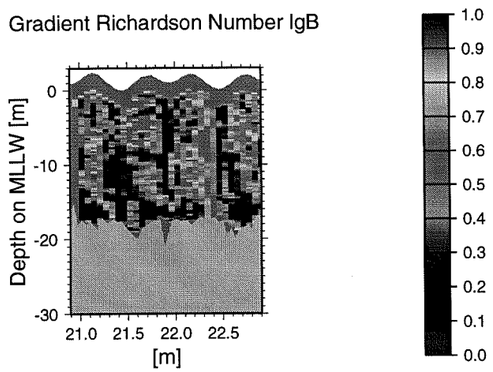


Figure B.6: Time series of gradient Richardson number for G35a. See Figure (2.1).

B.1.3 Buoy 35b station

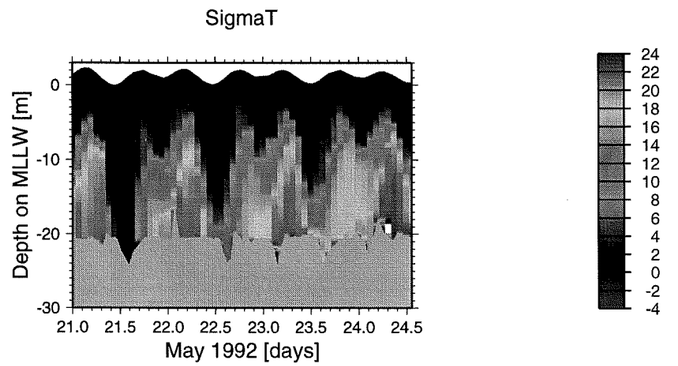


Figure B.7: Time series of density expressed as σ_T for G35b. See Figure (2.1).

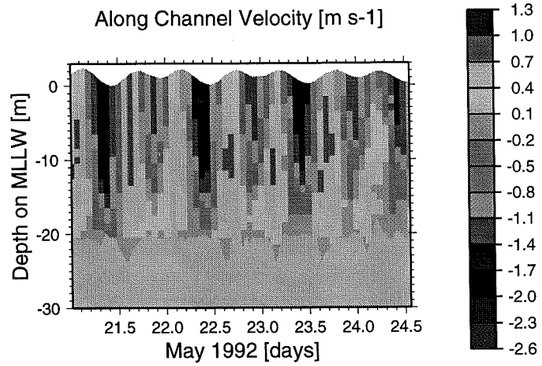


Figure B.8: Time series of along-channel velocity for G35b. See Figure (2.1).

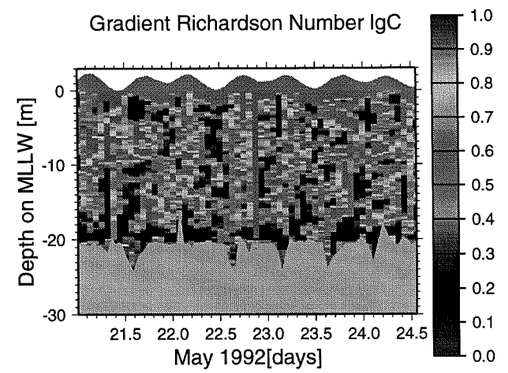


Figure B.9: Time series of gradient Richardson numbers for G35b. See Figure (2.1).

B.1.4 Buoy 37 station

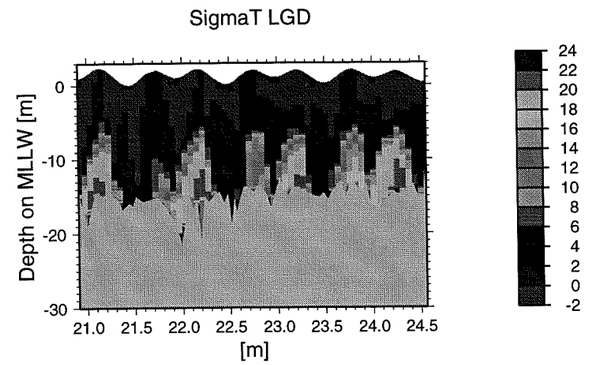


Figure B.10: Time series of density expressed as σ_T for G37. See Figure (2.1).

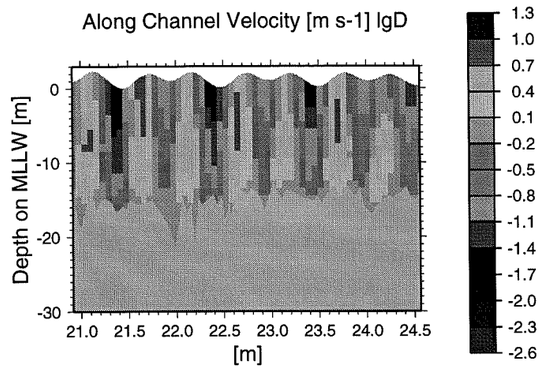


Figure B.11: Time series of along-channel velocity for G37. See Figure (2.1).

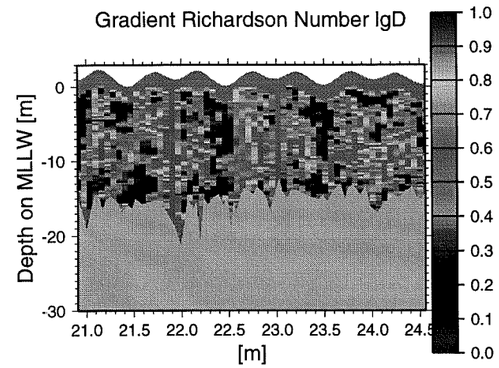


Figure B.12: Time series of gradient Richardson number for G37. See Figure (2.1).

B.1.5 Pier 11 station

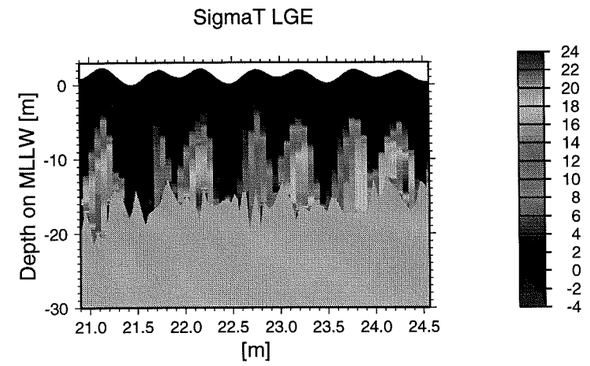


Figure B.13: Time series of density expressed as σ_T Pier 11

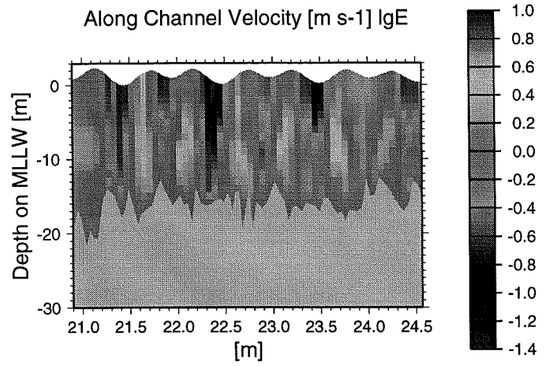


Figure B.14: Time series of along-channel velocity Pier 11

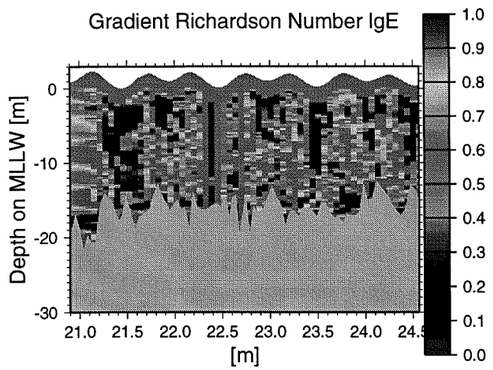


Figure B.15: Time series of gradient Richardson numbers Pier 11. See Figure (2.1).

B.1.6 Buoy 39 station

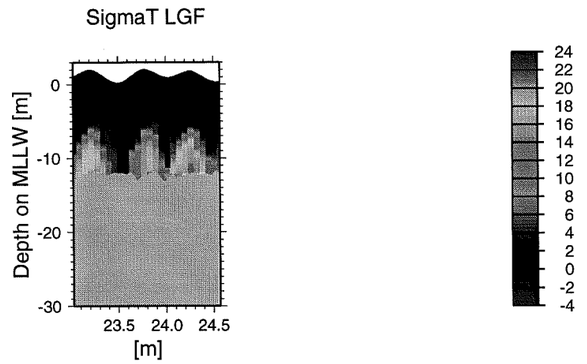


Figure B.16: Time series of density expressed as σ_T for G39

. See Figure (2.1).

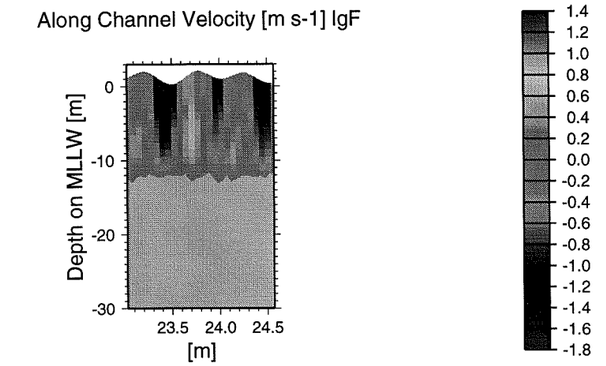


Figure B.17: Time series of along-channel velocity for G39. See Figure (2.1).

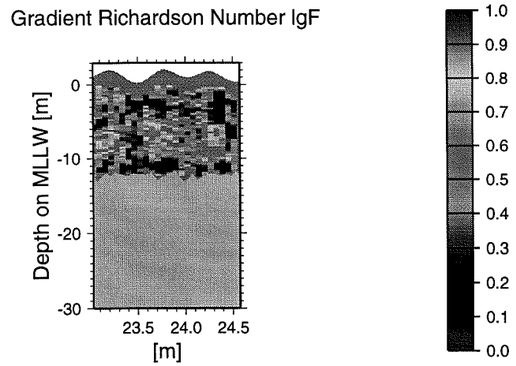


Figure B.18: Time series of gradient Richardson number for G39. See Figure (2.1).

B.1.7 East end mooring basin station

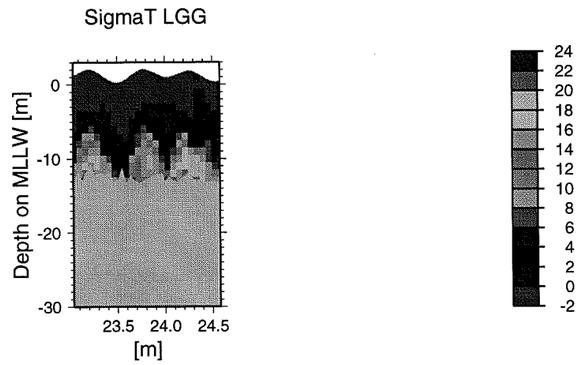


Figure B.19: Time series of density expressed as σ_T for East End. See Figure (2.1).

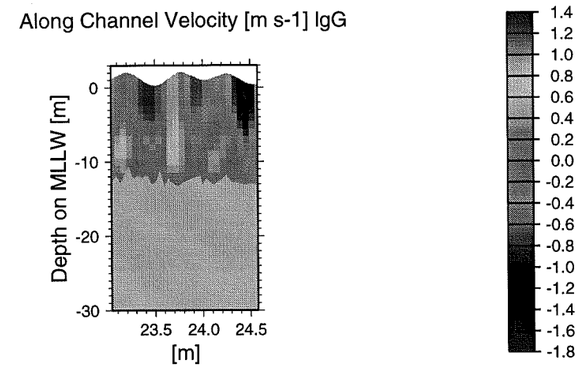


Figure B.20: Time series of along-channel velocity for East End. See Figure (2.1).

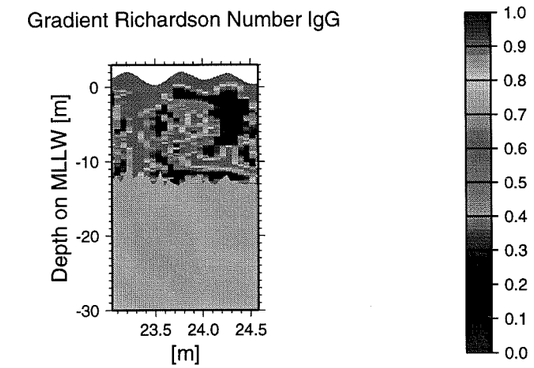


Figure B.21: Time series of gradient Richardson number for East End. See Figure (2.1).

B.2 Harmonic data

This section presents the harmonic velocity and density data collected in the south channel of the Columbia River estuary during the time period 19 - 25 May 1992 plotted as time along-channel contour plots for each constituent. The station locations are shown in Figure (2.1).

B.2.1 Velocity

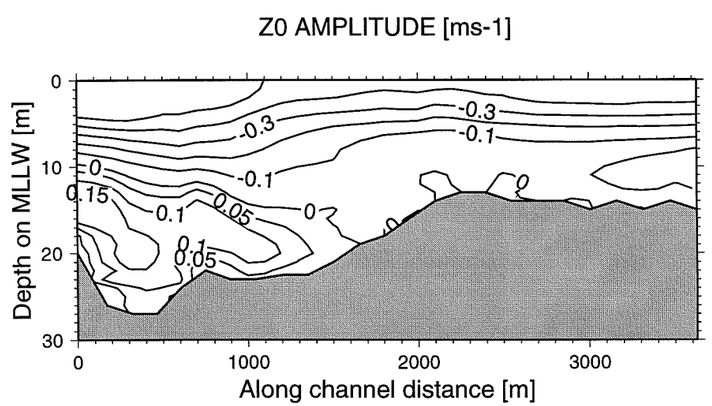


Figure B.22: Hamonically analyzed Z_0 along-channel velocity, along-channel section

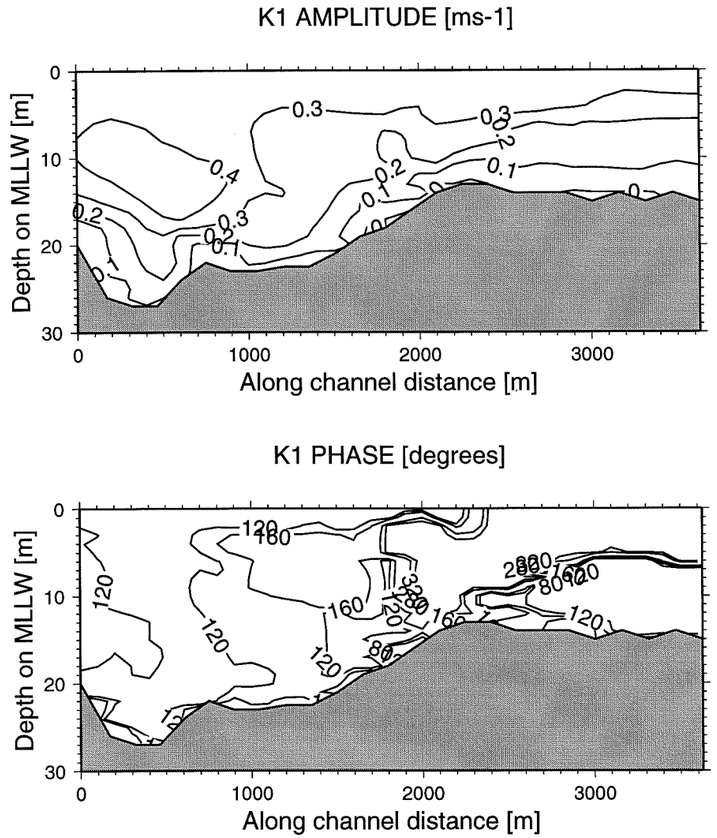


Figure B.23: Hamonically analyzed K_1 along-channel velocity, along-channel section

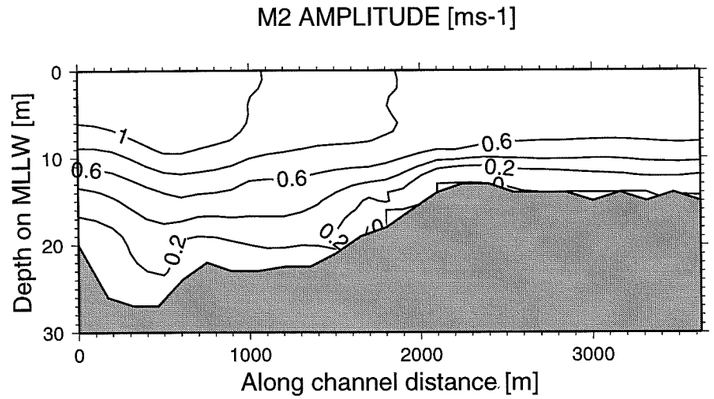


Figure B.24: Hamonically analyzed M_2 along-channel velocity, along-channel section

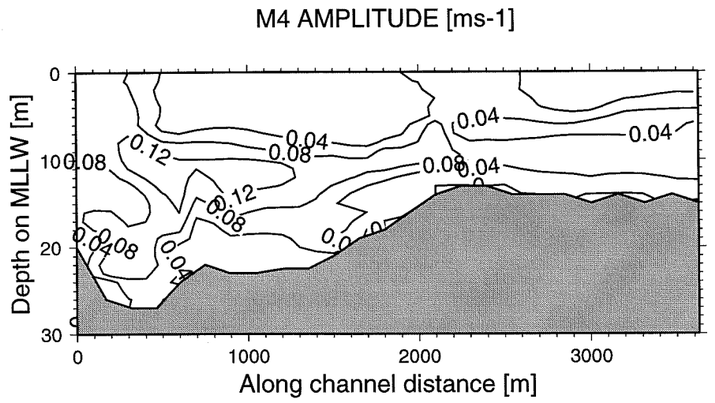


Figure B.25: Hamonically analyzed M_4 along-channel velocity, along-channel section

B.2.2 Density

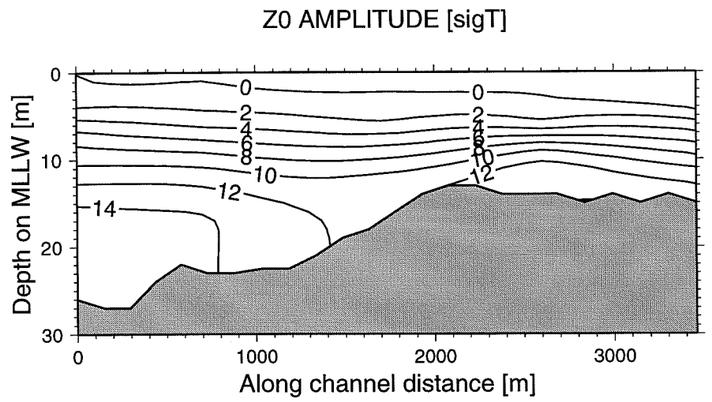


Figure B.26: Hamonically analyzed Z_0 density, along-channel section

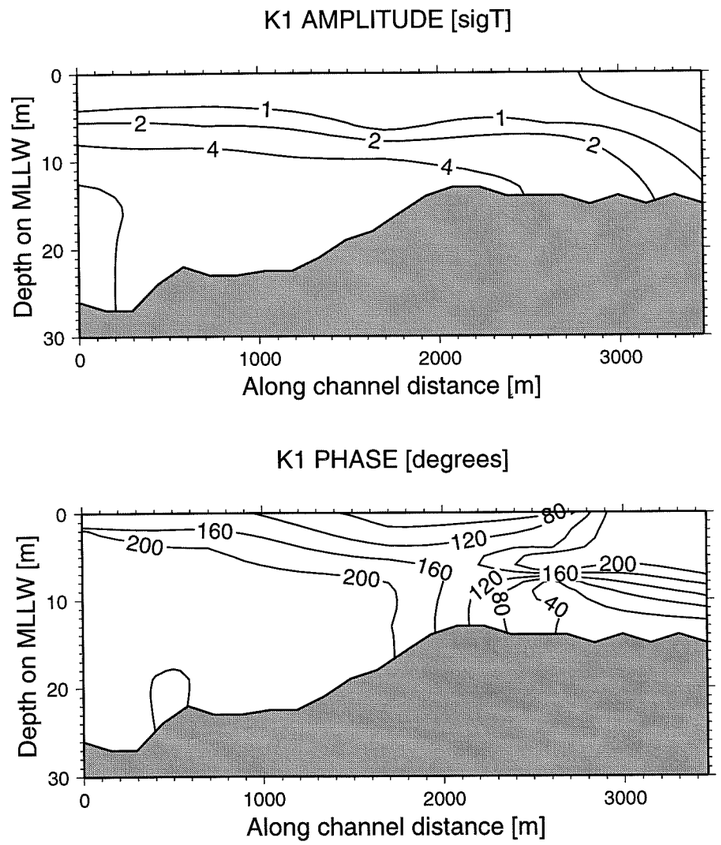


Figure B.27: Hamonically analyzed K_1 density, along-channel section

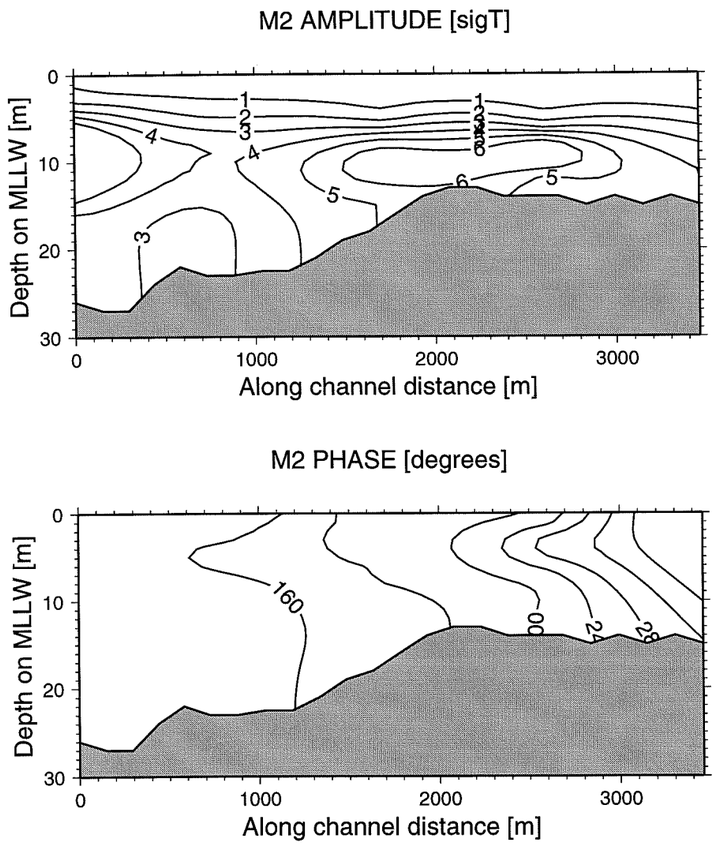


Figure B.28: Hamonically analyzed M_2 density, along-channel section

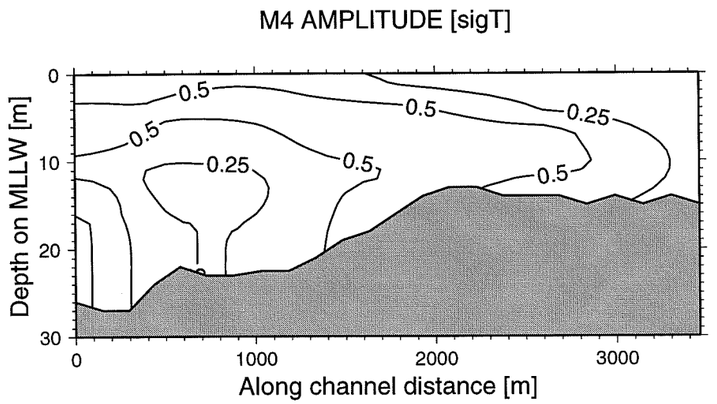


Figure B.29: Hamonically analyzed M_4 density, along-channel section

Appendix C

1-D BAROTROPIC MODEL

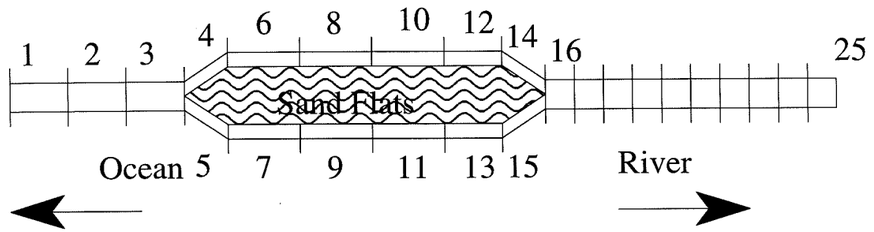


Figure C.1: Schematic of idealized channel topography for 1-D model. The channel bifurcates from section 3 into sections 4 and 5 and then rejoins at section 16. Refer to table C.1 for actual widths, depths and lengths used.

For 1-D barotropic tidal propagation model the variables are as follows: LL is the section length, BB channel width, BBt is the total width, HH is the depth of the channel and QrFRAC is the fraction of the total riverflow passing through that section.

Table C.1: Channel geometry used with Figure (C.1).

sec	LL [m]	BB [m]	BBt [m]	HH [m]	QrFRAC
1	4000	3200	3200	12.00	1
2	3360	3150	3539	14.00	1
3	4160	3100	3839	13.30	1
4	4000	1604	2482	13.30	0.4
5	4000	1404	1502	13.30	0.3
6	2960	1440	2780	14.50	0.4
7	2960	1080	1900	13.20	0.3
8	3200	1504	2992	10.00	0.4
9	3200	1208	1444	13.10	0.3
10	2570	1100	4480	7.00	0.4
11	2570	1500	2000	13.00	0.3
12	11720	1000	2500	7.50	0.4
13	11720	2040	2580	12.00	0.3
14	1200	1200	2100	7.00	0.4
15	1200	3050	3525	7.00	0.3
16	2500	4004	4327	7.00	1
17	5000	3300	3600	7.25	1
18	10000	2000	2225	8.80	1
19	10000	1500	1500	10.00	1
20	10000	1300	1375	10.50	1
21	10000	1100	1250	11.00	1
22	10000	1000	1075	11.50	1
23	10000	900	920	11.60	1
24	10000	800	800	11.70	1
25	32500	700	700	12.00	1

VITA

Educational Experience

- **Ph.D. Geophysics** June 1989 to December 1998. Graduate research assistant. Geophysics Program, University of Washington. Seattle, WA. Dissertation title: Three-Dimensional Circulation Dynamics of Along-Channel Flow in Stratified Estuaries.

- **M.S. Aerospace Engineering** May 1987 to June 1989, Graduate research assistant. Department of Aeronautics and Mechanical Engineering, Case Western Reserve University, Cleveland, OH. Thesis title: Experimentally Measured Ignition Delay Time Measurements and Proposed Kinetic Mechanism for the Hydrogen-Oxygen System.

- **B.S. Mechanical Engineering** August 1981 to May 1985, Department of Aeronautics and Mechanical Engineering, Case Western Reserve University, Cleveland, OH.

Work Experience

- **Process Engineer** June 1985 to March 1987, The Babcock & Wilcox Company. Barberton, Ohio. Involved in the overall design of waste-to-energy plants, industrial power plants and co-generation plants.

Presentations

- **Eastern Pacific Oceanic Conference** 1998, Mt. Hood, OR. Poster: Musiak, J. D. and David A. Jay. A Model for Strongly Forced Estuaries.

- **Physics of Estuaries and Coastal Seas** 1994, Woods Hole, MA. Talk: Musiak, J. D. and David A. Jay. Convergence and Divergence Over Topographic Obstacles in a Stratified Estuary.

- **The Oceanography Society** 1993, Seattle, WA. Poster: Musiak, J. D. and David A. Jay. A New Viewpoint on Baroclinic Estuarine Circulation: Internal Overtide Generation in Tidal Channel Flows.

- **Estuarine Research Federation** 1993, Hilton Head, SC. Talks: A) Musiak, J. D. and David A. Jay. Internal Tidal Asymmetry and Dispersion. B) Jay, D. A., J. D. Musiak and David J. Kay. Internal Tidal Asymmetry and Particle Trapping in Stratified Tidal Flows.

- **Estuarine Research Federation** 1992, San Francisco, CA. Talk: Musiak, J. D. and David A. Jay. Observed Estuarine Turbidity Maxima Transport Processes in the Columbia River Estuary.

- **The Combustion Institute** 1988, Indianapolis, IN. Talk: Musiak, J. D. and T.A. Brabbs, Ignition Delay Time Measurements and Kinetic Model for Hydrogen-Oxygen.

Publications

- Jay, D. A. and J. D. Musiak, Particle Trapping in Estuarine Tidal Flows, Journal of Geophysical Research, Vol. 99, Number C10, pp. 20445-20461, October 15, 1994.

- Jay, D. A. and J. D. Musiak, Internal Tidal Asymmetry in Channel Flows: Origins and Consequences, pp. 219-258, in Mixing Processes in Estuaries and Coastal Seas, an AGU Coastal and Estuarine Sciences Monograph, C. Pattiaratchi (editor), AGU, Washington, D.C., 1996

- Kay, D. J., D. A. Jay and J. D. Musiak, Salt Transport Calculations from Acoustic Doppler Current Profiler (ADCP) and Conductivity-Temperature-Depth (CTD) Data: A Methodological Study, pp. 195-212, in Buoyancy Effects on Coastal Dynamics, an AGU Coastal and Estuarine Sciences Monograph, D. Aubrey and C.T. Friedrichs (editors), AGU, Washington, D.C., 1996

- Musiak, J. D. and T. A. Brabbs, Ignition Delay Time Measurements and Proposed Kinetic Model for Hydrogen-Oxygen. NASA National Aero-Space Plane Program, Contractor Report 1030, NASA Langley Research Center, November 1988.

5 20WWi 440
TH
1/99 31364-144